

N 70 42166

CR 110790

TECHNICAL REPORT 703-9

AN INVESTIGATION OF TANDEM ROW
HIGH HEAD PUMP INDUCERS

FINAL REPORT

By

Robert J. Etter

May 1970

CASE FILE
COPY

HYDRONAUTICS, incorporated
research in hydrodynamics

Research, consulting, and advanced engineering in the fields of NAVAL
and INDUSTRIAL HYDRODYNAMICS. Offices and Laboratory in the
Washington, D. C. area: Pindell School Road, Howard County, Laurel, Md.

HYDRONAUTICS, Incorporated

TECHNICAL REPORT 703-9

AN INVESTIGATION OF TANDEM ROW
HIGH HEAD PUMP INDUCERS

FINAL REPORT

By

Robert J. Etter

May 1970

Prepared Under

National Aeronautics and Space Administration
George C. Marshall Space Flight Center
Huntsville, Alabama
Contract No. NAS 8-20625

FOREWARD

The following report summarizes the work completed during a three phase theoretical and experimental research program conducted at HYDRONAUTICS, Incorporated. Eight previous technical reports have been issued covering various aspects of the program. The program was conceived with primary emphasis on the evaluation of the performance of tandem row pump inducers for use in rather "conventional" liquid fueled rocket engine systems such as those used in the very successful Saturn V launch vehicle which has allowed man, in the person of the Apollo Astronauts, to land on and explore the moon. By "conventional" it is meant that the launch vehicle is intended for a single mission and is not recovered and used again. The total firing time required of the propulsion system for such a rocket is measured in minutes. Recent emphasis for future space exploration has been shifted toward the as yet undeveloped "space shuttle vehicle". The space shuttle has been characterized as the "DC-3" of the space age. It is intended as the key to an economical space transportation system for use with earth orbital space stations. With the shuttle, significant portions of the launch vehicle and the space craft itself would be completely recoverable. The space craft, which would be capable of making soft-landings on airport style runways is intended for a minimum of 30 flights and a desired 100 flights. The reusable requirement puts a new set of constraints on the fuel/oxidizer turbopump system. In particular, with regard to the inducer, the problem of cavitation damage to materials becomes a serious consideration. Some comments on this aspect of the problem are presented in the report.

The present report, being the final summary of a rather long and involved study, contains some material excerpted from previous reports on the project as necessary to produce a concise statement of the problem and approach taken in attempting solution. In addition much new material not previously reported is presented.

TABLE OF CONTENTS

	Page
1.0 INTRODUCTION.....	1
2.0 PHASE I STUDIES.....	8
2.1 Design Studies.....	8
2.2 Experimental Program.....	11
3.0 PHASE II STUDIES.....	17
3.1 Higher Term Cambered Supercavitating Cascades..	17
3.1.1 Influence of Foil Type and Camber Index on Performance.....	22
3.2 Partially Cavitating Cascades.....	23
3.3 Expansion of Second Stage Design Capabilities..	25
3.4 Inducer Designs.....	26
4.0 PHASE III STUDIES.....	26
4.1 First Stage Design.....	26
4.2 Second Stage Design.....	37
4.3 Five-Term Cambered First Stage Tests.....	42
4.3.1 Overall Performance.....	42
4.3.2 Quasi Two-Dimensional Performance at Mid-Span.....	50
4.3.3 Stability Analysis.....	52
4.3.4 Mechanism of Flow Instability.....	57
4.3.5 Pressure Fluctuations in the "Stable" Region.....	62
4.3.6 Cavitation Damage.....	65

	Page
5.0 SUMMARY.....	67
6.0 CONCLUSIONS.....	79
ACKNOWLEDGMENTS.....	83
APPENDIX A - SATURN V INDUCER OPERATING CHARACTERISTICS...	84
APPENDIX B - SHUTTLE VEHICLE INDUCER OPERATING CHARACTERISTICS.....	91
REFERENCES.....	99

LIST OF FIGURES

- Figure 1 - Influence of Flow Coefficient on Relationship Between Suction Specific Speed and Tip Cavitation Number for a 0.60 Hub/Diameter Ratio
- Figure 2 - Influence of Hub/Diameter Ratio and Flow Coefficient on Suction Specific Speed at $\sigma = 0.010$
- Figure 3 - Test Section of HYDRONAUTICS, Incorporated Pump Loop
- Figure 4 - Overall View of HYDRONAUTICS, Incorporated Pump Loop
- Figure 5 - Yaw Head Probe and Traverse Stand
- Figure 6 - Summary of Performance of Supercavitating First Stages for Phase I Inducers at Near Design Flow Coefficient, $\phi = 0.10$
- Figure 7 - Tandem Inducer Model with - 6" Overlap and 0° Offset. First Stage - 3 Blades at 63.5° Pitch, Second Stage - 6 Blades at 55.8° Pitch
- Figure 8 - Tandem Inducer Performance with - 6" Overlap, Stage 1 - Three Blades 63.5° Pitch; Stage 2 - 6 Blades, 55.8° Pitch
- Figure 9 - Tandem Inducer Model with - 1.5 Inch Overlap and 0° Offset. First Stage - 3 Blades at 63.5° Pitch, Second Stage - 6 Blades at 55.8° Pitch
- Figure 10 - Tandem Inducer Performance with - 1.5" Overlap Stage 1 - Three Blades, 63.5° Pitch; Stage 2 - Six Blades, 55.8° Pitch
- Figure 11 - Distribution of Total Head Rise Between Stage 1 and Stage 2 During Tandem Tests of Phase I
- Figure 12 - Definition Sketch for a Two Dimensional Supercavitating Cascade

- Figure 13 - Pressure Distribution on Four Types of Isolated Foil Profiles (After Ref. 27)
- Figure 14 - Comparison of Foil Shapes for Circular Arc and Constant Pressure Camber (After Yim (18)) Foils in Cascade with $\beta = 75^\circ$, $c/d = 0.410$, $\sigma/C_L = 0.082$
- Figure 15 - Influence of Stagger Angle on Lift Coefficient for 0.75 Solidity for Various Camber Types
- Figure 16 - Influence of Solidity on Lift Coefficient for 65° Stagger Angle and Various Camber Types
- Figure 17 - Five-Term Cambered, Two Bladed, First Stage Impeller Using Linear Chord Length Variation
- Figure 18 - Comparison of Leading and Trailing Edge Profiles Used in Saturn V Engine Inducers to 5-Term Cambered Model with Constant Chord Length
- Figure 19 - Phase I Model Showing Fatigue Failure at Outer Portion of Leading Edge
- Figure 20 - Schematic Radial Sections Near the Leading Edge: (a) for an Inducer with Radial Leading Edge and (b) for an Inducer with a Swept Leading Edge
- Figure 21 - Stage 1, Two-Bladed, Second Order Design Using Five-Term Cambered Sections and Constant Chord Length
- Figure 22 - Stage One of a Tandem Row Inducer Using Five-Term Cambered Supercavitating Sections
- Figure 23 - Structural Compatibility of Phase III First Stage Model Having Five-Term Camber with Prototype Inducers Operating in LH_2 and LOX . Assuming 50,000 psi Prototype Working Stress

- Figure 24 - Second Stage Two Dimensional Blade Profiles at Three Radii. (Four Blades, 0.70 Hub)
- Figure 25 - The Two-Bladed Five-Term Cambered First Stage in Tandem with a Four Bladed Subcavitating Second Stage Having a 0.7 Hub Ratio
- Figure 26 - Head Coefficient as a Function of Suction Specific Speed for a Two-Bladed, Five-Term Cambered First Stage Impeller
- Figure 27 - Typical Radial Variation of Axial Flow Velocity and Total Head
- Figure 28 - Photograph of Cavitating Operation with $\phi_o = 0.10$, $l/c = 2.40$, $\psi = 0.055$, and $N_{ss} = 20,500$
- Figure 29 - Photograph of Cavitating Operation at same Conditions as in Figure 28
- Figure 30 - Photograph of Cavitating Operation with $\phi_o = 0.10$, $l/c = 2.75$, $\psi = 0.036$, and $N_{ss} = 25,700$
- Figure 31 - Photograph of Cavitating Operation with $\phi_o = 0.09$, $l/c = 3.10$, $\psi = 0.030$, and $N_{ss} = 28,500$
- Figure 32 - Effect of NPSH on Head Coefficient for a Two-Bladed Five-Term Cambered First Stage Impeller
- Figure 33 - Head Coefficient as a Function of Flow Coefficient for a Two-Bladed Five-Term Cambered First Stage Impeller
- Figure 34 - Three-Bladed Five-Term Cambered First Stage Inducer
- Figure 35 - Head Coefficient as a Function of Suction Specific Speed for a Three-Bladed, Five-Term Cambered First Stage Impeller
- Figure 36 - Effect of NPSH on Head Coefficient for the Three-Bladed, Five-Term Cambered First Stage Impeller

- Figure 37 - Head Coefficient as a Function of Flow Coefficient for a Three-Bladed, Five-Term Cambered First Stage Impeller
- Figure 38 - Effect of NPSH and Head Coefficient on Hydraulic Efficiency for a Two-Bladed, Five-Term Cambered First Stage Impeller
- Figure 39 - Effect of NPSH and Head Coefficient on Hydraulic Efficiency for a Three-Bladed, Five-Term Cambered First Stage Impeller
- Figure 40 - Influence of ϕ_0 and N_{ss} on Typical Axial Outlet Velocity Profiles for the Two and Three Bladed, Five-Term Cambered First Stage Inducers
- Figure 41 - Typical Radial Variation of Inlet and Outlet Total Head for the Two-Bladed and Three-Bladed Five-Term Cambered First Stage Inducers at $\phi_0 = 0.090$
- Figure 42 - Mid-Span Lift Coefficient and Ratio of Lift Coefficient to Cavitation Number as a Function of Chord-line Angle of Attack for the Two-Bladed, Five-Term Cambered Model
- Figure 43 - Mid-Span Lift Coefficient and Ratio of Lift Coefficient to Cavitation Number as a Function of Chord Line Angle of Attack for the Three Bladed, Five Term Cambered Model
- Figure 44 - Comparison of Two-Dimensional Linearized Theory (Ref. 28) to Experimentally Measure Lift and Angle of Attack at Mid-Span for the Two-Bladed, Five-Term Cambered First Stage Model Considering Only Data at or Very Near Fully Supercavitating Operation
- Figure 45 - Comparison of Two-Dimensional Linearized Theory (Ref. 28) to Experimentally Measure C_L/σ at Mid-Span for the Two-Bladed, Five Term Cambered First Stage Considering Only Data at or Very Near Fully Supercavitating Operation

- Figure 46 - Comparison of Two-Dimensional Linearized Theory (Ref. 28) to Experimentally Measured Lift and Angle of Attack at Mid-Span for the Three-Bladed, Five-Term Cambered First Stage Considering Only Data at or Near Fully Supercavitating Operation
- Figure 47 - Comparison of Two-Dimensional Linearized Theory (Ref. 28) to Experimentally Measured C_L/σ at Mid-Span for the Three-Bladed, Five-Term Cambered First Stage Considering Only Data at or Near Fully Supercavitating Operation
- Figure 48 - Typical Plots for the Determination of the Partial Derivatives M and N Required in the Yeh (16) Stability Analysis from the Data for a First Stage Inducer
- Figure 49 - Values of Yeh (16) Stability Parameter Calculated from Experimental Data at Various Points in the Operating Regime of the Two-Bladed, Five-Term Cambered First Stage
- Figure 50 - Values of Yeh (16) Stability Parameter Calculated from Experimental Data at Various Points in the Operating Regime of the Three-Bladed Five-Term Cambered First Stage
- Figure 51 - Cavity Lengths at which Severe Instabilities Occurred for the Two-Bladed and Three-Bladed Five-Term Cambered Supercavitating First Stage Models
- Figure 52 - Measured and Speculated Variation of Blade Cavity Length as a Function of Flow Coefficient at Constant NPSH
- Figure 53 - Typical Pressure Fluctuations and Amplitudes in the 0-100 cps Range

- Figure 54 - Head Fluctuations as a Percentage of Total Head Generated for Various Cavity Lengths in the "Stable" Operating Regime
- Figure 55 - Cavitation Damage to the Back Trailing Edge of a Phase I Constant Pressure Cambered Model
- Figure 56 - Cavitation Damage to the Plexiglas Test Section of the Pump Loop During Tests of the Phase I Constant Pressure Cambered Models
- Figure 57 - Cavitation Damage to the Face of the Phase III Two-Bladed Five-Term Cambered First Stage

NOTATION

C_L	Lift coefficient
$C_{L_{\text{camber}}}$	Lift coefficient due to camber
$C_{L_{\alpha}}$	Lift coefficient due to angle of attack
C_s	Specific heat
C_{θ}	Non-dimensional tangential velocity = $\frac{V_{u^r t}}{r}$
CPC	Constant pressure camber
D	Diffusion factor
D_m	Model diameter
D_p	Prototype diameter
D_t	Tip diameter
H	Head
H_L	Head loss
H_{static}	Static head
H_{vapor}	Vapor head
K	Coefficient, speed of distortion/axial inlet velocity
K_o, K_1, K_2	Coefficients in streamline equation
L	Lift, heat required for vaporization
LH ₂	Liquid Hydrogen
LOX	Liquid Oxygen

M	Loss parameter = $\frac{1}{2}\Delta\omega_1/\beta_1$
M_{cascade}	Actual value of loss parameter for given cascade geometry and flow conditions
M_{limit} or M_L	Limiting value of loss parameter for stability
N	Turning parameter = $\Delta \tan \beta_1 / \Delta \tan \beta_2$
N_s	Specific speed = $n \sqrt{Q}/H^{3/4}$
N_{ss}	Suction specific speed = $N \sqrt{Q}/\text{NPSH}^{3/4}$
NACA	National Advisory Committee for Aeronautics
NPSH	Net positive suction head
Pitch	Angle between chord line of root section and axis of rotation
P_{s_l}	Local static pressure
P_v	Vapor pressure
P_{v_l}	Local vapor pressure
Q	Discharge, gpm
T	Temperature
U	Velocity
U_l	Local velocity
U_t	Tip speed
U_1	Approach velocity to cascade
U_2	Velocity far downstream of cascade
V	velocity
V_{f_o}	Axial velocity upstream of hub

V_f	Axial velocity
V_u	Swirl velocity
ΔV_u	Change in swirl velocity
V_{θ_1}	Inlet tangential velocity
b/a	Cascade parameter (Ref. 18, 26)
c	Chord length
c/d	Solidity of a Cascade
cps	Cycles per second
d	Foil spacing in cascade
g	Acceleration due to gravity
gpm	Gallons per minute
k	Thermal conductivity, ratio of model to prototype stress
k_2, k_3, k_5, k_c	Camber indices for two, three, and five term and circular arc cambers
l	Cavity length
l/c	Cavity length/chord ratio
m	Exponent
n	Rotational speed in RPM, number of blades, exponent
n_m	Rotational speed in model, RPM
n_p	Rotational speed in prototype, RPM
psi	Pounds per square inch
r	Radius
r_t	Tip radius
rpm	Revolutions per minute

$t_{.20}$	Foil thickness at the 20 percent chord
w_1	Inlet velocity relative to blade
w_2	Outlet velocity relative to blade
y	Blade coordinate
z	Axial coordinate
α_1	Angle of attack
α_2	Direction of flow far downstream of cascade
α_c	Chord line angle of attack
β_1	Inflow angle relative to axial direction (Stagger angle)
β_2	Outflow angle relative to axial direction
β_m	Mean flow angle relative to axial direction
Γ	Circulation
Γ_b	Circulation per blade
η	Efficiency, dimensionless radial coordinate
η_H	Hub/diameter ratio, hydraulic efficiency
λ	V_{θ_1}/u_t , ratio of inlet tangential velocity to tip speed
ξ	Dimensionless axial coordinate
ξ_t	Non-dimensional axial extent ratio
π	3.14159
ρ	Fluid mass density
ρ_L	Liquid density
ρ_m	Fluid mass density in model

ρ_p	Fluid mass density in prototype
ρ_v	Vapor density
σ	Cavitation number or stress
$\sigma_{B.M.}$	Bending stress in blade
σ_l	Local cavitation number
σ_t	Tip cavitation number
ϕ_o	Flow coefficient, V_{f_o}/U_t
ψ	Head coefficient = gH/U_t^2
$\psi_{1st.}$	First stage head coefficient
$\psi_{2nd.}$	Second stage head coefficient
ω	Rotational speed, radians/sec.
ω_1	Head loss coefficient = $2gH_L/U_o^2$
∞	Infinity

1.0 INTRODUCTION

The inlet operating conditions of a pump including inlet net positive suction head, rotative speed, and total discharge may be combined to form the parameter, suction specific speed defined by Equation [1],

$$N_{ss} = \frac{n\sqrt{Q}}{NPSH^{3/4}} \quad [1]$$

Although not dimensionless, this parameter, in common use throughout pumping literature, may be shown by dimensional considerations (1)* to indicate the combination of inlet operating conditions which will give similar flow and cavitation patterns in machines which are geometrically similar. For a given discharge, high suction specific speed pumps result when either rotational speed is increased or inlet NPSH is decreased. Both changes result in significant system weight reductions when the pumps under consideration are being used as fuel or oxidizer pumps in liquid-fueled rocket engine systems (2). Reductions in the propulsion system weight can be utilized for a larger payload which is normally only a small percentage of total vehicle weight. As an example, consider the Saturn V launch vehicle used for manned lunar missions in the NASA Apollo program.

* Numbers in parentheses refer to references listed after the text.

The total launch weight of the Saturn V is 6,262,500 pounds with an escape payload of only 100,000 pounds. In this case, a decrease of only 1/2 percent in launch vehicle weight could result in a 30 percent increase in payload.

The three stage Saturn V uses liquid fuels and oxidizers with LOX/hydrocarbon fuel in the first stage and LOX/LH₂ in the second and third stages. By far the largest physical components of such a system are the propellant tanks whose wall thickness is determined primarily by tank pressure (3). Lower propellant tank pressures and therefore, lower pump NPSH allow lower vehicle weight. With higher rotative speeds, the size and weight of the fuel pumps are also reduced and the possible need for speed reduction components between turbines and pumps eliminated.

These weight reductions through the use of lower pressures and higher speeds are not, however, achieved without accompanying technical problems. Requiring the fuel/oxidizer** pumps to operate at high values of suction specific speed results in cavitation of the pump impellers. In ordinary pump experience, an N_{ss} value of 8000 or more results in cavitation causing vibration, noise, impeller damage, and a decrease in discharge and efficiency. The problem of pumping at high N_{ss} has however, been largely alleviated through the use of pre-pumping stages called "inducers" which operate rather satisfactorily even with

** Sometimes referred to only as fuel pumps.

extensive cavitation. A typical inducer consists of a high solidity, axial flow impeller with a small number of blades. The blade form usually approximates a simple helix. Inducers are generally located immediately upstream of the main fuel pump and operate at the same rpm on the same shaft as the main pump rotor. The problems of low efficiency and cavitation damage to the impeller blades are not restrictive in the application of inducers to rocket fuel pumps since the inducer produces only a small percentage of the total head rise of the fuel pump and the operating lifetime of the unit is short enough that little damage can occur.

This is not true in the case of the reusable space "shuttle" vehicle recently proposed as the key to an economical space transportation system. The shuttle is intended to be reusable for a minimum of 30 and a desired 100 flights. In this case impeller and casing damage due to cavitation becomes important (see Forward to this report).

Even in the case of the "one-time" or non-reusable engine, however, the problem of flow instabilities is very significant as a limiting condition for acceptable inducer operation. Model tests and operating experience (4,5,6,7) have shown that under certain operating conditions the discharge and head rise across an inducer may fluctuate violently resulting in corresponding engine thrust fluctuations contributing to the so-called "Pogo" effect. The unsteady motions and accelerations caused by the thrust fluctuations provide an unacceptable environment for delicate equipment and astronaut crews. In addition, low frequency oscillations may occur at or near the structural natural frequency.

One method suggested for reducing or eliminating the instabilities and fluctuating output of the inducer is the use of a tandem row inducer whose first stage operates at the design suction specific speed but delivers only a fraction of the total inducer head rise, thus operating with greater stability. The second stage of the inducer consequently operates at a lower suction specific speed and should also deliver the remaining head rise with greater stability. This concept has been used by other investigators (8,9,10,11).

In the present study, the nominal prototype fuel pumps following the inducers may be axial or centrifugal and cryogenic fuels or oxidizers are being pumped. The properties of cavitating flows in cryogenic fluids are such that modelling the flows in water is a conservative procedure, that is, flows in cryogenic fluids are more likely to be stable than similar flows in water. One factor which contributes to the stability of cryogenic cavity flows is local cooling at the cavity boundary (3). This local cooling results in a liquid film at the vapor cavity with a lower vapor pressure than that of the bulk fluid. Reference 3 presents the following equation for this local vapor pressure drop:

$$\Delta P_v = K \left(\frac{\rho_v}{\rho_L} \cdot \frac{L}{C_s} \cdot \frac{dp}{dT} \right) \left(\frac{\rho_L C_L}{k} \right)^m U^n \quad [2]$$

where

K depends on the hydrodynamics of the flow,

$\frac{dp}{dT}$ is the slope of the vapor pressure temperature curve at the bulk liquid temperature of interest,

U = a characteristic velocity,
 ρ_v and ρ_L are the vapor and liquid densities,
 k = the thermal conductivity of the liquid,
 L = heat required for vaporization, and
 C_s = specific heat of the fluid.

The last two terms are heat transfer factors. The exponents m and n are dependent on the heat transfer process accompanying cavitation. Venturi experiments (3) have established the validity of this relationship. The vapor pressure drop for water at ordinary room temperatures is negligible, the drop for most cryogenic fluids however is significant. If water, however, were superheated to 450°F its local vapor pressure drop would be similar to that of liquid H_2 at -423°F . Lower vapor pressure at the cavity surface means that the local cavitation number of the flow defined as:

$$\sigma_l = \frac{P_{sl} - P_{vl}}{\frac{1}{2}\rho U_l^2} \quad [3]$$

is actually higher than one would calculate based on the bulk fluid vapor pressure. Higher cavitation numbers correspond to lower N_{ss} values and nominally more stable flows. Tests using helical inducers (3,9) have further verified the fact that flow breakdown in liquid H_2 is much delayed over that of water at similar inlet conditions. By the same reasoning, it should be understood that the development of fully "supercavitating" flow

such as is required by designs presented later in this report is also delayed to lower cavitation numbers (higher N_{ss} values) than indicated in the data for water tests.

The operating conditions chosen to govern the design and testing of the present tandem row inducer were as follows:

- ϕ_o flow coefficient = 0.10
- ψ total head coefficient = 0.25
- N_{ss} suction specific speed = 30,000.

An innovation of the present tandem row design is the use of a supercavitating (12) first stage. The supercavitating stage is one whose blade form is deliberately designed to produce large stable suction side vapor cavities springing from the blade leading edge and collapsing beyond the trailing edge. The second stage is designed as a high solidity high head axial flow rotor operating with minimum cavitation.

Cavitating cascade performance is presented in terms of the cavitation number while cavitating pump performance is presented using the common parameter of suction specific speed. The two are related in the following manner. Assuming an axial flow machine with no prerotation, the inlet cavitation number will vary in the radial direction. For purposes of comparison, the tip cavitation number will be used since it represents the lowest value of any radial location. The tip cavitation number is defined as:

$$\sigma_t = \frac{H_{\text{static}} - H_{\text{vapor}}}{w_1^2/2g} \quad [4]$$

where

$$w_1 = \sqrt{U_t^2 + V_f^2}, \quad U_t = \frac{2\pi n}{60} r_t$$

w_1 is the velocity of flow relative to the impeller blade.

Suction specific speed is not dimensionless and is defined by Equation [1],

where

$$\text{NPSH} = H_{\text{static}} + \frac{V_f^2}{2g} - H_{\text{vapor}} \quad [5]$$

Combining these two relationships and further using the definition of flow coefficient,

$$\phi_o = \frac{V_{f_o}}{U_t} \quad [6]$$

One may obtain the following relationship between σ_T and N_{SS} for an axial flow machine with a 60 percent hub.

$$N_{SS} = \sqrt{\phi_o} \left[\frac{67272}{.41 + \phi_o^2} / \sigma_t + \frac{\phi_o^2}{.41 + \phi_o^2} \right]^{\frac{3}{4}} \quad [7]$$

For other hub-diameter ratios, the constants in the above equation will change. Figure 1 shows the solution of Equation [7] for a variety of tip cavitation numbers and flow coefficients.

Two characteristics of this relationship should be noted. First, there exists an optimum flow coefficient for which a maximum value of N_{ss} can be obtained for each tip cavitation number. Secondly, for each flow coefficient there exists a theoretical maximum possible suction specific speed which occurs when the tip cavitation number (i.e. inlet static pressure) is zero. This maximum possible N_{ss} is strongly dependent on ϕ_o . Figure 2 shows the influence of flow coefficient in suction specific speed for various hub/diameter ratios assuming a constant tip cavitation number $\sigma_t = 0.010$. The purpose in introducing these relationships is to clarify the operating regime of the inducers presently being discussed and to define the relationship between N_{ss} and cavitation number, both of which are used extensively in the report.

2.0 PHASE I STUDIES

2.1 Design Studies

The decision to use a supercavitating first stage was based on studies early in the project which indicated that in order to develop significant head across the first stage at the ambient pressures (NPSH) required the cavity length must exceed 30 percent of the chord length. This was based largely on the theoretical results of References 13 and 14. From the experimental cascade results of Reference 15 it appeared that severe cavity oscillations would occur if the cavity length were greater

than 30 percent of the chord. As the pressure in the study of (15) was further reduced and the cavities become larger than the chord, the oscillations ceased. This was in agreement with observations on isolated hydrofoils. It seemed, therefore, for the first stage to produce significant head rise and operate stably it must operate in the supercavitating mode.

The design head rise produced by the first stage was determined by the maximum allowable value within the limits of certain stability requirements. A generalized theory for the prediction of instabilities caused by self-induced circumferential distortion or rotating stall (16) was used to determine this maximum stable head rise. The application of this theory required a knowledge of the performance of supercavitating cascades under various inflow conditions.

It was shown by Auslaender (17) that an isolated foil which has a constant pressure camber distribution should have nearly optimum performance for supercavitating propellers and pumps. It was therefore decided to design the first stage of the inducer pump to obtain all lift from constant pressure camber. The development of a two-dimensional cascade theory for sections with constant pressure camber and finite cavity length was thus essential.

The performance of supercavitating cascades with constant pressure cambered blades and finite cavity lengths was studied theoretically using potential theory for cavity flows and a suitable model for finite cavity length. The results have been published in previous reports (18,19).

Meanwhile, the NACA data for 65 series cascades (20) was analyzed to determine the inception of rotating stall for non-cavitating pumps and the data of Numachi (21) and (22) for cavitating cascades of fully wetted sections was examined to determine inception for representative cavitating conditions.

Sample calculations (23) using the NACA data were made for two cases; a single row inducer pump with a head rise coefficient ψ of 0.25 and the first row of a tandem row inducer pump producing one half the total required head rise or a value of ψ of 0.125. In both cases the flow coefficient was 0.10. It should be noted that the NACA data extends only to inflow angles of 60° and 70° , while the inflow angle, β_1 , required was approximately 84 degrees. The measured results were therefore extrapolated. The results of this data analysis and sample calculations indicated that the loss parameter (16) required to give flow instability would be very large for these cascades and that rotating stall-type flow instability could not occur when cavitation was not present. In fact, the operating conditions were so far from inception of rotating stall as to yield little or no information about the design of cavitating helical inducer pumps (23).

The procedure used in the design of the supercavitating first stage was the familiar free-vortex, blade element theory described in References 51 and 52. This design method allows the design to be based on the performance of two-dimensional supercavitating cascades. The design equations are presented in Reference 34.

The design method for the second stage of the tandem row inducer was based on the theory for axial flow pump design presented in Reference 24. This method accounts for induced interference effects at an impeller blade as influenced by the other blades and the total downstream vorticity along the pump centerline. Optimization of the cavitation performance of the second stage is also accounted for in the procedure.

A design for a two stage inducer utilizing constant pressure cambered supercavitating sections in the first stage and meeting the design requirements while maintaining stable flow required that 15 percent of the total head be generated by stage 1 and 85 percent by stage 2.

2.2 Experimental Program

To conduct the experimental investigation, HYDRONAUTICS, Incorporated designed and fabricated a pump test loop capable of testing the performance of a variety of pumps over a wide range of operating conditions. The plexiglas test section of the loop is 22 inches long with an internal diameter of 7 inches. Plexiglas was used to make observations of the onset and extent of cavitation possible. Figure 3 shows the test section with the first stage of a tandem row inducer operating in it. The cloudy region is caused by cavitation.

The entire pump loop can be pressurized to eliminate cavitation or the pressure can be reduced to low absolute values to simulate low cavitation numbers. Thus, pumps can be tested at suction specific speeds as high as 30,000. A continuously

variable speed 150 hp drive provides a shaft speed up to 5000 rpm. A torque and thrust dynamometer located on the shaft downstream of the test section enables these quantities to be measured. A specially designed valve downstream of the test section allows flow regulation. A heat exchanger allows the water temperature to be kept steady even though considerable heat may be generated by the dissipation of energy in the water. Figure 4 shows an overall photograph of the pump loop and associated instrumentation.

The loop is equipped with instrumentation to measure static and total pressures and velocities in the test section. Probes of the type shown in Figure 5 are inserted through the test section wall for radial surveys of pressures, velocities and flow angularity. The probes can be located at several points in the test section. Arrangements are provided to effectively bleed air bubbles from the tubing. This can be a major source of error especially at low absolute pressures.

Pressures are measured using pressure transducers of the differential reluctance type and the output is displayed digitally. The shaft rpm is measured by means of a calibrated strobe light, which is also essential for observation of the type and extent of cavitation occurring on the blades.

The test procedure adopted for all impellers was the same as that used for cavitation tests on a conventional pump. The flow coefficient is held constant and the net positive suction head (NPSH) of the pump lowered until the total head decreased rapidly due to cavitation. All tests were conducted at a shaft

speed of 4000 rpm. The pressure upstream of the impeller is first reduced to the required value. The valve downstream of the pump is then regulated until the required flow coefficient is obtained. Measurements of the static and total pressures and flow angularity are made at 5 or 6 radial positions upstream and downstream of the impeller. These data are processed by an IBM 1130 computer which integrates the pressures and velocities and calculates the appropriate performance parameters and coefficients.

The Phase I test program conducted in the HYDRONAUTICS, Incorporated pump loop (34) indicated that for optimum performance, both stages required empirical modification to solidity and pitch angle. Tests conducted on each stage separately indicated that the best performance among the models tested was obtained from a first stage with 3 blades ($c/d = 0.810$) at the original design pitch* and a second stage with 6 blades ($c/d = 2.41$) with a blade pitch ten degrees less than the original design pitch. Section geometry was unchanged during these tests.

Figure 6 summarizes the performance of various Phase I stage 1 models having numerous combinations of pitch and number of blades.

The best first and second stages were then tested in tandem with a -1.5 and -6 inch overlap. Figures 7 and 8 show the tandem model with -6 inch overlap and the resultant experimental performance. Figures 9 and 10 are similar but for the -1.5 inch overlap.

* Pitch is defined as the angle between the chord of the root section and the axis of rotation.

In order to compare the performance of the final Phase I tandem inducer selected to the original design requirements, the operating point where the distribution of head generation between the first and second stages matched the original design point distribution was chosen. This point is where 15 percent of the total head is generated by the first or supercavitating stage and 85 percent by the second or subcavitating stage. From Figure 11 this occurs at about $N_{ss} = 22,000$ for the six inch overlap and $N_{ss} = 22,500$ for the 1.5 inch overlap.

Using $N_{ss} = 22,000$ for Stage 1 and $\phi \approx .080$, from Figure 8 the head coefficient generated is approximately $\psi = 0.29$ and the first stage cavity length $l/c = 1.75$. Overall efficiency at this point is 62 percent. This operating point is shown as a solid triangular symbol in Figure 8. Similarly for a 1.5 inch overlap, the same operating point is shown in Figure 10. In this case the first stage cavity length is about $l/c = 1.50$ and the overall efficiency 66 percent.

Table 1 summarizes the optimum experimental inducer performance and compares these results to the original design parameters. The tandem model produced more than the design head coefficient (0.29/0.25) at slightly less than the design flow coefficient (.083/.100) and less than the design suction specific speed (22,000/30,000). First stage cavity lengths were approximately as required by the original design (1.50 - 1.75/1.50).

TABLE 1
Summary of Phase I Tandem Inducer Performance*

Operating Parameter	Original Design Value	Experimental Value at -1.5 inch overlap	Experimental Value at -6 inch overlap
N_{ss} , entrance	30,000	22,000	22,000 to 23,000
ϕ_o , average	0.100	0.083	0.083
ψ , total	0.250	0.283	0.296
ψ_{2nd}/ψ_{1st}	0.85	0.85	0.85
η_T , total	65% (1st stage only)	66%	62%
Stage 1 Pitch	63.5°	63.5°	63.5°
Stage 1, No. of blades	2	3	3
Stage 1, Char. solidity	0.540	0.810	0.810
Stage 1, l/c	1.50	1.50	1.75
Stage 2, N_{ss}	13,250	10,600	10,600
Stage 2, pitch	65.8°	55.8°	55.8°
Stage 2, No. of blades	6	6	6
Stage 2, Char. solidity	2.43	2.43	2.43

* Constant pressure cambered first stage.

The experimental performance, while not quite reaching the design objectives did indicate that the tandem inducer using a supercavitating first stage has definite potential as a high suction specific speed design concept. Low frequency instabilities or oscillations were noted at breakdown but appeared to stem from unstable cavity lengths rather than from Yeh (16) type instabilities which the design was intended to avoid. Little difference was observed between the performance at -6 inch overlap and -1.5 inch overlap and the "trade-off" of head generation between the first and second stages as indicated in Figure 11 produced a relatively flat ψ vs N_{SS} characteristic (Figures 8 and 10) well suited to rocket fuel pump applications where N_{SS} may vary during the course of a flight.

Further manipulation of the pitch of the tandem inducer stages (in particular smaller pitch angles for Stage 1) may have reduced the head coefficient and increased the flow coefficient bringing each closer to the design values. This would probably have resulted in higher breakdown N_{SS} values because of the smaller angles of attack. It was concluded, however, that with the constant pressure cambered blade shapes, it was doubtful that the design goal of 30,000 could be reached.

One characteristic of constant pressure cambered cascades is that as the solidity is increased, the camber of the foil decreases approaching a flat plate. This is detrimental to the stability of the flow since flat plate profiles create a higher drag for the same lift than cambered profiles. The flat plate must rely entirely on angle of attack for lift generation.

The Phase I experiments also indicated that the original second stage design apparently induced more swirl than predicted by the theory (24). In order to improve the prediction of induced by a radial line vortex in an annulus (25) needed to be calculated for smaller axial and circumferential spacings and for larger hub to diameter ratios.

3.0 PHASE II STUDIES

3.1 Higher Term Cambered Supercavitating Cascades

Phase II (26) of the project was aimed partially at further improving the capability for tandem inducer design through a theoretical study of higher term cambered supercavitating cascades. It was speculated that higher-term cambered first stages, should improve the suction performance of the tandem inducer considerably.

The supercavitating cascade flow is schematically illustrated in Figure 12. The cascade consists of an infinite array of identically cambered blades having a stagger angle β_1 and an angle of attack α_1 . The mean chord length of each blade is c and the spacing of the blades in the direction of the stagger angle is d . The flow is turned by the cascade from its original horizontal direction and velocity U_1 at upstream infinity to the direction α_2 and velocity U_2 at a location far downstream.

The types of foils under consideration are those which are outlined by Johnson (27). The shapes which he derived are those resulted from the optimization of a finite number of

terms of the vorticity distribution in the airfoil plane such that maximum lift-drag ratio resulted for each hydrofoil shape. Strictly speaking, the foils thus generated can only be called two, three, or five term cambered foils in the isolated case, since the effects of cascade may modify the optimum shapes slightly. For continuity with the isolated foil case and for ease of calculation, the physical shapes presented by Johnson (27) have been used in the present program. This is further justifiable from a physical standpoint since it permits the computation of the performance of the same physical shape under a variety of conditions. This is in contrast to the constant pressure camber case where each change of cascade geometry of flow conditions results in a different foil shape. For the constant pressure camber case, therefore, off-design performance cannot be directly calculated.

Reference 28 reports the results of the theoretical study of the flow past a cascade of supercavitating cambered blades utilizing potential flow theory. The difficulty in this case can be appreciated by considering the much simpler problem of incompressible flow past a single supercavitating hydrofoil. The only exact analytical method known, based on certain artificial models of cavity termination, is the hodograph technique, which is rather complex. To solve such complex problems, one usually introduces suitable approximations. The most convenient of them is the linearized, closed-cavity theory of Tulin (29). Realizing the complication, involved a similar approximation was made in the analysis of Reference 28. The

theoretical approach utilized some of the concepts developed in (30). The method is inherently limited in its applications because it is based on the assumption of small thickness of the blades being treated and relatively small disturbances being generated. However, in practice, the inducer blades are thin and consequently the linearized results may be used for design purposes.

Based on the theory developed, a computer program (actually an interdependent set of programs) to compute cascade characteristics was written, compiled and first verified by comparison with isolated foils and with cascades of flat plate foils in the existing literature (31, 32).

In addition to the first order linearized results, the program also calculates second order approximations using equations presented by Hsu (33) and verified for the isolated circular arc case. While there is no available method for verifying the second order approximation for cascades or for cambers other than the circular arc, it was included since little additional programming was required to do so and the results were expected to be more conservative than the first order results.

For the circular arc, the convention of Johnson (27) is used where the chord of the foil is rotated through $1/8$ of the central angle to insure a positive pressure over the entire wetted face of the foil. The camber indices k_2 , k_3 , k_5 , k_c are the respective lift coefficients of the isolated, infinite depth,

zero sigma, zero angle of attack foils having two term, three term, five-term and circular arc camber distributions. The higher the camber index the greater the camber of the respective foils and the higher the number of "terms" in the camber distribution, the further aft the center of pressure is shifted. Figure 13 after Reference 27 shows the pressure distributions on four types of isolated higher-term cambered foil profiles.

Reference 26 details the problems encountered in extending the calculations to high stagger angles and solidities as required for inducer applications. In particular, a narrow range of cavity lengths and cavitation numbers are attainable for which the results are physically meaningful. It is not certain whether or not the problems discussed in detail in (26) are an inherent difficulty of the method or a result of the numerical calculations used to calculate the cascade characteristics. As explained in (26), however, the small b/a or long (finite) cavity range of calculation was used to determine cascade characteristics.

The computations of (18) are different from the present case in two ways. First, the foil shape used in (18) was a constant pressure cambered geometry. This is different from any shape used in the present case but may be approximated by the circular arc. Secondly, the results of (18) do not yield a particular cavitation number, lift coefficient and foil shape for each cascade geometry but rather the ratio of cavitation

number and foil shape to lift coefficient. Thus σ/C_L and y/cC_L are the primary parameters for a given stagger, solidity and cavity length. Angle of attack α is given as α/C_L and is not an independent variable.

It was, therefore, rather difficult to directly compare the constant pressure cambered results to the results of Reference 28. A comparison was made however, at $\beta = 75^\circ$ and $c/d = .410$. In the long cavity region where both results were well behaved, the circular arc case at $k = .135$ (central foil angle = 12°) and geometric angle of attack of 7.4° produced the same ratio of σ/C_L as the constant pressure cambered case. The CPC foil required only 5.05° geometric angle of attack for the same σ/C_L ratio and in addition required 27 percent less camber. In other words, the CPC case appears to have a more effective or efficient camber distribution in cascade.

A comparison of the actual physical shapes of the two foils being considered is shown in Figure 14. The vertical scale is distorted. The camber distributions are different but not different enough that one would expect the large difference in camber and angle of attack indicated for similar lift-cavitation number performance. Since the cascade characteristics were calculated by different methods, the technique of calculation and method of linearization may have introduced part of the difference. However, based on the Phase I experimental program (34), we know that the value of the parameter $C_L/\sigma c/d$ for Stage 1 of Inducer 1 was less than 1/3 of the predicted theoretical value. Even acknowledging real fluid and three dimensional effects have contributed to this reduction, the results

indicate that the CPC theory (18) tends to overestimate the ratio C_L/σ . We may also conclude that the tendency of the calculation of (28) to indicate a more conservative relation between σ and C_L for similar geometries, (i.e., that more camber and angle of attack is required for a similar camber distribution to yield a particular lift coefficient at a particular cavitation number than in the calculation of (18)) is likely to be more correct based on the Phase I experiments.

Reference 26 compares the results of the theory of (28) to some experimental work reported in References 15 and 35. Neither reference has much usable data and little could be concluded from the comparisons. In both cases the experimental conditions were not well defined and in (35) the data was from an impeller in which three dimensional effects could not be accounted for. It was concluded in (26) that good, reliable supercavitating cascade data is virtually nonexistent.

3.1.1 Influence of Foil Type and Camber Index on Performance-

In order to compare the influence of foil type and camber index on typical cascade geometries, a series of calculations were undertaken in (26) with l/c values in the "long-cavity" range in which lift and cavitation number vary little with l/c .

Figure 15 illustrates the effect of stagger angle on the lift coefficient of a series of cascades with all five camber types and $c/d = 0.75$, $\alpha = 10^\circ$, and $k = 0.15$. (The flat plate case of course has $k = 0$). Over the entire range of stagger angles

calculated, the five term camber foils show higher lift coefficients than any of the other types, but as stagger angle increases, the five term camber performance degrades at a rate slightly higher than the others and its relative advantage decrease.

Figure 16 shows the influence of solidity on lift coefficient for cascades using all five camber types, $\beta = 65^\circ$, $\alpha = 10^\circ$ and $k = 0.15$. Each type degrades sharply with increasing solidity. Again the five term camber case is best over the entire range but it degrades more rapidly with increasing solidity than the other types.

Based on these results and additional results presented in (26), the five term cambered sections were chosen to be used in future first stage inducer applications.

3.2 Partially Cavitating Cascades

Reference 36 presents a theoretical study of cascades of partially cavitating cascades (i.e. the cavity length is less than the chord of each foil).

The formulation presented gives the linearized solution for the flow past a cascade of partially cavitating cambered blades. From the analysis, it is possible to determine the lift and drag coefficients, cavitation number, cavity shape and downstream flow conditions for any given specific cascade geometry, blade shape, cavity length and initial inflow conditions. The theory was not programmed under the present scope of work. The only

previously available theoretical study on flow past a cascade of partially cavitating blades (37) dealt with the problem of thin flat plate hydrofoils. Reference 36 formulates the problem with the aid of conformal transformation and assumes that the flow is two-dimensional.

As indicated by the experiments of Wade and Acosta (15) the flow is unstable when the cavity length-chord ratio is close to unity; the analysis is, therefore, invalid in this flow regime. The analysis is also limited to cases in which the disturbance, caused by the presence of the blades, is small - an inherent restriction in the linear approximation. However in practice, the blades are, generally, thin. Consequently the linearized results are valuable as a guide in the design of inducers and other turbomachinery.

The amount of experimental data available concerning the performance of partially cavitating cascades is also limited but in much greater supply than the fully cavitating cascades previously discussed. The data of Wade and Acosta (15) is largely in the partially cavitating range as is some of the work of Numachi (21,22) and United Aircraft (38). Furthermore, much of the work on helical inducers in the literature may be considered as three-dimensional data for partially cavitating flat plate cascades (4,39,40,41, etc). Since in most cases, however, only overall performance is considered, it is difficult to draw conclusions regarding two-dimensional cascades from this data.

3.3 Expansion of Second Stage Design Capabilities

Reference 42 presents a theoretical study of the three-dimensional flow field from a radial vortex filament in a cylindrical annulus. As previously explained in Section 2.1 this information is necessary to apply the technique of (24) to design the subcavitating second stage. The calculations of (25) were originally used but were only available for a 0.60 hub ratio. The results of (42) are summarized below:

(a) A computer program to solve the three-dimensional flow field from a radial vortex filament in a cylindrical annulus was written.

(b) The convergence of the solutions depended on proximity to the vortex filament, with more and more terms required in the summation as the filament is approached in either the axial or tangential direction.

(c) The eigenvalues used in Reference 25 agreed with the values of (42). The series representation of the eigenvalues (43) was valid for small values of m and n only.

(d) Considerable disagreement was found between the three-dimensional results of (42) and the results reported in Reference 25 except at the mid-radius.

(e) A systematic deviation was found between the three-dimensional calculations and the two-dimensional approximation with maximum differences on the order of 25 percent. The larger the hub/diameter ratio, the closer the three-dimensional results were to the two-dimensional.

(f) Eigenvalues and coefficients required for the three-dimensional calculations at hub/diameter ratios, η_H , of 0.60, 0.70 and 0.80 and actual velocities for $\eta_H = 0.70$ are tabulated in Reference 42.

(g) A sample interference streamline calculation showed little difference between $C_{\theta \text{ total}}$ using three-dimensional results or two-dimensional results in the summation in the case of $\eta_H = 0.70$. For this case, therefore, the more complicated three-dimensional calculations were unjustified.

3.4 Inducer Designs

At the conclusion of Phase II (26) new first and second stage inducer designs using the newly generated higher term camber information of (28) and the improved and expanded second stage design capability provided by (42). These designs will be discussed in the following section covering Phase III of the project and integrated with the Phase III design work.

4.0 PHASE III STUDIES

4.1 First Stage Design

In Reference 26 the design of a five-term cambered impeller using a specified linear chord length variation was presented. The chord lengths were chosen to roughly correspond to the chord length variation which resulted from the constant pressure cambered design of Reference 34. Table 2 shows the results of this design and Figure 17 shows three views of the impeller

TABLE 2

Summary of Stage 1 Two Bladed, Second Order Design
Using Five-Term Cambered Sections and Specified
Linear Chord Length Variation

Quantity	Tip Radius R = 3.50"	Mid-Radius R = 2.80"	Hub Radius R = 2.10"
Head Coefficient, ψ	0.0375	0.0375	0.0375
Cavitation Number, σ	0.0132	0.0203	0.0352
Peripheral Speed, u , fps	122.2	97.9	73.3
Relative Inlet Angle, β_1	81°07'	78°56'	75°22'
Relative Mean Angle, β_m	80°55'	78°36'	74°36'
Relative Outlet Angle, β_2	80°46'	78°17'	73°45'
Axial Flow Velocity, V_f , fps	19.12	19.12	19.12
ΔV_u , fps	4.58	5.72	7.65
$\frac{C_L c}{\sigma d}$	5.62	5.66	5.72
c (inches)	5.50	4.75	4.00
Nominal Ref. Line. Angle of Attack, α_1	7.10°	8.80°	11.65°
Geometric Chord Line Angle of Attack, α_c	5.63°	6.78°	8.80
Solidity, c/d	0.500	0.540	0.606
Camber Coefficient, k	0.152	0.206	0.291
Section Efficiency, η	0.604	0.613	0.627
Lift Coefficient	0.148	0.213	0.332

design with required 0.60 hub. As discussed in (26) however, a considerable degree of freedom exists in the selection of the higher term cambered impeller geometry. This was not true in the case of the constant pressure cambered impeller whose chord lengths were dictated by the design procedure.

At the beginning of Phase III, the first stage design was reviewed. Using the theoretical methods of (28), a broad range of 5 term-cambered supercavitating cascades were calculated using the high speed computer programs previously developed. In particular, calculations were completed for cascades with stagger angles of 45° , 55° , 65° , 70° , 75.36° , 78.92° and 81.16° . For 70° or less solidities of 0.25 to 1.50, camber coefficients of 0.0 to 0.30 and angles of attack of 0° to 20° were used. The stagger angles used above 70° represent the required β 's at hub, mid, and tip radii for an inducer with a flow coefficient of 0.10 and a hub/diameter ratio of 0.60. At 81.16° the c/d range was 0.25 to 1.00. At 79.92° the range was extended to 1.25 and at 75.36° to 1.50. Camber coefficients ranged from 0 to 0.30 and angles of attack from 0° to 20° . The small b/a (or long cavity length) range was used based on previous experience with diverging solutions as discussed in Reference 26.

Using the results of the cascade calculation, parametric studies of designs satisfying the design requirements for the inducer were conducted. The design requirements for Stage 1 were taken to be the same as the inducers designed and tested under Phase I and the stage 1 design of Phase II. These were as follows:

Tandem head coefficient	=	0.25
Flow coefficient	=	0.10
Suction specific speed	=	30,000
Hub/diameter ratio	=	0.60
Model tip diameter	=	7.0 inches

Initially, the head developed by Stage 1 was taken to be 15 percent of the total required headrise, since this was found to provide satisfactory stability as determined by the Yeh (16) criterion in the Phase I and Phase II calculations. The design equations presented in Appendix A of Reference 34 were used and the design rpm was taken as 4000 rpm based on operating experience with the pump loop facility.

First and second order section designs at each of three radii were conducted using the design technique presented in Reference 26 and six arbitrarily selected camber coefficients. From these designs it was possible to prepare curves for each radius giving lift coefficient, solidity, and angle of attack as functions of camber coefficient for constant lift parameter, $\frac{C_L}{\sigma} \frac{c}{d}$, and cavitation number σ . Using these curves, intermediate designs were selected for the following conditions:

- (a) Specified linear C_L variation with radius,
- (b) Constant chord length at each radius,
- (c) Constant solidity with radius (radial leading and trailing edges), and
- (d) Specified linear (non-radial) chord variation with radius.

For each of the above conditions, first and second order designs using two and three blades were calculated.

The constant chord length design was particularly appealing. Taking the second order, two bladed constant chord length version and lining up the trailing edges to form a radial trailing edge results in a swept leading edge.

An experimental study of helical inducers conducted by Acosta (4) located regions of various modes of cavitating flow. Included among these were no cavitation, blade tip cavitation, alternate blade cavitation, fully developed cavitation, breakdown, and oscillating cavitation. The boundaries of these regions were not sharply defined but were typical of all helical inducers studied in (4). The effect of various geometrical changes on minimizing the extent and severity of the oscillating mode was examined in detail. Increasing the tip clearance helped suppress the oscillations but at the expense of cavitating performance and overall efficiency. A variable lead helix (9° at leading edge to 6° at trailing edge) greatly reduced the extent of the oscillating mode while causing little change in overall or cavitating performance. (A variable lead helix is actually a simple form of cambered blade). Finally, the effect of changing the leading edge from a radial line to a spiral line was examined. This modification had the effect of depressing the occurrence of oscillating cavitation to lower cavitation numbers and improving the cavitating performance.

The non-radial or spiral leading edge concept has also appeared in a number of inducers for operational rocket engines including the J-2 oxidizer and J-2 fuel inducers and the F-1 oxidizer inducer for use in the Saturn V launch vehicle. The non-dimensional leading edge and trailing edge profiles of these inducers are shown in Figure 18. All three employ tapered hubs, thus the entrance hub radii are different from the exit hub radii. The five-term model profiles on the same figure which will be explained later have the same hub radii for entrance and exit (non-tapered or cylindrical hub).

Swept or spiral leading edges also have certain structural advantages over radial leading edge profiles. Figure 19 shows the fatigue failure of the outer portion of the leading edge of a Phase I model (constant pressure cambered). The failure, due to fluctuating loads on the thin leading edge of the blade, occurred very nearly along a line formed by the arc of a circle with the center at the tip leading edge corner of the blade and radius equal to 17 percent of the chord at the tip radius. Blade configurations using swept leading edges avoid the problem of radial sections with uniformly thin cross-sections and resulting high stresses. Instead, each radial section has a tapered shape with thin outer edges gradually increasing to thicker root sections. This is illustrated by Figure 20. The effect of the swept leading edge on the blade projected profile is to actually eliminate that portion of the blade which failed as shown in Figure 19.

The final design selected for testing was the second-order, two-bladed, constant chord length case using a radial trailing edge. This is the model whose leading and trailing edge profiles are shown in Figure 18.

Table 3 summarizes the parameters of this design at each of three radii and Figure 21 shows two views of the impeller. The design was found to be marginally stable using the Yeh stability criterion (16) at the midspan.

Overall Conditions:

Discharge, Q	= 1464 gpm - 3.26 cfs
Tandem total head, H_T	= 116 ft.
First stage total head, H	= 17.4 ft.
Tandem specific speed, N_{sT}	= 4,310
First stage specific speed, N_s	= 18,010
pump rpm	= 4,000
Net positive suction head, NPSH	= 8.81 ft.
Number of blades	= 2

The first stage inducer design described above was manufactured and tested in the HYDRONAUTICS pump loop facility. Figure 22 shows the impeller as built. The procedure and results of the tests are presented in Section 4.3.

TABLE 3

Summary of Stage 1 Two-Bladed, Second Order Design Using
Five-Term Cambered Sections and Constant Chord

Quantity	Tip Radius R = 3.5"	Mid Radius R = 2.8"	Hub Radius R = 2.1"
Head Coefficient, ψ	0.0375	0.0375	0.0375
Cavitation Number, σ	0.0132	0.0203	0.0352
Peripheral Speed, U	122.2 fps	97.9 fps	73.3 fps
Relative Inlet Angle, β_1	81°07'	78°56'	75°22'
Relative Mean Angle, β_m	80°55'	78°36'	74°36'
Relative Outlet Angle, β_2	80°46'	78°17'	73°45'
Axial Flow Velocity, V_f	19.12 fps	19.12 fps	19.12 fps
ΔV_u , fps	4.58 fps	5.72 fps	7.65 fps
$\frac{C_L}{\sigma} \frac{c}{d}$	5.62	5.66	5.72
c (inches)	4.55"	4.55"	4.55"
Nominal Reference Line Angle of Attack, α	7.2°	8.8°	11.7°
Geometric Chord Line Angle of Attack	5.6°	6.5°	8.6°
Solidity, c/d	0.415	0.519	0.691
Camber Coefficient, k	0.165	0.210	0.286
Section Efficiency, η	0.607	0.618	0.640
Lift Coefficient C_L	0.175	0.230	0.300

Basic structural considerations are presented in Reference 34. The overriding requirement for supercavitating sections is always that the upper surface of the foil lie within the cavity generated by the wetted portion of the blade. When this condition is satisfied, the upper surface does not contribute to the hydrodynamics of the flow and is entirely determined from structural considerations.

The relationship between the model and prototype stress is (34):

$$\frac{\text{Model Stress}}{\text{Prototype Stress}} = \frac{\rho_m}{\rho_p} \left(\frac{n_m}{n_p} \right)^2 \left(\frac{D_m}{D_p} \right)^2 = k \quad [8]$$

As discussed in Reference 34 a survey of typical rocket inducers established a preliminary range of k values of 0.2-0.4 for the models presently under consideration.

If the titanium alloy Ti-Al 6-V4 is assumed for the prototype, the 10^7 cycle fatigue limit with a load factor of 0.40 at room temperature in a non-corrosive environment is about 100,000 psi (44). A factor of safety of 2 will provide a prototype design stress of 50,000 psi. It should be noted that the selection of the load factor and factor of safety in this case was arbitrary. In addition the ultimate strength and yield stress of Ti-Al6-V4 increases by nearly 100 percent as the temperature is reduced from 78°F to -420°F (44). This behavior is typical for most metals and alloys (45). Thus the use of room temperature values appears extremely conservative for cryogenic applications. Fatigue data in LH₂ or LOX, however,

is not available and stress-corrosion considerations may severely reduce the allowable design stress. A brief discussion of the effect of cavitation damage on blade life is presented in Section 4.3.6, however, further discussion of the material problems in the prototype inducer is beyond the scope and intent of the present study.

The critical stress in supercavitating foil sections as are presently being considered is nearly always in the leading edge chordwise bending mode.

Experience with supercavitating propellers has indicated that calculation of the chordwise bending stress at a location 20 percent from the leading edge provides a good criterion for maximum stress in this mode. This simplified calculation which considers the blade to be composed of an infinite number of parallel and independent cantilever beams has also been checked using a complex stress calculation based on a shell structure of varying thickness and non-uniform loading. Agreement between the complex and simplified methods has been within 5-10 percent. This is very close agreement considering the assumptions of the simplified approach. The same approach was therefore used for the stress calculation in a supercavitating inducer blade.

The following equation derived in Reference 26 may be used to give the stress in chordwise bending at the 20 percent chord when the blade pressure distribution over this portion is governed only by the contribution due to angle of attack. Figure 13 shows this to be generally true for the five term cambered case,

$$\sigma_{\text{B.M.}} = \frac{0.30}{144} \left(\frac{c}{t_{.20}} \right)^2 C_{L_\alpha} \rho w_1^2 \text{ psi} \quad [9]$$

where

$t_{.20}$ = the thickness at the 20 percent chord,

C_{L_α} = the lift coefficient due to angle of attack only,

ρ = the fluid density, and

w_1 = the absolute fluid velocity relative to the blade.

At the design operating point, the five term cambered model having a helical back surface has a chordwise bending stress of 6630 psi at the tip radius. Using a prototype working stress of 50,000 psi, the ratio of model to prototype stress in Equation [8] is 0.1326. From Equation [9] and using 70.8 lb/cu ft for LOX and 4.39 lb/cu ft for LH₂ we find that prototypes having tip speeds of 315 fps and 1263 fps are structurally compatible with the model in LOX and LH₂ respectively. Figure 23 presents as solid lines those combinations of prototype rpm and prototype diameters which satisfy this requirement. Circular points are included indicating the existing J-2 fuel and oxidizer inducers and the F-1 oxidizer inducer. The other points for conjectured shuttle vehicle inducers are discussed in Appendix B.

4.2 Second Stage Design

As discussed in Reference 34 the design procedure presented by Bowerman (24) allows the design of axial flow pumps without the use of experimental or theoretical cascade data. This procedure was attractive for the second stage design since no data exists for the high solidity, high stagger angle cascades required. The original design procedure as presented in (24) made use of the results of (25) in which the distribution of the three-dimensional tangential, axial and radial velocity components due to a single radial line vortex in an annular space are given.

The design method consists of representing each impeller blade by a number of radial line vortices. One blade is removed from the impeller and the interference streamline due to all the other blades and the total downstream vorticity is calculated. The camber and thickness distributions are then superimposed on the interference streamline, resulting in the final impeller design.

Reference 42 discusses results in which the calculations of (25) were repeated and extended to cover larger hub diameter ratios than the 0.60 originally calculated. Larger hub diameter ratios were required principally to lower the value of the diffusion factor (46) below the critical value of 0.60 at all radii. During the tests of the second stage inducer of Phase I (34) neither the total head nor the axial velocity remained constant along the radius as assumed in the design. A contributing factor causing this difficulty was flow separation along the hub section

and resulting flow "pile up" at the tip sections. The diffusion factor (46) has been shown to correlate well with limiting blade loading or separation in axial flow compressor blades.

$$D = \left(1 - \frac{w_2}{w_1} \right) + \frac{\Delta V_u}{2(c/d)w_1} \quad [10]$$

Correlation with NACA compressor data shows that to avoid separation this factor should be less than 0.60. The Phase I second stage design called for diffusion factors at the tip radius, mid radius, and hub radius of 0.259, 0.362, and 0.701, respectively. The diffusion factor at the hub was too large because of the high head coefficient and low peripheral speed. It could have been reduced by increasing the hub diameter ratio, but the necessary annular velocity distributions for the Bowerman method were only available for a 0.60 hub at the time.

For the new second stage design, a hub ratio of 0.70 was chosen. The design technique was that of (24) with slight modifications. Specifically, the technique of (24) results in a prescribed variation of chord with radius as a result of the optimization of cavitation performance. In the present case, the variation of chord with radius was arbitrarily prescribed. This is a minor consideration for the high solidity blades and large hub ratio of the present design for which the cavitation optimization of (24) has little effect. The chord variations considered included:

- (a) Constant solidity, c/d ,
- (b) Constant axial extent, ξ_t ,
- (c) Constant chord, c ,
- (d) 180° wrap at hub and 45° leading edge sweep, and
- (e) 180° wrap at hub and 60° leading edge sweep.

Case (e) was chosen and the parameters of this design are tabulated in Table 4. The overall design utilized the following:

Number of blades - 4

Vortices per blade in Bowerman technique - 6

Camber type - NACA "65"

Thickness distribution - NACA 16-009 function

Thickness - tip 1.5 percent, mid 2.5 percent,
hub 4.5 percent

Hub ratio - 0.70

The tangential component of velocity V_u due to all blades except the one removed is non-dimensionalized as follows:

$$C_\theta = \frac{V_u r_t}{\Gamma} \quad [11]$$

The value of C_θ in (24) and (34) was found to vary almost linearly with non-dimensional axial distance $\xi = z/r_t$. Thus,

$$C_\theta \approx K_0 + K_1 \frac{\xi}{\xi_t} \quad [12]$$

TABLE 4
 Summary of 2nd Stage, 4-Bladed Design
 with 0.70 Hub/Diameter Ratio

Quantity	Tip Radius (3.5")	Mid Radius (2.975")	Hub Radius (2.45")
Head Coefficient, ψ	0.2125	0.2125	0.2125
Peripheral speed	122.2 fps	103.8	85.5
Axial flow velocity	24.0 fps	24.0	24.0
V_u , inlet	4.57 fps	5.38	6.53
ΔV_u	26.0 fps	30.65	37.20
C_l c/d	0.493	0.710	1.114
c	9.87 inches	8.95	8.26
c/d	1.795	1.92	2.15
C_l	0.275	0.370	0.519
ξ_t , axial extent	0.641	0.709	0.849
Diffusion factor	0.275	0.385	0.511
θ , tangential extent	157.3°	165.6°	180°
β_1	78°15'	76°18'	73°28'
β_2	76°51'	73°54'	68°56'
β_m	75°02'	70°29'	61°17'

where ξ_t is the value of ξ at the trailing edge of the foil.
In (26) a slightly closer expression was found to be

$$C_\theta = K_0 + K_1 \frac{\xi}{\xi_t} + K_2 \sin \left(2\pi \frac{\xi}{\xi_t} \right) \quad [13]$$

The streamline equation (which defines the streamline at each radius about which the isolated cambered blade shape must be placed) was thus found to be

$$\theta = \frac{\xi}{\phi} \left(1 - \frac{\lambda}{\eta} \right) - \frac{n\Gamma_b}{\phi r_t^2 \omega \eta} \left[K_0 \xi + \frac{K_1}{2} \frac{\xi^2}{\xi_t} - \frac{K_2}{2\pi} \xi_t \cos \left(2\pi \frac{\xi}{\xi_t} \right) \right] \quad [14]$$

where

$$\phi = \frac{V_f}{U_t} = \frac{V_f}{\omega r_t},$$

$$\lambda = \frac{V_{\theta_1}}{U_t} = \frac{V_{\theta_1}}{\omega r_t},$$

n = number of blades,

V_f = axial velocity,

V_{θ_1} = inlet tangential velocity,

η = r/r_t ,

ξ = z/r_t ,

Γ_b = circulation per blade, and

ω = rotational speed.

K_0 , K_1 and K_2 are based on total circulation for all blades. The values of K_0 , K_1 and K_2 for three radii are presented below:

r/r_t	K_0	K_1	K_2	ξ_t
0.70	0.0199	0.1875	0.010	0.849
0.85	0.0217	0.1441	0.010	0.709
1.00	0.0214	0.1162	0.008	0.641

A camber line of the NACA 65 series was chosen and a thickness distribution of the NACA 16 series was used. These distributions along with the above design procedure determined the final coordinates of the impeller blades.

Figure 24 shows the final blade profiles for the second stage and Figure 25 presents a view of the three-dimensional impeller as it appears when the sections are wrapped around the required 0.70 hub and in tandem with the 0.60 hub ratio five-term cambered first stage previously described.

4.3 Five-Term Cambered First Stage Tests

4.3.1 Overall Performance - The two-bladed first stage of Figure 22 was tested in the HYDRONAUTICS pump loop using the experimental techniques previously discussed. Figure 26 summarizes the overall performance of this stage with head coefficient as a function of suction specific speed. Note that significant improvement in the operating suction specific speed has been obtained as compared to the previous tests using constant pressure cambered sections (34). The design head coefficient

and suction specific speed have both been obtained, but at a flow coefficient of only about 80 percent of the design value. This is a reflection of the inability of the blades operating in a real three-dimensional flow to achieve the ideal two-dimensional lift coefficients theoretically predicted at the angles of attack and cavitation numbers predicted. With the resultant lower net head generation, the cavities do not see the static pressure rise necessary to terminate at a finite length and they slip into the infinite cavity range resulting in even less head generation.

A decrease in flow coefficient increases the angle of attack of the blades and thus the lift coefficient and head generation. As an example, consider the effect of changing the flow coefficient from 0.10 to 0.08 with the assumption of uniform inflow and constant rotative speed. In the present design, the design chord line angles of attack with uniform inflow for $\phi_0 = .10$ are $5^\circ 36'$, $6^\circ 30'$, and $8^\circ 36'$ at the hub, mid, and tip radii respectively (Table 3). Decreasing ϕ_0 to 0.08 while maintaining uniform would increase these values to $7^\circ 18'$, $8^\circ 40'$, and $11^\circ 26'$, respectively.

Figure 27 shows the radial variation of head generation and axial flow velocity for a typical data point. Note that both are non-uniform with maximum head generation occurring at the tip radius and considerably less at the mid and hub radii. The hub radius typically generates more head than the mid radius. These observations can be explained by the effects of the inflow velocity distribution and real fluid and three-dimensional effects

on the impeller. The boundary layer generated by the casing of the pump causes the local axial velocity to be reduced as indicated by the inflow velocity profile of Figure 27. This results in a local reduction of flow coefficient near the tip and thus a higher local head generation. The hub radius probably sees a lower angle of attack due to prerotation of the flow by the hub spinner ahead of the impeller, thus reducing the effective peripheral speed of the blade at the hub radius. This is verified by the tendency for the blades to remain fully wetted near the hub. Reduced angle of attack on a supercavitating blade causes a reduced head generation only to the point where the blade becomes fully wetted (base cavitating). The fully wetted section generates more head even though the angle of attack may be less. A boundary in Figure 26 shows the limit of fully supercavitating operation for the impeller and indicates a considerable region where the flow is not fully supercavitating. Cavity lengths reported are those of the base cavity as observed at the tip radius. When supercavitating, the three-dimensional variation of cavity length with radius is such that the cavities are longest at the tip and shorter at the hub with the collapsing region roughly paralleling the leading edge of the following blade.

Another effect of low impeller head generation results in face cavitation which occurs near the 40 percent chord. This almost always appears in varying degrees when the head coefficient is .03 or less. The region of occurrence is also indicated in Figure 26.

Photographs of typical cavitating performance are shown in Figures 28, 29, 30 and 31. In Figure 28 the flow conditions are:

$$\begin{aligned}\phi_o &= 0.10 \\ l/c &= 2.40 \\ \psi &= 0.055 \\ N_{ss} &= 20,500\end{aligned}$$

Note the clearly separate base and tip cavities trailing the blade and the fact that these cavities terminate at exactly the same point. The rotation is toward the bottom of the picture, flow from right to left, and the cavity to the left is the base cavity. The base cavity extends across the full radius while the tip cavity is confined to the region near the wall. Figure 29 shows the same flow condition. Note the extensive gap cavitation and the trailing cavities from the other blade in the lower left corner of the picture. Flow orientation is the same as in Figure 28. Figure 30 shows a similar view for the conditions:

$$\begin{aligned}\phi_o &= 0.10 \\ l/c &= 2.75 \\ \psi &= 0.036 \\ N_{ss} &= 25,700\end{aligned}$$

The tip and base cavities have merged at the wall and less gap cavitation is occurring. A transient detached cavity generated by one blade is collapsing near the trailing edge of the face of the other blade. Figure 31 shows the flow conditions:

$$\phi_o = 0.09$$

$$l/c = 3.10$$

$$\psi = 0.030$$

$$N_{ss} = 28,500$$

In this case the base and tip cavities are again merged and the base cavity shows a long collapsing region. Overall flow, however, is still steady.

Figure 32 presents the performance of the two-bladed model in terms of head coefficient versus NPSH. Flow coefficients, cavity lengths and regions of instability are all indicated on this figure. Using the data of Figure 32, Figure 33 may be constructed giving head coefficient as a function of flow coefficient, this is essentially the familiar head-discharge relation used in all pump characterization.

From the experimental results on the two-bladed model, it was apparent that the design goal head and suction specific speed requirements could not be met with the model at the required flow coefficient. Although significant improvement over the constant pressure cambered first stages (34) was achieved.

A model having the same blade profiles but with three blades instead of two was constructed in the belief that the higher solidity blades might improve head generation and thus delay breakdown to a higher N_{ss} value at higher flow coefficient. The blades were also reduced in pitch by 1° to allow higher flow coefficient

values with similar angles of attack. Figure 34 shows the resulting three-bladed, five-term cambered first stage. The suction performance obtained from pump loop tests is indicated in Figure 35 where head coefficient is presented as a function of N_{ss} . As in Figure 26 for the two bladed model, cavity lengths and regions of various cavitation patterns are indicated. A phenomenon not noted for the two bladed model (but referred to in Reference 4) was found in the three bladed case. This was the existence of a large region of unequal cavity lengths (i.e. the lengths of the cavities on all three blades were not equal). In most cases two cavities were of one length and the third either shorter or longer. In a few cases, however, all three were slightly different. The maximum deviation in l/c among the blades during testing amounted to only about 20 percent and was typically less than 10 percent. The phenomena is felt to be hydrodynamic in nature and related to the cascade effect rather than physical differences in the three blades. The variations in the pattern could not be predicted to occur on any particular blade, and a check of the "as-built" geometry showed deviations among the three to be insignificant. The base cavity lengths reported in the region of unequal lengths are the averages of the lengths observed at the particular operating condition.

As is readily observed on comparison of Figures 35 and 26, the addition of a third blade greatly increased the head generation of the model at low N_{ss} values. The breakdown N_{ss} values

for all flow coefficients, however, were reduced. The region of face cavitation was increased substantially in spite of increased head generation. The lengths of base cavities before breakdown were also reduced. As for the two bladed model, Figure 36 presents the variation in head coefficient with NPSH for the three bladed model. From this a head coefficient versus flow coefficient (head-discharge) relationship may be constructed as shown in Figure 37.

Figures 38 and 39 indicate lines of constant hydraulic efficiency superimposed on a grid of head coefficient versus NPSH for the two and three bladed models respectively. Efficiencies typically range from 30 to 60 percent over the operating range. The efficiency near the design goal is shown to be only 35 - 40 percent. This is quite low, illustrating the feasibility of using such supercavitating turbomachinery in applications only where cavitation is unavoidable and where efficiency is secondary to stability requirements. It should be remembered when considering the efficiency of Stage 1, however, that the overall efficiency of the tandem inducer when stage 2 is employed will be significantly higher due to the more efficient subcavitating second stage sections and the higher percentage of the total head generation provided by that stage. The constant pressure cambered first stages of Phase I (34) also had typical efficiencies in the range of 35-40 percent, however the tandem model achieved a fairly respectable 65 percent at the operating point.

Figure 40 presents typical outlet axial velocity distributions from the five-term cambered models. Figure 40(a) for the two bladed model at $\phi_o = .10$, illustrates that, except at the tip radius, suction specific speed had little effect on the axial outlet velocity profile. The outlet profile, due to radial gradients, is not uniform at 19.10 fps as assumed, but rather the axial velocity increases from hub to tip with some boundary layer effects modifying the hub and tip regions. A linear outlet velocity distribution varying from 14.4 fps at the hub to 23.0 at the tip better characterizes the outflow velocity profile at $\phi_o = 0.10$ as shown in Figure 40(a). It should be noted that none of the data of 40(a) is in the fully supercavitating flow regime but, rather, has partial back cavities. Figure 40(b) illustrates the effect of flow coefficient, ϕ_o , on outlet axial velocity profiles for the same model at relatively high values of suction specific speed ranging from 24,000 to 29,500. At low values of ϕ_o (0.07 - 0.08) the outflow velocity is relatively uniform becoming more non-uniform as the flow coefficient is increased. As ϕ_o is increased, however, the flow regime changes from the fully supercavitating to partially cavitating flow condition where the flow is fully cavitating at the tip, but base cavitating (with fully wetted back) at the hub with a range of conditions at intermediate radii. Figure 40(c) presents similar data for the three bladed model over a wider range of flow coefficients, a trend similar to the two bladed model is apparent. All of the data except at the 0.12 flow coefficient was in the fully supercavitating range. It

is apparent from the data of Figure 40 that the outlet axial flow velocity profiles are strongly dependent on the flow coefficient and that when fully supercavitating flow is maintained, the outlet velocity profile is relatively uniform. As the value of ϕ_0 is increased and the partially back cavitating mode of operation is entered, the flow becomes more non-uniform with considerably more flow in the tip region than at the hub.

Figure 41 illustrates typical radial variation of total head both upstream and downstream of the two and three bladed inducers at a flow coefficient of 0.09 and a variety of suction specific speeds. The outlet total head variation for all N_{ss} values and for both models is similar with a higher value at the tip than at the hub. Higher N_{ss} values of course result in lower total head rise as shown in Figures 26 and 35. The deviation from head to tip expressed as a percentage of the tip total head varies from 9 percent to 28 percent with most of the data between 15 percent and 25 percent.

4.3.2 Quasi Two-Dimensional Performance at Mid-Span - In order to obtain a representative performance sample approximating two dimensional flow conditions, the data taken at the mid-span and one station to either side of mid-span were averaged. These values are presented in the following section and are referred to as mid-span characteristics. Figure 42(a) presents the mid-span lift coefficient as a function of chord line angle of attack for the two bladed, five-term cambered model. The mid-span physical characteristics for this model are:

$$\bar{k} = 0.210$$

$$c/d = 0.521$$

Lines of constant local cavitation number, σ , are indicated on the plot and fully supercavitating points are indicated as compared to those data not at fully supercavitating conditions. In Figure 42(b) the ratio of C_L/σ is plotted against chord line angle of attack. The data tends to be collapsed by this representation but cannot be adequately represented by a single curve. Figures 43(a) and (b) present similar results for the mid-span characteristics of the three bladed five term cambered model. The mid-span characteristics for this model are: $\bar{k} = 0.210$, $c/d = 0.781$. Comparing Figure 43(a) to 42(a), the effect of increased solidity on reducing lift coefficient (per blade) is apparent when curves with equal cavitation numbers are compared. Flow breakdown occurs at higher angles of attack for the three bladed model. In Figure 43(b), a significant change in variation of C_L/σ with chord line angle of attack for the higher solidity of the three bladed model can be easily seen when compared to 42(b) for the two bladed model.

Figures 44, 45, 46, and 47 compare only the data in the fully supercavitating or nearly fully supercavitating range to the first and second order theoretical predictions using the results of (28). In addition, a simplified result given by Reference 47 in which the lift coefficient of a cascade at $\sigma = 0$ is calculated by analogy to flow past a supercavitating isolated foil at $\sigma = 0$ (infinite cavity length) operating over a free

surface. The present solidity and stagger angles far exceed those intended to be represented by the analogy of (47) and the results are presented here for comparison to the present calculated results only.

It may be concluded from the results presented in Figures 44 thru 47 that, while some deviation is apparent between the experimental and theoretical results, the theory (28) reasonably calculates the cascade lift performance for those conditions which are nearly two-dimensional and fully supercavitating. The higher cavitation number and, therefore, not fully supercavitating data shown in Figures 42 and 43 are of course not well predicted by the theory since the basic assumption of a supercavitating flow is not satisfied. The data of Figures 42 and 43 indicate, as would be expected, that higher lift coefficients are obtained in partially or fully wetted flow conditions. The severe face cavitation noted for several data points in Figures 44 thru 47 resulted in significant lift reduction and deviation from the predicted performance.

4.3.3 Stability Analysis - There are numerous possible sources of the observed instabilities in cavitating inducers. Among the primary possibilities are: (1) unstable interaction of tip and base cavities with adjacent blades, (2) unsteady location of the cavity separation point near the leading edge of the blade, (3) interaction of the inducer with the hydrodynamic and hydro-elastic properties of the load, (4) leading edge flutter, and (5) travelling circumferential distortion or rotating stall.

Some detailed discussion of these is given in Reference 23. Of these causes, the last was originally selected as the one most amenable to analytic study and use in the design procedure. It was this type of instability which was used to determine the distribution of head between the first and second inducer stages as mentioned in Section 2.1.

Rotating stall in axial-flow compressor operation occurs at low flows and consequent high angles of flow incidence. This phenomenon has been studied experimentally and analytically by several investigators and has been summarized in Reference 48. A brief description is as follows. As blade rows approach stall, the flow separates in some groups of blades. The stalled blade restricts the flow through the channel adjacent to its upper surface and in consequence the fluid is deflected around the blocked channel, increasing the angle of incidence on the blade above and decreasing the angle of incidence on the blade below so that these patterns of stalled and unstalled flow do not remain fixed but are propagated along the cascade. The result is that the blade rows are subjected to violent periodic dynamic loads, since they find themselves alternately in stalled and unstalled flow.

Various theories concerning the problem of rotating stall have been proposed, the majority of which use a small perturbation approach, and therefore, apply strictly only to an incipient stall. A recent analysis due to Yeh (16) treats the problem on the basis of classical actuator disc theory. It was found (16) that, in general, both a traveling circumferential distortion

and a spanwise type self-induced distortion are possible, and that the purely traveling circumferential type would in all probability occur first. Restricting the analysis to this type simplifies the problem enormously. The conditions required for the purely circumferential type self-induced distortion to occur are shown to be

$$M = [1 + \tan^2 \beta_2 + N(1 - \tan \beta_1 \tan \beta_2)] / \tan \beta_1 \quad [15]$$

$$K = [1 + \tan^2 \beta_2 + N(1 + \tan^2 \beta_1)] / (2 \tan \beta_1) \quad [16]$$

where

M is defined as $\frac{1}{2} \frac{\Delta \omega_1}{\Delta \beta_1}$,

N is defined as $\frac{\Delta \tan \beta_2}{\Delta \tan \beta_1}$,

β_1, β_2 are the relative flow angles, upstream and downstream of cascade,

K is the ratio of the speed of distortion propagation to the axial component of inlet velocity, and

ω_1 is the head loss coefficient $\frac{2gH_L}{U_o^2}$.

Equation [15] can be applied directly to the stability of a supercavitating impeller. All of the parameters in the equation can be obtained from theoretical cascade performance (18, 28). The values of M and N are obtained graphically and if the design is shown to be unstable, the design parameters are adjusted and the stability procedure repeated until a stable impeller design is obtained.

The maximum allowable head coefficient will be stability-controlled. The higher the head coefficient, the larger the lift and drag coefficients and hence the larger the value of M_{cascade} . As the solidity increases, the value of N is reduced, consequently increasing M_{limit} . However, the increase in M_{cascade} is much steeper than the increase in M_{limit} and at some value of head coefficient, ψ , the flow through the impeller will become unstable. In Reference 34 the constant pressure cambered supercavitating first stage was initially designed to produce 0.25 of the total inducer head coefficient. However, when the stability criterion was applied to this design, it was found that the flow through the impeller would be unstable. A second design was conducted in which the first stage head coefficient was 0.20 of the total inducer head coefficient. Once again, Yeh's stability analysis showed that the flow through the impeller would be unstable. A third design was initiated with a design head coefficient 0.15 of the total inducer head coefficient. For this value of 0.15, the stability analysis showed that the impeller was stable.

The present two bladed five-term cambered first stage was also designed so that theoretically 0.15 of the total inducer head coefficient was produced by the first stage. The Yeh stability analysis at the mid radius showed the design to be nominally stable ($M/M_L \approx 1.0$). This distribution of head was therefore retained for the five-term cambered model.

After the experimental program was conducted all data for both the two and three bladed five term cambered models were analysed to determine the true influence of the Yeh criterion on incipient instabilities. The parameters, β , β_2 , ω and σ for the mid three radii (2.55, 2.80, and 3.05 inches) were averaged to reduce the random error of the measurements. All data were then grouped by σ range into three groups $\sigma = 0$ to .035, .035 to .090, and .090 to .175. These groupings made it possible to graphically use the data for the determination of the derivatives required in stability analysis. Figures 48(a) and 48(b) show the plots of ω versus β_1 and $\tan \beta_2$ versus $\tan \beta_1$ used in the stability analysis of the two-bladed five-term cambered first stage. The symbols indicate the σ group of each data point. With few exceptions, the data are rather clearly separated by this procedure. Similar plots were prepared for the three-bladed model. If the Yeh criterion for incipient instability through the mechanism of rotating stall truly determines the onset of this type of instability and if the instability observed in the present supercavitating inducers is related to the rotating stall phenomenon, the ratio of M/M_L should steadily approach 1.0 or at least steadily increase as the boundary of the unstable region is approached.

Figure 49 and 50 show the head coefficient, ψ , as a function of NPSH for the two-bladed and three bladed models respectively. Beside each data point the ratio of M/M_L for that point is indicated. While the relatively stable high NPSH regions do show

small M/M_L ratios, there is apparently no good correlation between this ratio and the proximity of a data point to the unstable region. In fact many data points near the unstable boundary have M/M_L ratios smaller than data points further away in highly stable regions.

One must, therefore, conclude that the Yeh stability criterion does not adequately predict incipient instabilities in the cavitating flows under consideration. It is unlikely, therefore, that the rotating stall mechanism is responsible for the observed large magnitude low frequency instabilities in the cavitating inducers presently under consideration. However, it seems probable that flow oscillations are strongly related to the basic cascade flow geometry. The suction and discharge systems do not, at present, appear to be the cause of such oscillations but may have a significant influence on the frequency or amplitude of the oscillations once they are generated.

4.3.4 Mechanism of Flow Instability - The question then arises - what is the physical mechanism of the flow instability if not rotating stall? The data for the five term cambered models indicate that two requirements are necessary for the region of severe instabilities to occur. The first of these is a flow coefficient below a certain minimum. Figure 32 indicates that for the region of instabilities to occur for the two bladed model the flow coefficient must be below 0.09. In a similar way, Figure 36 indicates that the flow coefficient must be .075 or below for instabilities to occur on the three bladed model. In addition, these figures indicate that the region of instabilities

lies in a rather well defined cavity length region. For the two bladed model it occurs at about $l/c = 2.40$ while for the three bladed model it occurs between $l/c = 1.80$ and 2.00 . Figure 51 indicates schematically that the cavity lengths mentioned above correspond to those operating points at which the cavity collapsing from one blade extends back to or slightly past the leading edge of the adjacent blade. Extending to this location, by itself, is not a sufficient condition to insure interference instabilities. The flow condition must also include a low enough flow coefficient to provide a relatively thick cavity at the adjacent blade. Recall that lower flow coefficients correspond to higher angles of attack and therefore higher head generation coupled with thicker cavities (not necessarily longer cavities since higher head generation may terminate them). For shorter cavities, no strong oscillations were observed. As the cavity length increased beyond the critical length, choking and head breakdown rapidly follow.

Details of the magnitude and frequencies of the head fluctuations in the relatively stable regions are discussed in Section 4.3.5.

From the available data it seems that an instability in cavity length due to interactions between the cavity and the inflow to the next or adjacent blade is the source of the region of severe flow instability. The observation that instabilities occur when the cavity enters the gap formed with an adjacent blade was also noted by Acosta (49) and Soltis (7). The details of how the instability occurs may be as follows:

1. As the flow coefficient is reduced toward a critical value, the cavity grows in thickness and length depending on NPSH variation until its collapse occurs at or near the gap formed by the adjacent blade.

2. If the flow coefficient is further reduced below the critical value (actually ϕ_0 and NPSH will both vary), the increase in cavity length and thickness causes a serious blockage which results in reduced inflow and thus a further reduction in flow coefficient. In this region the process is unstable and cavity length grows rapidly.

3. The exact mechanism for a limit cycle process is not certain. As cavity thickness and length increase and flow coefficient decreases, head may begin to increase, causing a collapse of the cavity. One alternate cause of cavity collapse may be the complete breakdown of head and flow, followed by reestablishment of an unstable flow.

In Figure 33 for the two bladed inducer, note that as the region of instability is approached the head approaches a constant value and the cavity length appears to reach a minimum. The same trend is indicated in Figure 37 for the three bladed model. A possible variation of cavity length with flow coefficient (at constant NPSH) is shown in Figure 52. In the unstable region cavity length appears to increase rapidly with decreasing flow coefficient, a highly unstable condition.

The oscillation of the flow (and cavity length) appears to be of the limit cycle type. Once instability occurs, the cavity length begins to grow very rapidly; this growth is terminated either by complete blockage ($\phi \rightarrow 0$) and reestablishment of the flow or by a sudden decrease in cavity length with decreasing flow coefficient (as shown in Figure 52). In the first case limit cycle type oscillations are certain. In the second it seems likely that the process will be dynamically unstable so that limit cycle type oscillations between the boundaries of the unstable region will occur.

Wood (50) indicates that flow oscillations observed in mixed flow pumps designed for high suction specific speeds appear to be due to growth of tip vortex cavities into the gap between blades. Hartmann and Soltis (5) have also attributed observed flow oscillations in low hub-tip ratio axial flow pumps to growth of tip vortex cavities. Neither of these pumps is typical of the axial inducer pumps used in space applications. For the pumps tested by Acosta, Iura and others, there is no indication that tip vortex cavities are the primary source of flow oscillations. In the present tests, it was generally not possible to separate tip vortex cavity behavior from blade cavity behavior. The two types of cavity flow appear to be closely related for typical inducer pumps so that it is probably unnecessary to fully differentiate between the roles of these cavities.

Acosta and Wade (49) found that flow oscillations occurred at nearly constant Strouhal number (based on chord) of approximately 0.10. This result is comparable to that for a similar

isolated foil and is further indication of the isolated behavior of the foil under oscillatory conditions.

It seems probable that flow oscillations that occur in inducer pumps may occur at several Strouhal numbers. The present tests also indicate that in the region of severe instability, oscillations occur at Strouhal numbers less than those observed by Wade and Acosta. It is quite possible, however, that the Strouhal number for cascades with high solidity or stagger should be based on some other characteristic length such as cavity length. It is also possible, in view of the proposed mechanisms of flow oscillation, that the suction and perhaps the discharge systems have an effect on the frequency of oscillation.

There is no means of analyzing the effect of the test facilities on observed flow oscillations. It seems unlikely, however, that these facilities could be the source of such oscillations, however the facilities may effect the frequency and the amplitude of the oscillations. Disturbances in the inflow to the pumps may also contribute to initiating the oscillatory flow. For operational pumps, say in large booster rockets, the suction and discharge systems probably can effect the magnitude and region of flow oscillations.

From the foregoing discussion, it may be concluded that the observed flow instabilities and oscillations are probably due to interactions of the cavities with adjacent blades at critical cavity lengths and thicknesses. Because of the complex flow occurring when a cavity collapses at or near the entrance to the

gap formed by an adjacent blade, the blade cavity length and pump head characteristics may be the inverse of those normally observed and inherently unstable. This instability is probably of the limit cycle type, the cavity length and head oscillating between relatively fixed boundaries.

4.3.5 Pressure Fluctuations in the "Stable" Region - During Phase III, when testing the five-term-camber supercavitating first stages in isolation, the range of pressure fluctuation frequencies of interest was restricted to 0-100 cps. This was due to the importance of this frequency range in exciting fluctuations in the rocket propulsion and structural systems. For the Saturn V, NASA indicated the particularly critical ranges were 10-15 cps and 28-35 cps.

The tests of the two and three bladed five-term cambered first stage models as presented in Figures 26 and 35 indicated that a large region of stable operation existed extending roughly from 12,000 to 30,000 suction specific speed and from flow coefficients of 0.12 to 0.07. Some acceptable operation was maintained as low as flow coefficient = 0.05. There were regions of severe pressure fluctuations for various combinations of suction specific speed and flow coefficient. These have been discussed in detail in Section 4.3.4 and a mechanism for the instabilities postulated. In the large "stable" region of operation, pressure fluctuation spectrums were obtained in the 0-100 cps range. Figure 53 presents typical spectrums of the pressure fluctuations for the three-bladed five-term cambered model. In addition the

envelope of all spectral data for this model is indicated. As can be seen the fluctuations generally peaked at two frequency values, one in the vicinity of 20 cps and the other near 85 cps. (The lower frequency peak actually varied from 10 to 28 cps and the higher from 75 to 95 cps). In the large stable region of operation, the peak in the 85 cps vicinity never exceeded 4 percent of the first stage head generated. The peak in the 20 cps vicinity varied from 2 percent to 10 percent of the head generated, never exceeding 5 percent at suction specific speeds of 22,000 or less.

Figure 54 presents the ratio of fluctuating head to total head generated in percent as a function of the average cavity length to chord ratio (l/c) for the three bladed model. The correlation is rather good with the region of minimum fluctuations occurring in the vicinity of $l/c = 1.4$. The increase at longer cavity lengths is more a result of lower head generation by the stage than increased absolute amplitude of the pressure fluctuations. The dotted increase toward $l/c = 1.0$ is speculated based on experience with isolated foils and the Phase I tests (34) where fluctuations over the range 0-10,000 cps peaked near $l/c = 1.0$. The data presented may be taken as typical for both the three and two bladed models.

No tandem tests involving a five term cambered supercavitating first stage were conducted. The results of the Phase I tests, however, indicate that the overall performance of the tandem pair would be improved (i.e. the pressure fluctuation would be lower) over that of the first stage alone when expressed as a

percentage of the total head generated. During the Phase I tests, the entire frequency spectrum of 0-10,000 cps was examined and insufficient resolution in the 0-100 cps range was available for details of this range to be examined. However, Phase I tests of the isolated constant pressure cambered first stage indicated a total pressure fluctuation level at a flow coefficient of 0.10 over the frequency range of 0-10,000 cps of less than 5 percent in the suction specific speed ranges of less than 12,000 and 14,000 to 21,500. In the narrow band between 12,000 and 14,000 the fluctuation level reached 10 percent of the head generated. This corresponded to a cavity length-chord ratio of about 1.0. Beyond 21,500 another increase was registered toward breakdown. Isolated tests of the final second stage during Phase I indicated a pressure fluctuation level of less than 2 percent over the range of suction specific speed values from 10,000 to 19,000. The corresponding flow coefficient range was .074 to .097. When tested in tandem, the total pressure fluctuation for the Phase I models expressed as a percentage of the total head generated by both stages for the range of flow coefficient of 0.072 to 0.085 was never in excess of 5 percent except near breakdown ($N_{ss} > 23,000$).

No detailed data were available for fluctuating pressures from a conventional (helical) inducer with which to compare the tandem results reported.

It is concluded that a tandem inducer using a supercavitating first stage and subcavitating second stage may be designed to operate over a fairly wide range of suction specific speeds (models

operated at 10,000 - 30,000 in water) and flow coefficients (models operated at .12 - .07) with pressure fluctuations of less than 10 percent of the head generated. The influence of the remainder of the hydraulic system (including main fuel pump) on damping or amplifying this level cannot presently be predicted. In addition, the number of inducer models tested has been quite limited and these have been tested only in room temperature water. The thermodynamic effects of cavitation in cryogenic fluids will raise the range of operating suction specific speeds to higher values.

4.3.6 Cavitation Damage - As previously noted and as mentioned in Reference 3 for "conventional" rockets, cavitation damage to the turbopumps is not a serious problem due to the short period of operation. This is not true, however, for the space shuttle application where components are required to be reusable. This is discussed in Appendix B.

Cavitation damage results when vaporous cavitation bubbles collapse in proximity to a surface with sufficient force to deform or erode that surface. The collapse usually occurs when the cavities or bubbles are carried by the flow into a region of higher local pressure. The collapse of a spherical bubble was first theoretically formulated by Raleigh (53) in 1917 and recently a great deal of research has been conducted on how to reduce cavitation damage to various materials, primarily metals, and to classify and understand their relative resistance to damage (54,55,56,57,58,59,60). Not even the hardest metals

available can entirely resist the erosive force. Experimental and theoretical investigations of the problem indicates that pressures of 200,000 to 300,000 psi or higher may be generated during collapse. The repeated collapse of bubbles with these forces causes a type of fatigue failure of the surface.

Figure 55 shows a photograph of cavitation damage to the trailing edge of the suction side of a Phase I model. The characteristic pitting caused by cavitation is evident. Figure 56 shows the damage to the test section of the pump loop which occurred during Phase I testing. The casing of a prototype would eventually suffer the same type of damage. Figure 57 shows the beginning of cavitation pitting of the face of the five term model of Phase III. This damage resulted primarily from the collapse of cavities trailing the adjacent blade as shown in Figures 30 and 31.

As related in Appendix B, some research into the damage resistance of materials in cryogenic fluids is almost certainly required to provide guidance in inducer designs for the proposed shuttle vehicle where prolonged life and higher rotative speeds are required.

5.0 SUMMARY

The suction specific speed (N_{ss}) is the parameter used to characterize the inlet operating conditions for a pump. For a given discharge, high suction specific speed results when either rotational speed is increased or NPSH is decreased. Both changes result in significant weight reductions when the pumps under consideration are fuel or oxidizer pumps in a liquid fueled rocket engine system. Prepumping stages called "inducers" are presently located ahead of the main fuel pumps. The inducers operate rather satisfactorily even with extensive cavitation and provide sufficient head rise so that the main pumps may operate non-cavitating.

A typical inducer consists of a high solidity axial flow impeller with a small number of blades operating on the same shaft and at the same rpm as the main pump. The blade form usually approximates a simple helix. While severely cavitating, cavitation damage and low efficiency are not particularly restrictive in "conventional" applications since the operating period is very short and the head generated by the inducer is only a small portion of the total. The problem of flow instabilities, however, is very significant as a limiting condition for acceptable inducer operation. Under certain conditions instabilities in the flow may cause engine thrust fluctuations. The resulting unsteady motions provide an unacceptable environment for delicate equipment and astronaut crews. In addition, low frequency oscillations may occur at or near the structural natural frequency.

The tandem row inducer has been suggested as one method for reducing or eliminating the instability problem. The first stage operates at the design suction specific speed but delivers only a fraction of the total head rise. The second stage thus operates at a lower N_{ss} and delivers the remaining head with greater stability.

The present study was conducted in water rather than the cryogenic fluids of the prototypes. Thermodynamic effects in cryogenics tend to make modelling in water a conservative procedure. For the same reasons, cavitation patterns in cryogenics will occur at lower bulk cavitation numbers, (higher N_{ss} values) than similar patterns in water.

A supercavitating first stage was chosen due to studies indicating that to produce the required head, cavities on the back side of the blades would be in excess of 30 percent of the chord length and unstable. Long cavities (supercavitation) are known to be a more stable operating condition.

A generalized theory of rotating stall (16) was chosen to determine the allowable head rise in the first stage of the tandem row inducer. Rotating stall was speculated to be another source of instability in addition to the unstable cavity lengths previously mentioned.

The performance of supercavitating cascades of constant pressure cambered foils was theoretically studied by the use of potential theory (18, 19). Using these results, a supercavitating

first stage was designed using a free vortex-blade element approach (34,51,52) where the variation of head generated with radius is assumed to be constant.

The second or subcavitating stage was designed using the approach of (24) which requires no cascade data and which accounts for induced interference effects at the impeller blade as influenced by the other blades and the total pump vorticity.

An initial design for the two stage inducer utilizing a cylindrical 60 percent hub/diameter ratio, a two bladed constant pressure cambered supercavitating first stage (characteristic $c/d = .540$), and a six bladed high solidity ($c/d = 2.43$) second stage having NACA camber and thickness distributions was obtained. The design point overall performance requirements were:

flow coefficient, $\phi_o = 0.10$

head coefficient, $\psi = 0.25$

suction specific speed, $N_{ss} = 30,000$

The stability analysis (16) indicated that 15 percent of the total inducer head could be provided by the first stage at the design point and still maintain stable operation.

An experimental pump test loop (see Figure 4) was used to test the model. The loop had a plexiglas test section for observation of cavitating operation and the capacity to operate at reduced pressure to model N_{ss} . Direction sensitive velocity probes were used to provide radial surveys of the pressure, velocity and flow direction both upstream and downstream of the

models. (see Figure 5). The test procedure adopted was to hold flow coefficient constant and to reduce NPSH (increase N_{ss}) until flow breakdown with data taken at arbitrary points along the performance curve.

The test program (34) indicated that for optimum performance both stages required empirical modification. Several modifications were tried and the final best performance was obtained by the use of a three-bladed first stage ($c/d = .810$) at the original design pitch and a six-bladed second stage at 10° less than the original design pitch. These stages were then tested in tandem with -6 inch and -1.5 inch overlaps (see Figures 7,8,9 and 10). Little difference was noted in the performance at the two overlaps. To compare the experimental performance to the original design requirement, the point at which the required head distribution (15 percent first, 85 percent second) occurred was chosen.

The tandem model produced more than the required head coefficient (.29/.25) at less than the design flow coefficient (.083/.100) and less than the design suction specific speed (22,000/30,000). The first stage cavity lengths at this point were approximately as required by the original design (1.50-1.75/1.50). Low frequency oscillations or instabilities were noted at breakdown but were attributed to unstable cavity lengths rather than rotating stall. In the stable region, pressure fluctuations over the range 0-10,000 cps were generally less than 5 percent of the head generated. The trade-off in head generation between the first and second stages produced a relatively flat ψ vs. N_{ss} characteristic.

The experimental performance, while not quite reaching the the design objectives, did indicate that the tandem inducer having a supercavitating first stage had definite potential as a high N_{ss} design concept.

Further manipulation of the pitch of the tandem inducer stages (in particular smaller pitch angles for Stage 1) may have reduced the head coefficient and increased the flow coefficient bringing each closer to the design values. This would probably have resulted in higher breakdown N_{ss} values because of the smaller angles of attack. It was concluded however, that with the constant pressure cambered blade shapes, it was doubtful that the design goal of 30,000 could be reached. One characteristic of constant pressure cambered cascades is that as the solidity is increased, the camber of the foil decreases approaching a flat plate. This is detrimental to the stability of the flow since flat plate profiles create a higher drag for the same lift than cambered profiles. The flat plate must rely entirely on angle of attack for lift generation. It was, therefore, apparent that the characteristics of supercavitating cascades having other than constant pressure camber were required. The second stage performance indicated the need for extension of the design capabilities of Reference 24. In particular, the velocities induced by a radial line vortex in an annulus (25) needed to be calculated for smaller axial and circumferential spacings and for larger hub/diameter ratios.

The theoretical performance of supercavitating cascades having other than constant pressure cambers was formulated (28) and the performance of numerous cascades calculated. The types of blades considered were those obtained by Johnson (27) and included circular arc, two-term, three-term and five-term cambers. The higher the number of terms in the camber distribution, the further aft the center of pressure is shifted. A comparison to the results of (18) indicated that the results of (28) were more conservative (i.e., more camber and angle of attack are required for the same lift than in the constant pressure results). This is in agreement with the experimental results on the Phase I models. A comparison of the results of (28) to experimental supercavitating cascade characteristics was difficult since almost no reliable data exists. A study of the influence of camber type on cascade performance indicated that the five-term cambered shape should be adopted for future first stage designs.

A formulation of the problem of partially cavitating cascades of cambered blades was conducted and published (36) for future use in the off-design performance of turbomachinery and for partially cavitating design use.

A theoretical study of the three-dimensional flow field generated by a radial vortex filament in a cylindrical annulus (42) was conducted as an extension of the second stage design capability. Considerable disagreement was found between these results and the results of Reference 25 except at mid radius. Sample streamline calculations showed that for hub/diameter

ratios in excess of 0.70, the three-dimensional results are not required and a simpler two-dimensional approximation may be used.

A number of five-term cambered supercavitating first stage designs were considered using the theoretical results of (28) and the approach of free vortex design and blade element theory. The overall inducer requirements were taken to be the same as for the constant pressure cambered case previously described.

Among the five term cambered cases considered were two and three bladed designs using first order and approximate second order (26) results having:

- (a) specified linear C_L variation with radius
- (b) constant chord length with radius
- (c) constant solidity with radius (radial leading and trailing edges)
- (d) specified linear chord length variation with radius

The two bladed, second order, constant chord length design was chosen. Lining up the trailing edges in a radial direction results in a swept leading edge. The swept leading edge has been shown (4) to have certain advantages with regard to stability and in addition has definite structural advantages. The swept or spiral leading edge has also been used in a number of operational rocket engine inducers including the J-2 and F-1 engines for the Saturn V launch vehicle. The design, assigning 15 percent of the total head rise to the first stage was shown to be marginally stable at the design point and mid-radius using the criteria of (16).

A helical back surface was used for the model and structural consideration based on chordwise bending stresses at 20 percent of the chord from the leading edge showed structural compatibility with prototype inducers having the diameter and rpm ranges of the Saturn V inducers when the prototype design stress is 50,000 psi.

Using the newly calculated results for the radial vortex filament in an annular space (42), numerous second (subcavitating) stage designs were considered using the design technique of (24). The design chosen utilized 5 blades and a 0.70 hub/diameter ratio. Six vortices per blade were used in the design procedure and the NACA 65 series camber and 16-009 thickness function were used to arrive at the final blade profiles (see Figure 24).

The two bladed, five-term cambered first stage was manufactured and tested in the pump test loop (see Figure 22). Significant improvement was achieved over the performance of the constant pressure cambered first stage previously investigated (see Figure 26). The design head coefficient (15 percent of .25) and suction specific speed (30,000) were both achieved but at a flow coefficient of only 80 percent of the design value.

A large region of partially cavitating (spanwise direction) flow was noted with the tip becoming supercavitating before the hub. Tip cavities were sometimes separate and sometimes merged to the base cavities (see Figures 28 and 30). In either case, they tended to collapse at the same point as the base cavities. The variation in the base cavity length when fully cavitating was such that the closure of the cavity paralleled the leading

edge of the following blade. A region of severe, instabilities and regions having various cavitation patterns including some face cavitation were found to be present (see Figure 26).

From the experimental results on the two bladed five-term model it seemed apparent that the design goal head coefficient and suction specific speed could not be met with this model at the required flow coefficient of 0.10. However, significant improvement over the best first stage model having constant pressure camber was achieved. Most notably, the operating N_{ss} value increased from 22,000 to 30,000.

A first stage model having the same blade profiles but with three blades was constructed in the belief that the higher solidity blades might improve overall head generation and thus delay breakdown to a higher N_{ss} value at a higher flow coefficient. The blades were also reduced in pitch by 1° to increase the flow coefficient operating range. The resulting three bladed five-term cambered first stage was manufactured and tested in the pump test loop. The addition of the third blade greatly increased the head generation at low N_{ss} values, but reduced the breakdown N_{ss} value at all flow coefficients (see Figure 35). The region of face cavitation was increased in spite of increased head generation and the base cavity lengths before breakdown were reduced. The phenomenon of unequal cavity lengths was also noted for this model.

Near the design flow coefficient (.10) the outlet axial velocity profiles were rather non-uniform with the velocity increasing from hub to tip with some boundary layer effects modifying the distribution. Suction specific speed had little effect on axial velocity profile but flow coefficient influenced it quite strongly. At lower flow coefficients where the flow was fully supercavitating the axial profile was much more uniform (see Figure 40). Typical total head generations varied by 15 to 25 percent with radial location with the higher values near the tip.

Analysis of the blade element performance of the two and three bladed five term cambered models at the midspan of the blade when operating in the fully supercavitating mode indicated that the theory (28) reasonably calculates the cascade lift performance when the basic assumption (fully supercavitating) is met. (See Figures 44, 45, 46 and 47). The partially cavitating or non-cavitating data at midspan indicates higher lift coefficients than when supercavitating as would be expected. Face cavitating conditions resulted in lift reduction.

Using the stability analysis techniques of (16) the experimental data for the two and three-bladed, five-term cambered models was analyzed at midspan. According to (16) the onset of rotating stall type instabilities should occur when the ratio of the parameters M/M_L approaches 1.0. If this type of instability is responsible for the regions of instabilities noted in the model tests, the ratio M/M_L should thus approach 1.0 or at

least steadily increase as the boundary of the unstable region is approached. This was not found to be so. It was thus concluded that the criterion of (16) did not adequately predict the onset of incipient instabilities in the cavity flows under consideration and, therefore, that the rotating stall mechanism was not responsible for the large magnitude, low frequency oscillations observed in the cavitating inducers studied.

Analysis of the cavity length data for both models indicated that, provided the flow coefficient was below a certain critical value, the region of severe oscillations corresponded to that operating condition where the cavity collapsing from one blade extends back to or slightly beyond the leading edge of the adjacent blade. The oscillation of the flow in the unstable region appears to be of the limit cycle type, but the exact mechanism is uncertain. From the analysis, however, it may be concluded that the oscillations are probably due to the interaction of the cavities with adjacent blades at critical cavity lengths and thicknesses. Because of the complex flow at the entrance to the gap formed by the adjacent blade, the cavity length-head relationship may be inherently unstable leading to cavity length oscillation between fixed boundaries.

In the large "stable" region of operation, an analysis of the magnitude and frequency of oscillations in the 0-100 cps range indicates that peaks occur in the vicinity of 20 cps and 85 cps. Neither pressure peak exceeded 10 percent of the head generated by the first stage and the N_{ss} values of 22,000 or less neither exceeded 5 percent. Correlation with l/c indicated a minimum at about $l/c = 1.40$.

No tandem tests were conducted using a five-term cambered first stage, however, the results of pressure fluctuation measurements on tandem tests during Phase I indicate that the overall pressure fluctuation level in the tandem configuration will be much lower when expressed as a percentage of total inducer head. This is due to the relatively smaller fluctuations of the second stage and the higher portion of the total head generated by that stage.

It is concluded that a tandem inducer using a supercavitating first stage and subcavitating second stage may be designed to operate over a fairly wide range of suction specific speeds (models operated at 10,000 - 30,000 in water) and flow coefficients (models operated at .12 - .07) with pressure fluctuations of less than 10 percent of the head generated.

The influence of the remainder of the hydraulic system (including main fuel pump) on damping or amplifying this level cannot presently be predicted. In addition, the number of inducer models tested has been quite limited and these have been tested only in room temperature water. The thermodynamic effects of cavitation in cryogenic fluids will raise the range of operating suction specific speeds to higher values.

Appendix A provides a summary of the inducer performance characteristics during a flight of the Saturn V launch vehicle using the data available. Appendix B discusses the shuttle vehicle inducer performance characteristics based on some preliminary and highly speculative data. The problems relating

to stresses and cavitation damage to the impeller and casing are considered to be very serious and require careful attention. The effect of cavitation damage on a conventional (short life) rocket inducer is minor since the operating time is only a matter of minutes. The shuttle, however, with the required reusable characteristic presents serious material problems in the turbomachinery system.

6.0 CONCLUSIONS

Based on the work reported, the following conclusions may be drawn:

1. Based on the Phase I tests the constant pressure cambered supercavitating cascade theory (18) tends to be overly optimistic in predicting the lift performance of high stagger angle cascades.
2. The theory for supercavitating cascades of cambered foils (28) appears to agree rather well with the test data provided that the flow is nearly two-dimensional and that supercavitating conditions exist.
3. The complex three dimensional flow field present in an actual inducer almost assures that empirical modifications to the design will be required. The design technique as developed (26,34) is admittedly less sophisticated than might be desired, however, it appears to be an adequate first step which should be built upon. A new rationale for determining head distribution among stages is needed.

4. The constant pressure cambered foil profile is considered inferior to the five-term cambered shape for cascade applications. The shift of the center of pressure further aft is advantageous.

5. Due to the various off-design operating conditions encountered, the theory formulated for partially cavitating cascades might prove especially valuable and should be further studied.

6. The swept leading edge configuration is apparently both hydrodynamically and structurally superior to the radial leading edge design.

7. The improved second stage design capability made possible primarily through the investigation of the radial vortex filament in a cylindrical annulus (42) should result in much improved second stage designs. In particular, the larger hub/diameter ratios such as in the designs discussed should improve performance. No model tests, however were conducted on second stage models after the improved design information was available.

8. In tandem, a two stage model demonstrated a flat N_{ss} vs. ψ curve with a larger percentage of the total head being assumed by the second stage as N_{ss} is increased. In addition, the tandem model (7.0 inch diameter) was affected only slightly by a change in overlap from -6.0 inches to -1.5 inches.

9. While not totally eliminating the unstable region, the tandem inducer configuration with a supercavitating first stage did produce a large "stable" operating range where the total fluctuating head was typically less than 5 percent of the total head generated.

10. The originally proposed stability criterion of (16) did not appear to correlate well with the observed onset of flow instabilities in the model.

11. The mechanism for flow instability in the models tested appeared to be related to cascade-cavity interference. The base cavity is predominant in this interference, the effect of the tip cavity being secondary. When the flow coefficient is below a critical value (dependent on the geometry of each inducer) and the suction specific speed is high enough that the cavity extends back to or slightly beyond the leading edge of the adjacent blade, limit cycle type cavity oscillations may occur. In this region it is believed that the cavity-length-head relationship for the impeller may be inherently unstable with the cavity length and head oscillating between fixed boundaries.

12. It is apparent that tandem inducers using a supercavitating first stages and subcavitating second stages may be designed to operate over a fairly wide range of suction specific speeds (models operated at 10,000 - 30,000 in water) and flow coefficients (models operated at .12 - .07) with pressure fluctuations of less than 10 percent of the head generated.

13. The influence of the remainder of the hydraulic system (including main fuel pump) on damping or amplifying the pressure fluctuation level cannot presently be predicted. In addition, the number of inducer models tested has been limited and these have been tested only in room temperature water. The thermodynamic effects of cavitation in cryogenic fluids will raise the range of operating suction specific speeds to higher values.

14. The type of inducer investigated might well be an alternative to the simple helical types presently used. This approach would appear to be even more attractive as future performance requirements become more severe with regard to higher speeds, lower flow coefficients, and higher total head generation requirements. It seems likely that more than two stages may be required for such applications.

15. Cavitation damage to the models and test section and previous research into cavitation damage and related phenomena indicates that serious materials problems may be expected for future high performance turbomachinery systems having long life requirements such as for the proposed space shuttle vehicle. These problems will be present regardless of the inducer configuration finally chosen.

ACKNOWLEDGMENTS

The author has summarized a long and many faceted research program. As is evident from the numerous references to the eight previously published technical reports on the project, several members of the HYDRONAUTICS, Incorporated staff are responsible for individual contributions to the work summarized herein. Particular credit is due Dr. D. N. Contractor, Mr. V. E. Johnson, Jr., Mr. C. C. Hsu, Dr. B. Yim, Mr. R. A. Barr, Mr. F. J. Turpin, and Dr. P. Van Dyke. Credit is also due Messrs. J. McBeth, R. Bateman and S. Dorr for their work on the experimental program.

HYDRONAUTICS, Incorporated

-84-

APPENDIX A
SATURN V INDUCER OPERATING CHARACTERISTICS

The following section presents an analysis of the operating characteristics of the Saturn V launch vehicle turbomachinery (primarily inducer) operating characteristics. The analysis is based on information received from NASA which consisted of the following:

- (a) A drawing (No. 459005) of the Rocketdyne J-2 fuel inducer.
- (b) A drawing (No. 456205) of the Rocketdyne J-2 oxidizer inducer.
- (c) A drawing (No. 459738 Rev. B) of the Rocketdyne F-1 oxidizer inducer.
- (d) A test data plot (No. AX-0244) of head generated vs. NPSH for various flow rates in LH₂ for the J-2 fuel pump assembly (not inducer alone). The range in this plot is NPSH: 0-320', HEAD: 26,000-38,000', DISCHARGE: 7220-8576 gpm., RPM: 25,600.
- (e) A test data plot (ENGINE No. S/N J-2083) of the head generated vs. NPSH for various flow rates in water for the J-2 oxidizer pump assembly (not inducer alone). The range for this plot is NPSH: 10-90', HEAD: 1200-1900', DISCHARGE: 2264-2851 gpm, RPM: 7892.

(f) Three test data plots (C-365, 366 & 367) of the head generated vs. NPSH for various flow rates in LOX for the F-1 oxidizer pump assembly (not inducer alone) also called the Mark 10 LOX Pump. The range for these plots is NPSH: 40-140', HEAD: 2600-3500', DISCHARGE: 25,000-29,750 gpm, RPM: 5700.

In addition, the available information regarding the NPSH range in flight is as follows:

NPSH - Ft.

Turbo Pump	S-IC Stage	S-II Stage	S-IVB Stage
J-2 Fuel		163-350'	350-550'
J-2 Oxidizer		44-55'	42.5-54'
F-1 Oxidizer	95-255'		

Using this available material, the following ranges of parameters during an actual flight have been calculated. The results presented in Tables A-1, A-2 and A-3 are, therefore, a mixture of flight information and test data results together with the geometry of the inducers as obtained from the drawings.

These numbers are believed to be a fair approximation of the inducer performance in the Saturn V application. However, a time history of the variation of discharge (flow coefficient)

and NPSH was not available to calculate the time history of suction specific speed during a typical flight. The performance curves available were not for the inducer alone, but rather for the inducer-main fuel pump combination.

The vapor pressure-temperature relationship for LH_2 is so critical that the temperature of the inlet fuel is apparently an overriding factor in determining NPSH at the inlet. For example, LH_2 becomes a solid at $25.2^\circ R$ where the vapor pressure is only about 36 ft. of LH_2 . At $30^\circ R$ the vapor pressure has risen to 115' LH_2 and at $35^\circ R$ to 295' LH_2 . Temperature control must, therefore, be very critical to the performance of the turbomachinery. The time history of the LH_2 temperature variation during a flight would be helpful in understanding the problem. In the case of LOX, the vapor pressure is less than 1 psi or 2 ft. of LOX as long as the temperature is kept below $125^\circ R$ and would therefore appear to be much less critical than LH_2 .

NASA indicated that the frequency range of importance for the F-1 engine was about 0-50 cps with particular emphasis on the 10-15 and 28-35 cps regions. While the requirement was stated that the inducer and main pump instabilities should be such that no more than 0.1% fluctuation in chamber pressure would be observed in the 0-50 cps range, no information is available on what this is likely to require in the ratio of inducer head instability to inducer developed head.

TABLE A-1

Rocketdyne J-2 Oxidizer InducerGeometry:

Inlet O.D.	6.75"
Outlet O.D.	6.75"
Inlet hub diameter	1.375"
Outlet hub diameter	2.750"
Inlet hub ratio	0.204
Outlet hub ratio	0.408
Axial extent	3.25"
Axial extent ratio	0.481
Number of blades (total)	3
Number of full blades	3
Number of partial blades	0
Inlet area	0.238 ft. ²
Outlet area	0.208 ft. ²
Inlet area before hub	0.249 ft. ²

General Engine Characteristics:

Engine thrust	230,000 lb.
Engine length	116 inches
Engine diameter	80.5 inches
Engine weight	3492 lb.
Fuel/oxidizer	LH ₂ /LOX
LH ₂ density	4.39 lb/ft. ³
LOX density	70.8 lb/ft. ³
Volume rate of LH ₂ cons.	.252-.299 cu ft./hr./lb.T
Weight rate of LH ₂ cons.	1.11-1.31 lb/hr/lb.T
Volume rate of LOX cons.	.079-.0995 cu.ft/hr./lb.T
Weight rate of LOX cons.	5.59-7.04 lb/hr./lb.T
Volume ratio of LH ₂ /LOX	3.00-3.19
Weight ratio of LH ₂ /LOX	.187-.199

Flow Conditions:Saturn V

Stage II or Stage III

RPM	8,800
NPSH range in flight	42-55'
Discharge range, gpm	2264-2851 gpm
Discharge range, cfs	5.05-6.35 cfs
Inlet axial velocity range	21.2-26.7 fps
Outlet axial velocity range	24.3-30.5 fps
Inlet tip speed	259 fps
Outlet tip speed	259 fps
Inlet flow coef. range	.819-.1030
Outlet flow coef. range	.0938-.1178
Inlet flow coef. range excluding .204 hub	.0784-.0985
N _{ss} range in flight using max. Q	23,400-28,500
N _{ss} range in flight using min. Q	20,900-25,400
Tip σ range using max. Q	.0303-.0417
Tip σ range using min. Q	.0333-.0457
Hub σ range using max. Q	.585-.738
Hub σ range using min. Q	.694-.951

TABLE A-2
Rocketdyne J-2 Fuel Inducer

<u>Geometry:</u>		<u>General Engine Characteristics:</u>	
Inlet O.D.	7.80"	Engine thrust	230,000 lb.
Outlet O.D.	7.20"	Engine length	116 inches
Inlet - hub diameter	2.93"	Engine diameter	80.5 inches
Outlet - hub diameter	6.01"	Engine weight	3492 lb.
Inlet - hub ratio	0.376	Fuel/oxidizer	LH ₂ /LOX
Outlet - hub ratio	0.835	LH ₂ density	4.39 lb/ft. ³
Axial extent	4.01"	LOX density	70.8 lb/ft. ³
Axial extent ratio	0.514	Volume rate of LH ₂ cons.	.252-.299 cu. ft./hr./lb.T
Number of blades (total)	8	Weight rate of LH ₂ cons.	1.11-1.31 lb/hr./lb.T
Number of full blades	4	Volume rate of LOX cons.	.079-.0995 cu.ft/hr./lb.T
Number of partial blades	4	Weight rate of LOX cons.	5.59-7.04 lb/hr./lb.T
Inlet area	0.285 ft. ²	Volume ratio of LH ₂ /LOX	3.00-3.19
Outlet area	0.0856 ft. ²	Weight ratio of LH ₂ /LOX	.187-.199
Inlet area before hub	0.332 ft. ²		

Flow Conditions:Saturn V

	<u>Stage II</u>	<u>Stage III</u>
RPM	25,600	
NPSH range in flight	163'-350'	350-550'
Discharge range, gpm	7220-8576 gpm	
Discharge range, cfs.	16.1-19.1 cfs	
Inlet axial velocity range	56.5-67.0 fps	
Outlet axial velocity range	188.-223. fps	
Inlet tip speed	870 fps	
Outlet tip speed	804 fps	
Inlet flow coef. range	.065-.077	
Outlet flow coef. range	.234-.278	
Inlet flow coef. range excluding .376 hub	.056-.066	
N _{ss} range in flight using max. Q	29,300-51,700 26,900-47,500	20,800-29,300
Tip σ range using max. Q	.00080-.00240	.00240-.00411
Tip σ range using min. Q	.00097-.00257	.00257-.00428
Hub σ range using max. Q	.0530-.1620	.1620-.2780
Hub σ range using min. Q	.0661-.1735	.1754-.2921

TABLE A-3
Rocketdyne F-1 Oxidizer Inducer

Geometry:

Inlet O.D.	15.75"
Outlet O.D.	15.75"
Inlet hub diameter	3.51"
Outlet hub diameter	6.39"
Inlet hub ratio	.223
Outlet hub ratio	.405
Axial extent	6.70"
Axial extent ratio	.425
Number of blades	3
Number of full blades	3
Number of partial blades	0
Inlet area	1.28 ft. ²
Outlet area	1.13 ft. ²
Inlet area before hub	1.35 ft. ²

General Engine Characteristics:

Engine thrust	1,522,000 lb.
Engine length	216 inches
Engine diameter	144 inches
Engine weight	18,800 lb.
Fuel/oxidizer	LOX/hydrocarbon
Volume rate of LOX cons.	.132-.158 cu.ft./hr/lb.
Weight rate of LOX cons.	9.35-11.2 lb./hr/lb.T

Flow Conditions:Saturn V Stage II

RPM	5700
NPSH range in flight	95'-255'
Discharge range, gpm	25,000-30,000 gpm
Discharge range, cfs	55.7-66.9 cfs
Inlet axial velocity range	43.5-52.2 fps
Outlet axial velocity range	49.4-59.1 fps
Inlet tip speed	391 fps
Outlet tip speed	391 fps
Inlet flow coef. range	.110-.134
Outlet flow coef. range	.126-.151
Inlet flow coef. range excluding .223 hub	.105-.127
N _{ss} range in flight using max. Q	15,480-32,400
N _{ss} range in flight using min. Q	14,100-29,500
Tip σ range using max. Q	.0219-.0883
Tip σ range using min. Q	.0272-.0934
Hub σ range using max. Q	.298-1.205
Hub σ range using min. Q	.446-1.530

HYDRONAUTICS, Incorporated

-91-

APPENDIX B

SHUTTLE VEHICLE INDUCER OPERATING CHARACTERISTICS

The following section details some calculations regarding the proposed space shuttle vehicle turbomachinery characteristics. NASA has indicated that the fuel and oxidizer systems will likely contain two separate inducers followed by the main centrifugal pumps. The inducers are referred to as the low speed inducer (LSI) and high speed inducer (HSI). The numbers presented are based on some preliminary information. They are therefore quite speculative and not intended to necessarily reflect the final shuttle design characteristics.

I. LOX System

(a) Low Speed Inducer (LSI)

NPSH = 16 ft. LOX

Q = 4000-6000 gpm.

RPM = 4000

Dia. = 14"

Outlet head = 200-300 psi = 410-610 ft. LOX

Based on these values:

N_{ss} range = 31,600 to 38,700

ϕ_o range = .0352 to .0512

ψ range = 0.214 to 0.322

U_{tip} = 244 fps

σ_{tip} range = .0146 to .0161

(b) High Speed Inducer (HSI) and Main LOX Pump

NPSH range = 410-610 ft. LOX

Q = 4000-6000 gpm.

RPM = 40,000

Dia. = 14"

Outlet head = 6,000-7,000 psi = 12,200-
14,200 ft. LOX

Based on these values:

N_{ss} range = 25,000 to 34,200 (max. Q)
or 20,400 to 28,000 (min. Q)

ϕ_o range = .00342 to .00512

U_{tip} = 2,440 fps

σ_{tip} = .0044 to .0066

II. LH₂ System

(a) Low Speed Inducer

NPSH = 30 ft. LH₂

Q = 10,000-15,000 gpm

RPM = 4,000

Dia. = 20"

Outlet head = 900 to 1,200 ft. LH₂

Based on these values:

N_{ss} range = 31,250 to 38,200

ϕ_o range = .0292 to .0438

-94-

$$\psi \text{ range} = .326 \text{ to } .428$$

$$U_{\text{tip}} = 348 \text{ fps}$$

$$\sigma_{\text{tip}} = .0140 \text{ to } .0151$$

(b) High Speed Inducer (HSI) and Main LH₂ Pump

$$\text{MPSH range} = 900 - 1,200' \text{ LH}_2$$

$$Q = 10,000-15,000 \text{ gpm}$$

$$\text{RPM} = 40,000$$

$$\text{Dia.} = 14''$$

$$\text{Outlet head} = 6,000-7,000 \text{ psi} = 197,000 \text{ to } 230,000 \text{ ft. LH}_2$$

Based on these values:

$$N_{\text{ss}} \text{ range} = 24,00 \text{ to } 29,650 \text{ (max. } Q)$$

$$19,600 \text{ to } 24,200 \text{ (min. } Q)$$

$$\phi_o \text{ range} = .00858 \text{ to } .0128$$

$$U_{\text{tip}} = 2440 \text{ fps}$$

$$\sigma_{\text{tip}} = .0096 \text{ to } .0129$$

Based on the summary presented, the low speed inducer for the LOX system is relatively conventional. The N_{ss} values are reasonable with the flow coefficient range considerably lower than most inducers. The low speed inducer for the LH₂ system is similar to the LOX L.S.I. with a lower than usual flow coefficient range.

The high speed inducers for both the LOX and LH₂ systems have reasonable N_{ss} values in the range of 19,000 to 34,000, but have extremely low flow coefficients (.004 to .013) and high tip speeds (2440 fps).

The low flow coefficients present the problem of extremely high stagger angle requirements for the appropriate cascades. For $\phi_o = .007$, for example, the stagger angle β_1 is $89^{\circ}36'$. As $\beta_1 \rightarrow 90^{\circ}$ (i.e. $\phi_o \rightarrow 0$), the normal to the blade leading edges approaches a 90° angle to the incoming flow. At small angles of attack, therefore, it is apparent that the solidity of such a cascade cannot exceed 1.0 or the trailing edge of one blade will overlap the leading edge of the next.

It would seem that inducers with such low flow coefficients, therefore, must be limited to rather low solidities on the order of 0.50 to avoid severe interference. The conventional helical inducer has a typical solidity much higher than this. For example, the F-1 oxidizer inducer has solidity values of 2.03, 2.60, and 4.16 at the tip, mid, and hub radii. The J-2 oxidizer inducer has corresponding solidities of 1.82, 2.41, and 3.86. Since the total head generation, however, must be high, this means that the overall value of the parameter $C_L \frac{c}{d}$ must be high. C_L however must be kept relatively low to preserve stability under the required high N_{ss} condition. These factors combine to make the use of tandem inducer rows likely.

To partially alleviate the problem of low inlet flow coefficient, a large hub ratio may be used. As an example, using a 0.90 hub ratio, the effective inlet flow coefficient after the hub will be increased from .007 to .037. This reduces the required cascade stagger angle from $89^{\circ}36'$ to $87^{\circ}53'$. While this is still a large stagger angle it represents a significant improvement when referred to the limit of 90° .

When all of the above factors are considered, the inducer has a large hub ratio with low solidity (compared to conventional inducers) and several tandem rows. The first rows will undoubtedly be supercavitating with less and less cavitation as the head rises progressively through the inducer stages. The resulting inducer looks very much like a compressor with supercavitating blade sections. For such a device, supercavitating and partially cavitating cascade characteristics such as have been investigated in the present study are required.

As discussed in section 4.1, Figure 23 presents those combinations of prototype LOX and LH₂ inducers having combinations of rotational speed and diameter which are structurally compatible with the five term cambered two bladed model designed for Phase III tests. For reference, the present Saturn V inducers were included in this figure. In addition, three points were also included for "conjectured" shuttle vehicle inducers. These are for the inducers of the present Appendix which have just been discussed.

It is apparent from Figure 23, that the conjectured shuttle LOX and LH₂ low speed inducers are quite compatible with the model when a 50,000 psi prototype stress is assumed. This is also true for the J-2 and F-1 inducers presented. The high tip speed of the conjectured LOX and LH₂ high speed inducers for the shuttle, however, result in scaled stresses far in excess of the limits for the present models. In order for structural compatibility to exist, the prototype allowable design stresses would have to be increased to 230,000 psi for the LH₂ H.S.I. and 415,000 psi for the LOX H.S.I. Severe structural problems are thus indicated at these high tip speeds.

The problem of cavitation damage to the blades and casing becomes very serious when the proposed 30-100 mission requirements for the shuttle components is considered. Damage suffered during model tests is discussed in section 4.3.6 and illustrated in Figures 55, 56, and 57.

Present indications are that cavitation damage scales roughly as the 6th power of the absolute fluid velocities. The high speed inducers being considered have tip speeds on the order of 2440 fps. The present Saturn V inducers have tip speeds which vary from 870 fps for the J-2 fuel inducer to 391 fps for the F-1 oxidizer inducer and 259 fps for the J-2 oxidizer inducer. Thus the new tip speeds are from 2.8 to 9.4 times the present values. This could thus result in damage rates of 150 to 70,000 times as great. Little basic

cavitation damage research has been conducted in cryogenic fluids, however, and the effect of temperature is known to be a significant factor influencing damage rate as is ambient static pressure, fluid and material properties. Some research into this field will almost certainly be required to provide guidance in the design of inducers such as the ones presently under discussion.

REFERENCES

1. Daily, J. W., "Theory of Turbomachinery," Chapter 8 in Engineering Hydraulics, H. Rouse, Ed., Wiley, 1961.
2. Ross, C. C and Banerian, G., "Some Aspects of High Suction Specific Speed Pump Inducers," Transactions ASME, Vol. 78, Number 8, 1956.
3. Pinkel, I. I., et al., "Conference on Selected Technology for the Petroleum Industry," NASA SP-5053, Chapter 6, Pump Technology, December 1965.
4. Acosta, A. J., "An Experimental Study of Cavitating Inducers," Trans. 2nd Symp. on Naval Hydrodynamics, ONR Publication ACR-38, 1958.
5. Hartmann, M. J., and Soltis, R. F., "Observations of Cavitation in a Low Hub-Tip Ratio Axial Flow Pump," ASME Paper No. 60-Hyd-14, March 1960.
6. Iura, T., Discussion of Ref. 4 by Acosta, Trans. 2nd Symp. on Naval Hydrodynamics, ONR Pub. ACR-38, 1958.
7. Soltis, R. F., "Some Visual Observations of Cavitation in Rotating Machinery," NASA TN D-2681, July 1965.
8. Crouse, James E. and Sandercock, Donald M., "Blade-Element Performance of Two Stage Axial Flow Pump with Tandem Row Inlet Stage," NASA TN D-3962, May 1967.
9. Sandercock, D. M., and Crouse, J. E., "Design and Overall Performance of a Two-Stage Axial-Flow Pump with a Tandem-Row Inlet Stage," NASA TN D-2879, March 1965.
10. Soltis, R. F., Urasek, D. C., and Miller, M. J., "Blade-Element Performance of a Tandem-Bladed Inducer Tested in Water," NASA TN D-5562, November 1969.

11. Soltis, R. F., Ursek, D. C., and Miller, M. J., "Overall Performance of a Tandem-Bladed Inducer Tested in Water," NASA TN D-5134, May 1969.
12. Eisenberg, P. and Tulin, M. P., "Cavitation", Chap. 12 in Handbook of Fluid Dynamics, V. L. Streeter, Ed. McGraw-Hill, 1961.
13. Stripling, L. B., and Acosta, A. J., "Cavitation in Turbo-Pumps, Part I," ASME Hydraulics Division Paper No. 61-WA-112, November 1961.
14. Acosta, A. J., and Hollander, A., "Remarks on Cavitation in Turbomachines," CIT Report 79.3, October 1959.
15. Wade, R. B., and Acosta, A. J., "Investigation of Supercavitating Cascades," ASME Journ. Basic Engr. Paper 66-WA/FE-25, December 1967.
16. Yeh, H., "An Actuator Disc Analysis of Inlet Distortion and Rotating Stall in Axial-Flow Turbomachines," Journal of the Aeronautical Sciences, Vol. 26, No. 11, 1959.
17. Auslaender, J., "The Linearized Theory for Supercavitating Hydrofoils Operating at High Speeds Near a Free Surface," HYDRONAUTICS, Incorporated Technical Report 001-5, June 1961.
18. Yim, B., "Supercavitating Cascades with Constant Pressure Cambered Blades," HYDRONAUTICS, Incorporated Technical Report 703-2, July 1967 (NASA CR-90426).
19. Yim, B., "The Higher Order Theory of Supercavitating Cascades with Constant Pressure Cambered Blades," HYDRONAUTICS, Incorporated Technical Report 703-3, October 1967. (NASA CR-91444).
20. Emery, James C., Herrig, L. Joseph, Erwin, John R., and Felix, A. Richard, "Systematic Two-Dimensional Cascade Tests of NACA 65 - Series Compressor Blades at Low Speeds," NACA Report 1368, 1958.

21. Numachi, F., "Cavitation Tests on Hydrofoils Designed for Accelerating Flow Cascades/Report 1," Report No. 125 of the Institute of High Speed Mechanics of Japan, April 1959.
22. Numachi, F., "Cavitation Tests on Hydrofoils Designed for Accelerating Flow Cascades: 3-Five Profiles Generated from Prescribed Pressure Configurations of Types 1 and 3," ASME Paper No. 63-WA-74, November 1963.
23. Barr, Roderick A., "Study of Instabilities in High Head Tandem Row Inducer Pumps," HYDRONAUTICS, Incorporated Interim Technical Report 703-1, February 1967.
24. Bowerman, R. D., "The Design of Axial-Flow Pumps," Trans. ASME, Vol. 78, No. 8, 1956.
25. Tyson, H. N., Jr., "Three-Dimensional Interference Effects of a Finite Number of Blades in an Axial Turbomachine," C.I.T. Report E19.1, November 1952.
26. Etter, R. J., and Hsu, C. C., "An Investigation of Tandem-Row High-Head Pump Inducers - Interim Report Phase II," HYDRONAUTICS, Incorporated Technical Report 703-8, February 1970.
27. Johnson, V. E., Jr., "Theoretical and Experimental Investigation of Supercavitating Hydrofoils Operating Near the Free Water Surface," NASA Technical Report R-93, 1961.
28. Hsu, C. C., "On the Flow Past a Supercavitating Cascade of Cambered Blades," HYDRONAUTICS, Incorporated Technical Report 703-5, February 1969. (NASA CR-100773).
29. Tulin, M. P., "Steady Two-Dimensional Cavity Flow about Slender Bodies," David Taylor Model Basin Report 834, May 1953.
30. Cohen, H. and Sutherland, C. D., "Finite Cavity Cascade Flow," Rensselaer Polytechnic Institute, Department of Mathematics, Report No. 14, April 1958.

31. Acosta, A. J., "Cavitating Flow Past a Cascade of Circular Arc Hydrofoils," California Inst. of Tech., Report No. E-79-2, March 1960.
32. Betz, A., and Petersohn, E., "Application of the Theory of Free Jets," NACA TN 667, April 1932.
33. Hsu, C. C., "Supercavitating Lifting Hydrofoils--Second Order Theory," HYDRONAUTICS, Incorporated Technical Report 121-6, March 1966.
34. Contractor, D. N., and Etter, R. J., "An Investigation of Tandem Row High Head Pump Inducers, Interim Report-Phase I," HYDRONAUTICS, Incorporated Technical Report 703-4, May 1969.
35. Pearsall, J. S., "The Use of Potential Flow Methods in Designing Cavitating Pumps," in 1968 ASME Cavitation Forum, ASME Fluids Engineering Conf., May 6, 7, 1968, Philadelphia, Pennsylvania.
36. Hsu, C. C., "On Flow Past a Cascade of Partially Cavitating Cambered Blades," HYDRONAUTICS, Incorporated Technical Report 703-6, March 1969.
37. Wade, R. B., "Flow Past a Partially Cavitating Cascade of Flat Plate Hydrofoils, California Institute of Technology Engineering Report No. 79-4, 1963.
38. United Aircraft Research Laboratories Report G910254-50 "Systematic Two Dimensional Cascade Tests of Double Circular-Arc Hydrofoils," 1968.
39. Lewis, George W., et al., "Cavitation Performance of an 83° Helical Inducer Operated in Liquid Hydrogen," NASA TM X-419, March 1961.
40. Soltis, Richard F., et al., "Investigation of the Performance of a 78° Flat Plate Helical Inducer," NASA TN D-1170, March 1962.

41. Montgomery, J. C., "Analytical Performance Characteristics and Outlet Flow Conditions of Constant and Variable Lead Helical Inducers for Cryogenic Pumps," NASA TN D-583, March 1961.
42. Etter, R. J. and Van Dyke, P., "Three Dimensional Flow Field from a Radial Vortex Filament in a Cylindrical Annulus," HYDRONAUTICS, Incorporated Technical Report 703-7, December 1969. (NASA CR-102560).
43. McMahon, J., "On the Roots of the Bessel and Certain Related Functions," Annals of Math. Vol. 9, No. 1, pp 29, 1894.
44. Titanium Metals Corp. of America, "Titanium Engineering Bulletin No. 1 - Properties of Ti-6Al-4V," New York, February 1965.
45. Scott, Russell, B., Cryogenic Engineering, D. Von Nostrand Company, Princeton, N. J., 1959.
46. Lieblein, S., Schwenk, F. C., and Broderick, R. L., "Diffusion Factor for Estimating Losses and Limiting Blade Loadings in Axial-Flow-Compressor Blade Elements," NACA RM E53D01, June 1953.
47. Tulin, Marshall P., "Supercavitating Propellers - History, Operating Characteristics, Mechanism of Operation," 4th Symposium on Naval Hydrodynamics, ONR Publication ACR-92, 1962.
48. "Aerodynamic Design of Axial-Flow Compressors," Volumes I, II and III, NACA RME56B03, August 1956.
49. Acosta, A. J., and Wade R. B., "Experimental Studies of Cavitating Hydrofoils in Cascade," CIT Report, February 1968.
50. Wood, G. M., "Visual Cavitation Studies of Mixed Flow Pump Impellers," ASME Paper No. 62-Hyd-12, 1962.

51. Wislicenus, F. G., "Fluid Mechanics of Turbomachinery," Volumes I and II, Dover Publications, New York, 1965.
52. Stepanoff, A. J., "Centrifugal and Axial Flow Pumps," 2nd Ed. John Wiley and Sons, N. Y., 1967.
53. Ralèigh, Lord "On the Pressure Developed in a Liquid During the Collapse of a Spherical Cavity, Philosophical Mag., Vol. 34, 1917.
54. Thiruvengadam, A. and Preiser, H. S., "On Testing Materials for Cavitation Damage," HYDRONAUTICS, Incorporated Technical Report 233-3, December, 1963.
55. Thiruvengadam, A. and Waring, S., "Mechanical Properties of Metals and Their Resistance for Cavitation Damage," HYDRONAUTICS, Incorporated Technical Report 233-5, June 1964.
56. Eisenberg, P., Preiser, H. and Thiruvengadam, A., "On the Mechanisms of Cavitation Damage and Methods of Protection," SNAME Transactions Vol 73, 1965.
57. Thiruvengadam, A., "The Concept of Erosion Strength," HYDRONAUTICS, Incorporated Technical Report 233-9, December 1965.
58. Thiruvengadam, A., "On Modelling Cavitation Damage," HYDRONAUTICS, Incorporated Technical Report 233-10, August 1966.
59. Thiruvengadam, A., "Theory of Erosion," HYDRONAUTICS, Incorporated Technical Report 233-11, March 1967.
60. Eisenberg, P., "Cavitation and Impact Erosion Concepts, Correlations, Controversies," Symposium on Characterization and Determination of Erosion Resistance, ASTM Annual Meeting, 1969, Atlantic City, N. J.

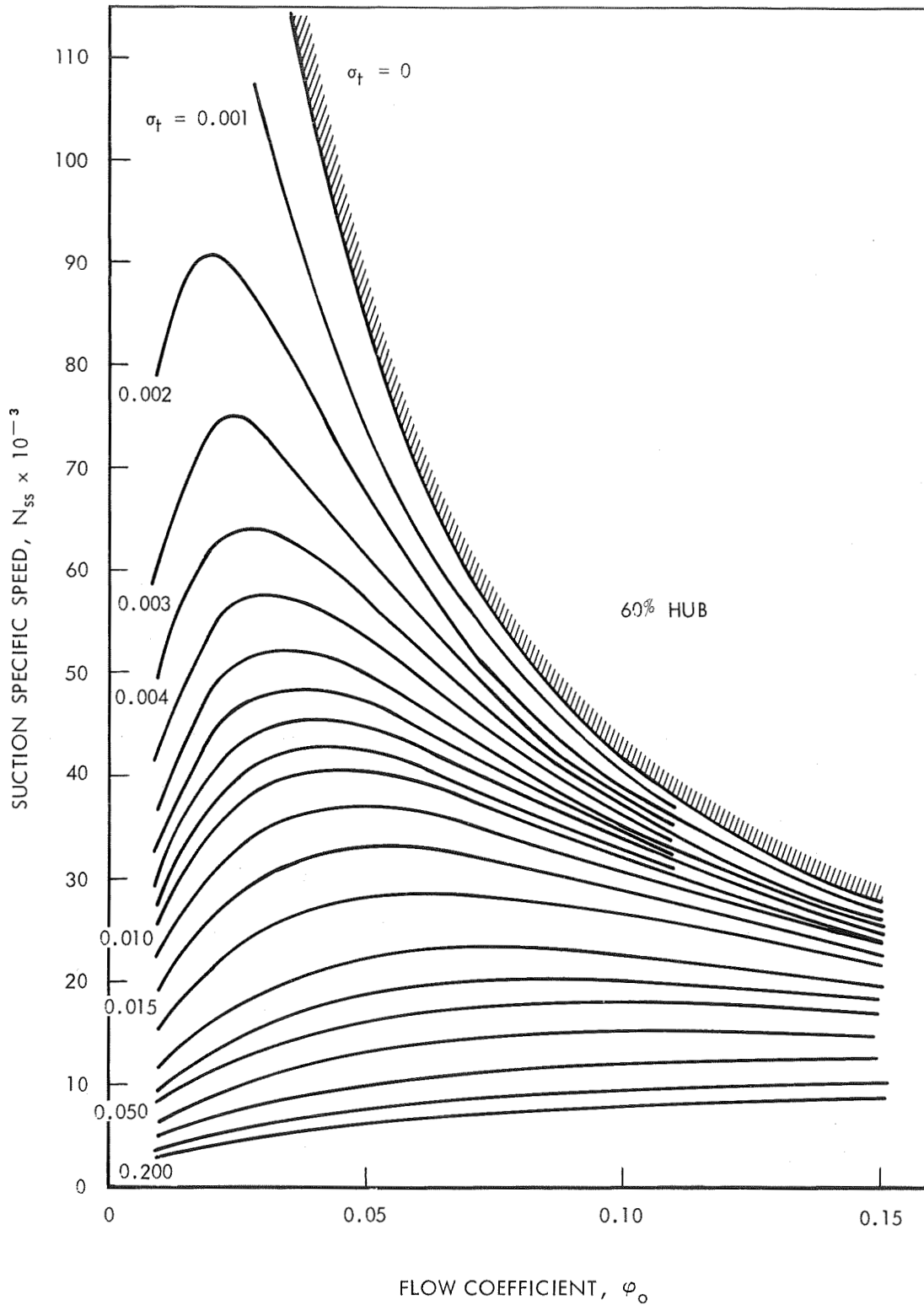


FIGURE 1 - INFLUENCE OF FLOW COEFFICIENT ON RELATIONSHIP BETWEEN SUCTION SPECIFIC SPEED AND TIP CAVITATION NUMBER FOR A 0.60 HUB / DIAMETER RATIO

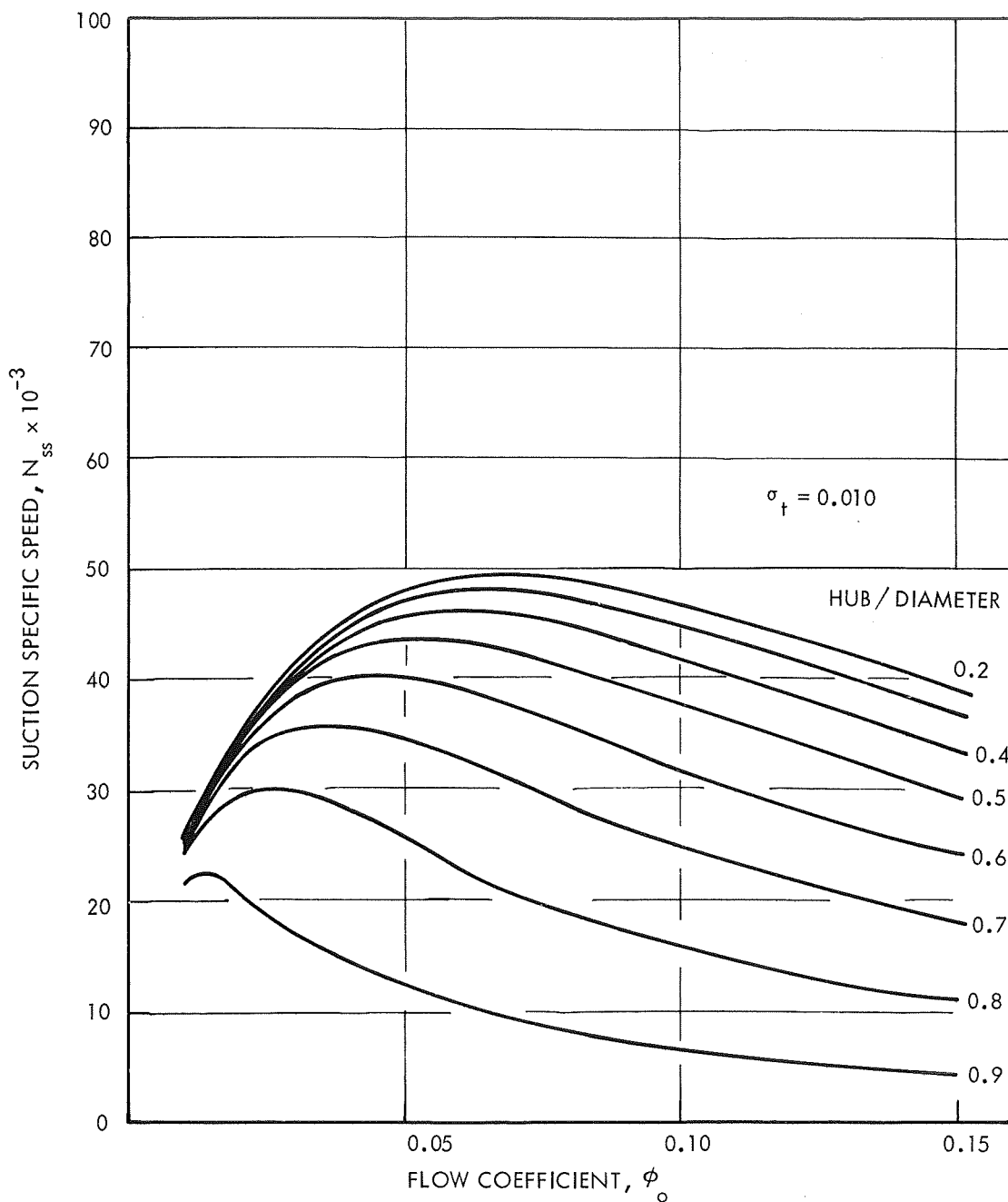


FIGURE 2 - INFLUENCE OF HUB / DIAMETER RATIO AND FLOW COEFFICIENT ON SUCTION SPECIFIC SPEED AT $\sigma_t = 0.010$.

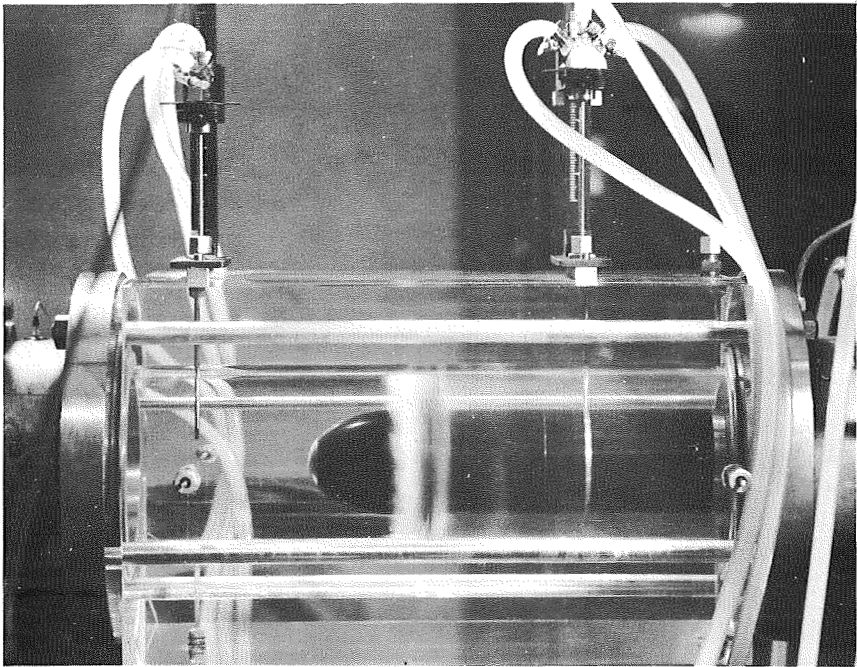


FIGURE 3 - TEST SECTION OF HYDRONAUTICS, INCORPORATED PUMP LOOP

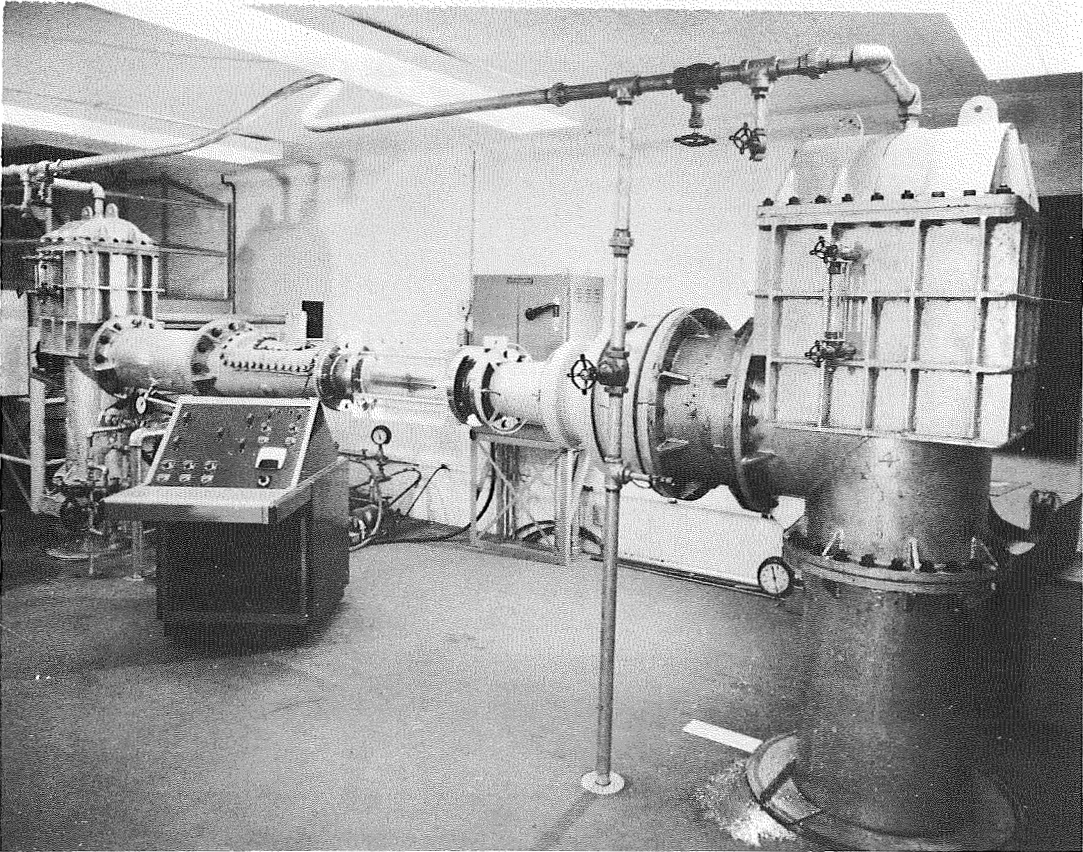


FIGURE 4 - OVERALL VIEW OF HYDRONAUTICS, INCORPORATED PUMP LOOP

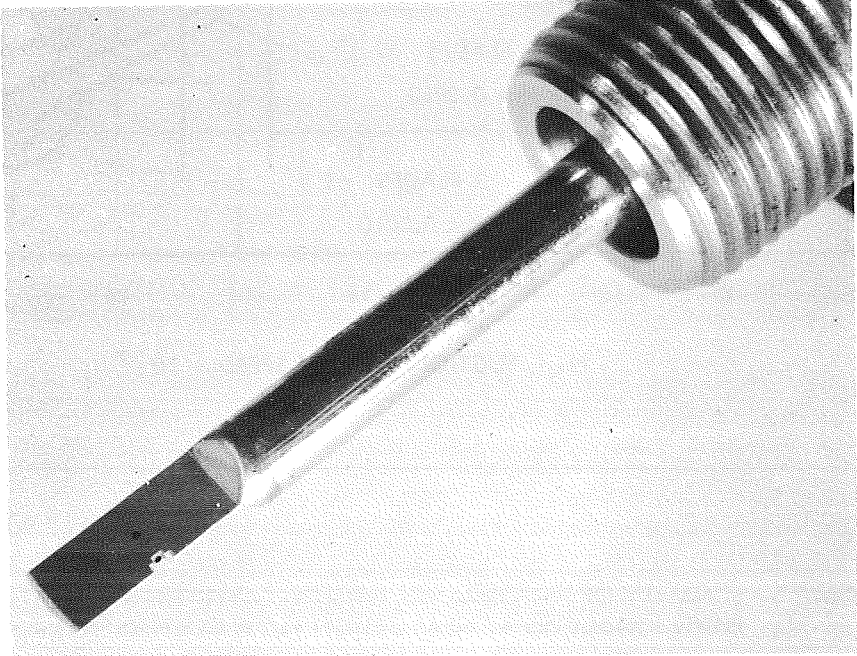
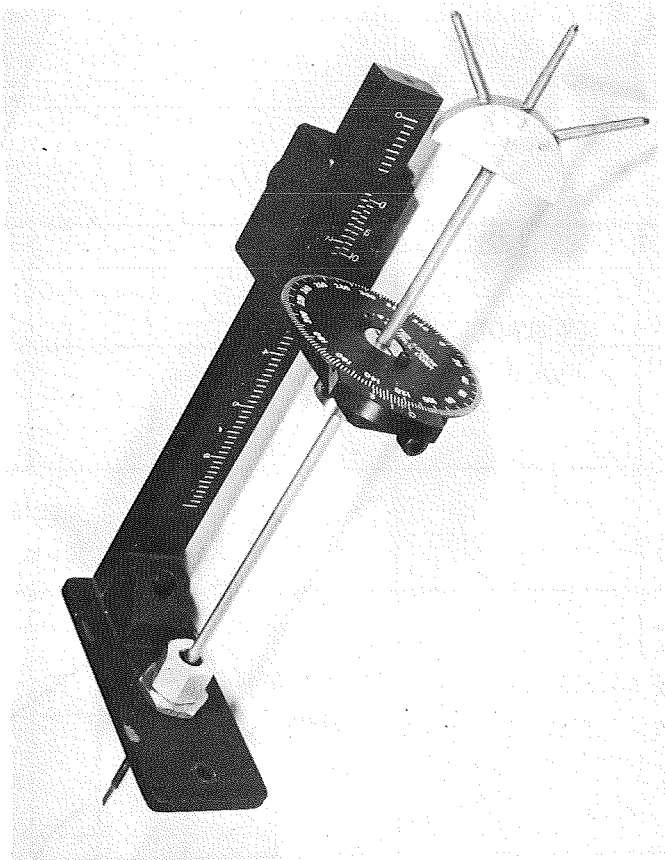


FIGURE 5 - YAW HEAD PROBE AND TRAVERSE STAND.

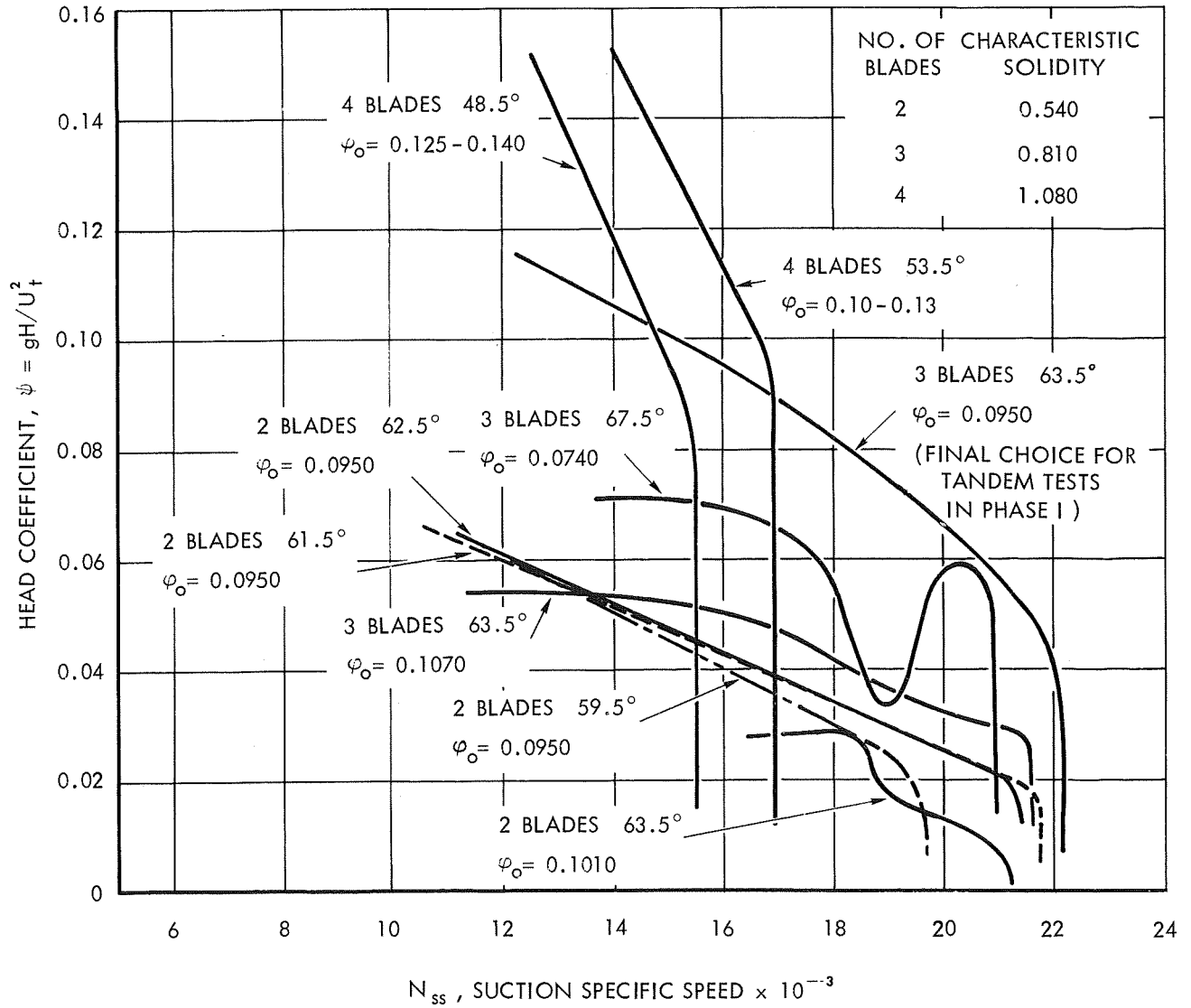


FIGURE 6 - SUMMARY OF PERFORMANCE OF SUPERCAVITATING FIRST STAGES FOR PHASE I INDUCERS AT NEAR DESIGN FLOW COEFFICIENT, $\phi_o = 0.10$



FIGURE 7 - TANDEM INDUCER MODEL WITH -6" OVERLAP AND 0° OFFSET. FIRST STAGE - 3 BLADES AT 63.5° PITCH, SECOND STAGE - 6 BLADES AT 55.8° PITCH.

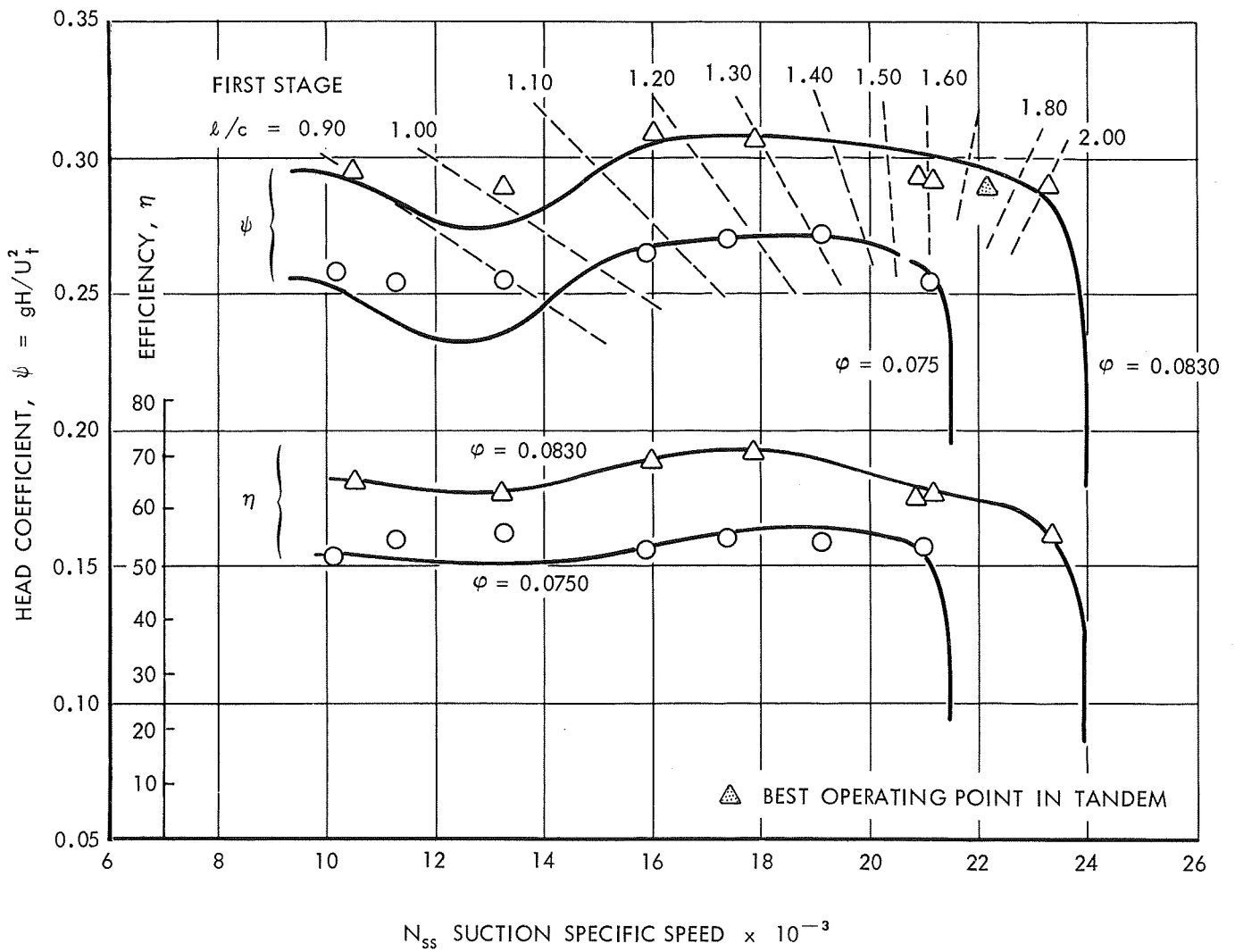


FIGURE 8 - TANDEM INDUCER PERFORMANCE WITH —6" OVERLAP, STAGE 1 - THREE BLADES 63.5° PITCH; STAGE 2 - 6 BLADES, 55.8° PITCH

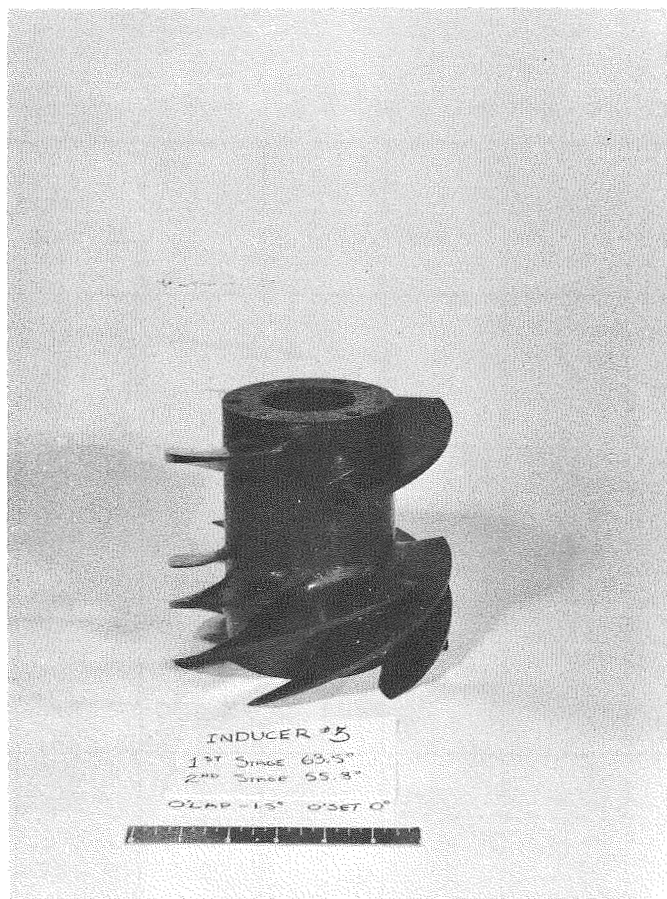


FIGURE 9 - TANDEM INDUCER MODEL WITH - 1.5 INCH OVERLAP AND 0° OFFSET. FIRST STAGE - 3 BLADES AT 63.5° PITCH, SECOND STAGE - 6 BLADES AT 55.8° PITCH.

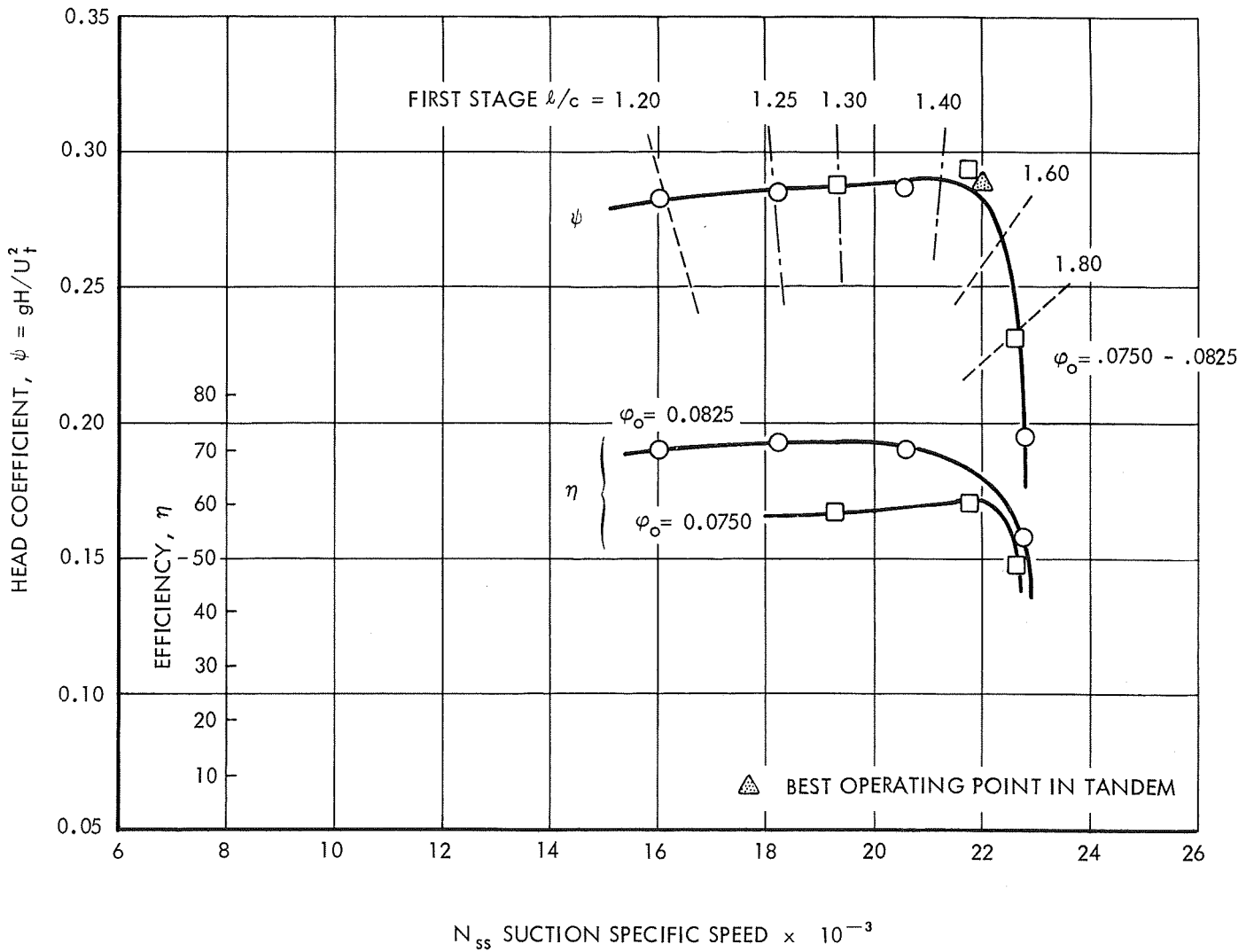


FIGURE 10 - TANDEM INDUCER PERFORMANCE WITH -1.5" OVERLAP
 STAGE 1 - THREE BLADES, 63.5° PITCH; STAGE 2 - SIX BLADES, 55.8° PITCH

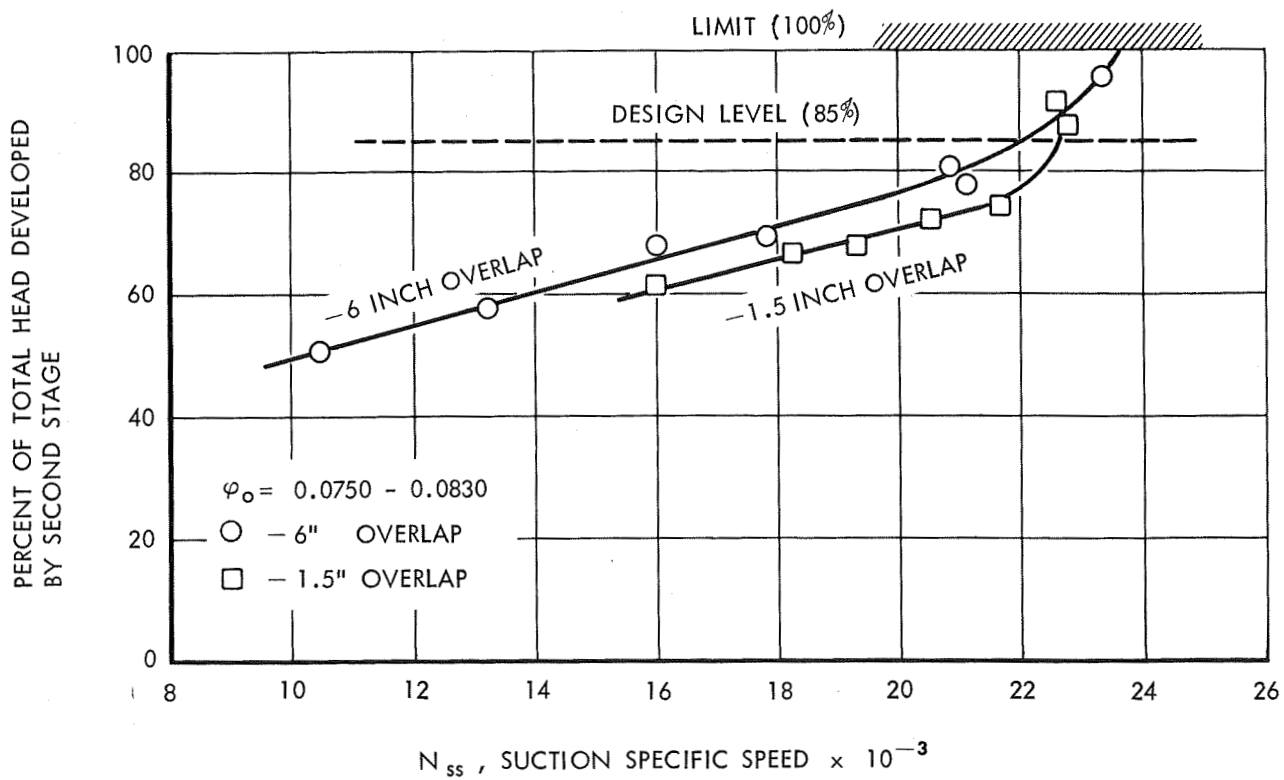


FIGURE 11 - DISTRIBUTION OF TOTAL HEAD RISE BETWEEN STAGE 1 AND STAGE 2 DURING TANDEM TESTS OF PHASE I

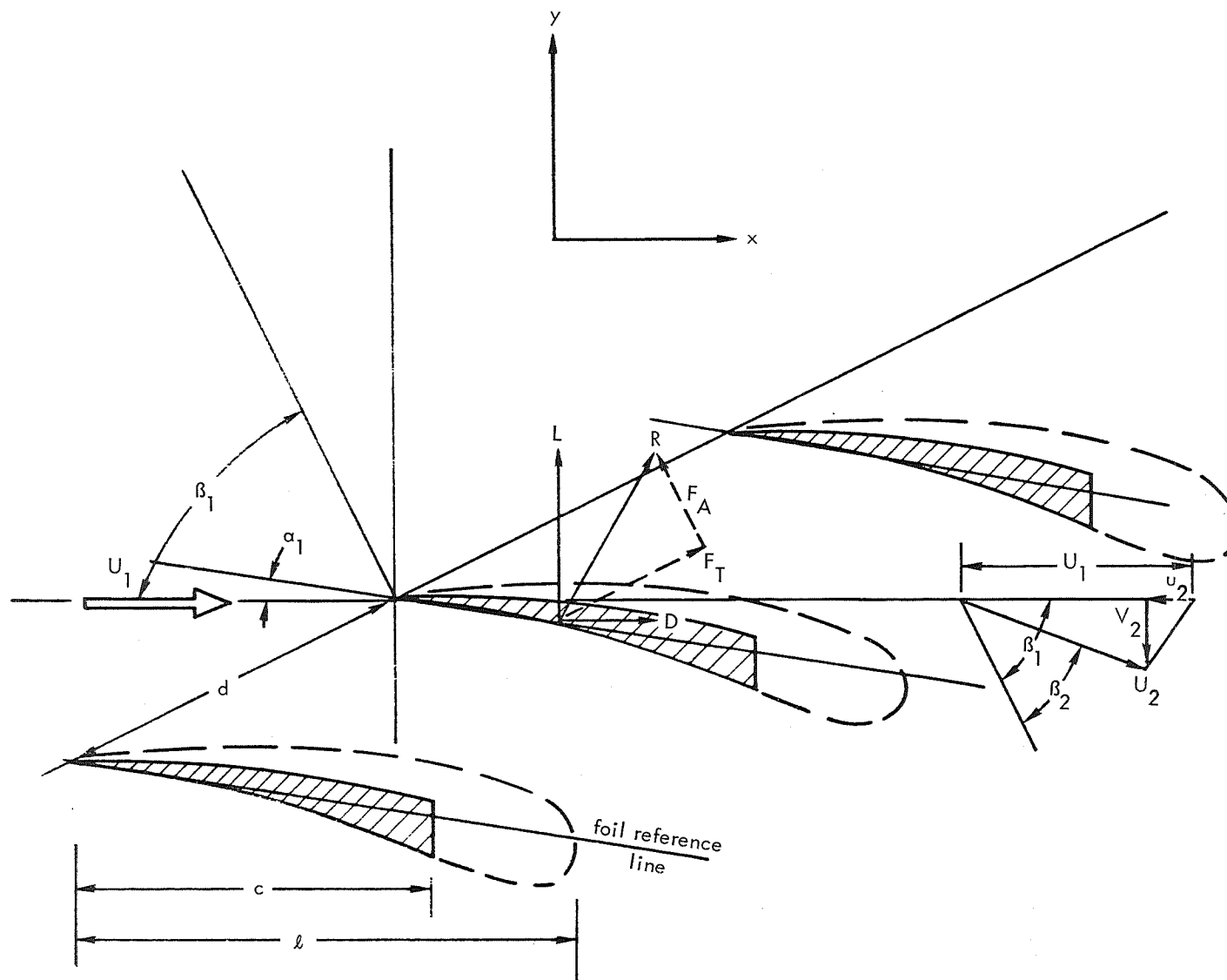
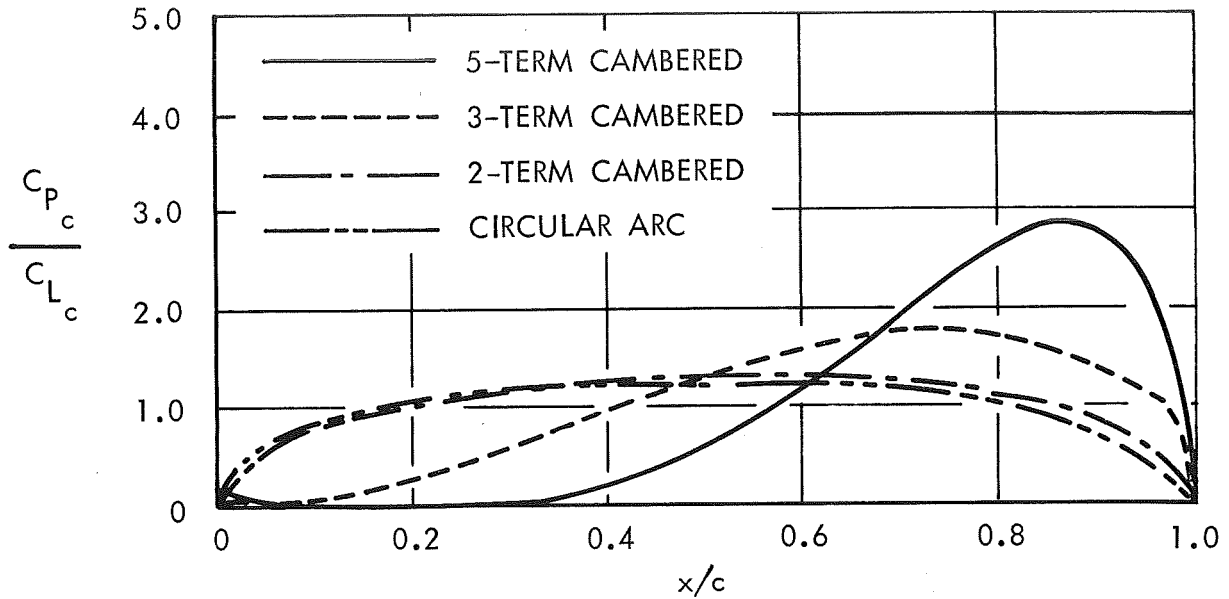
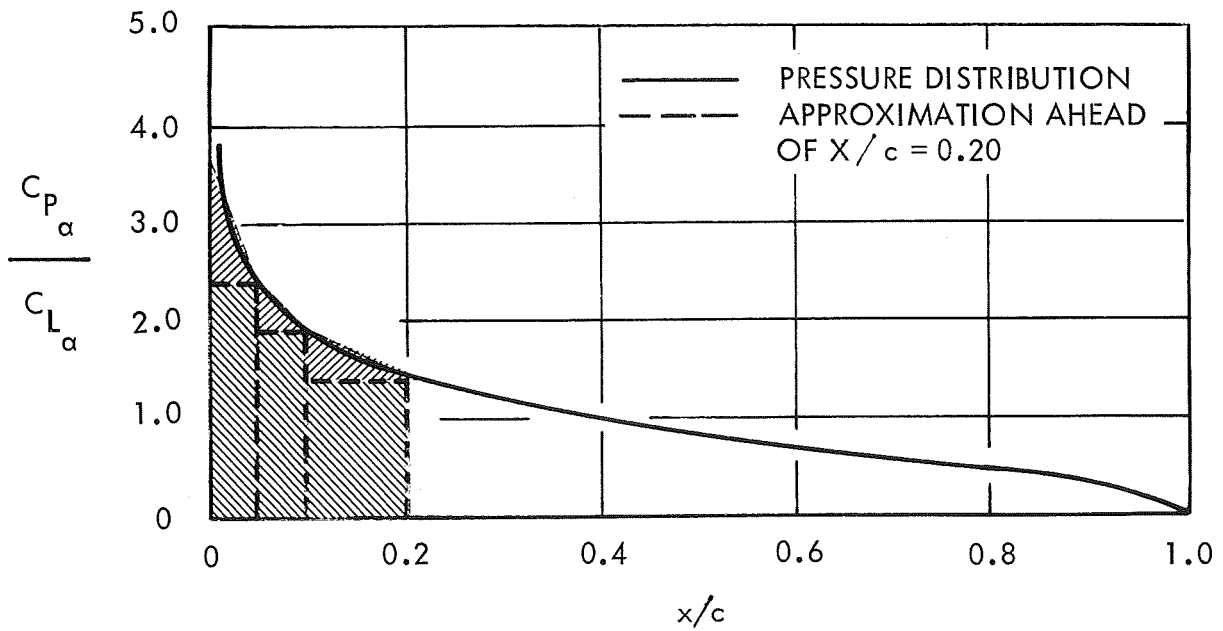


FIGURE 12 - DEFINITION SKETCH FOR A TWO DIMENSIONAL SUPERCAVITATING CASCADE



(a) CONTRIBUTION DUE TO CAMBER



(b) CONTRIBUTION DUE TO ANGLE OF ATTACK

FIGURE 13 - PRESSURE DISTRIBUTION ON FOUR TYPES OF ISOLATED FOIL PROFILES (AFTER REF (27))

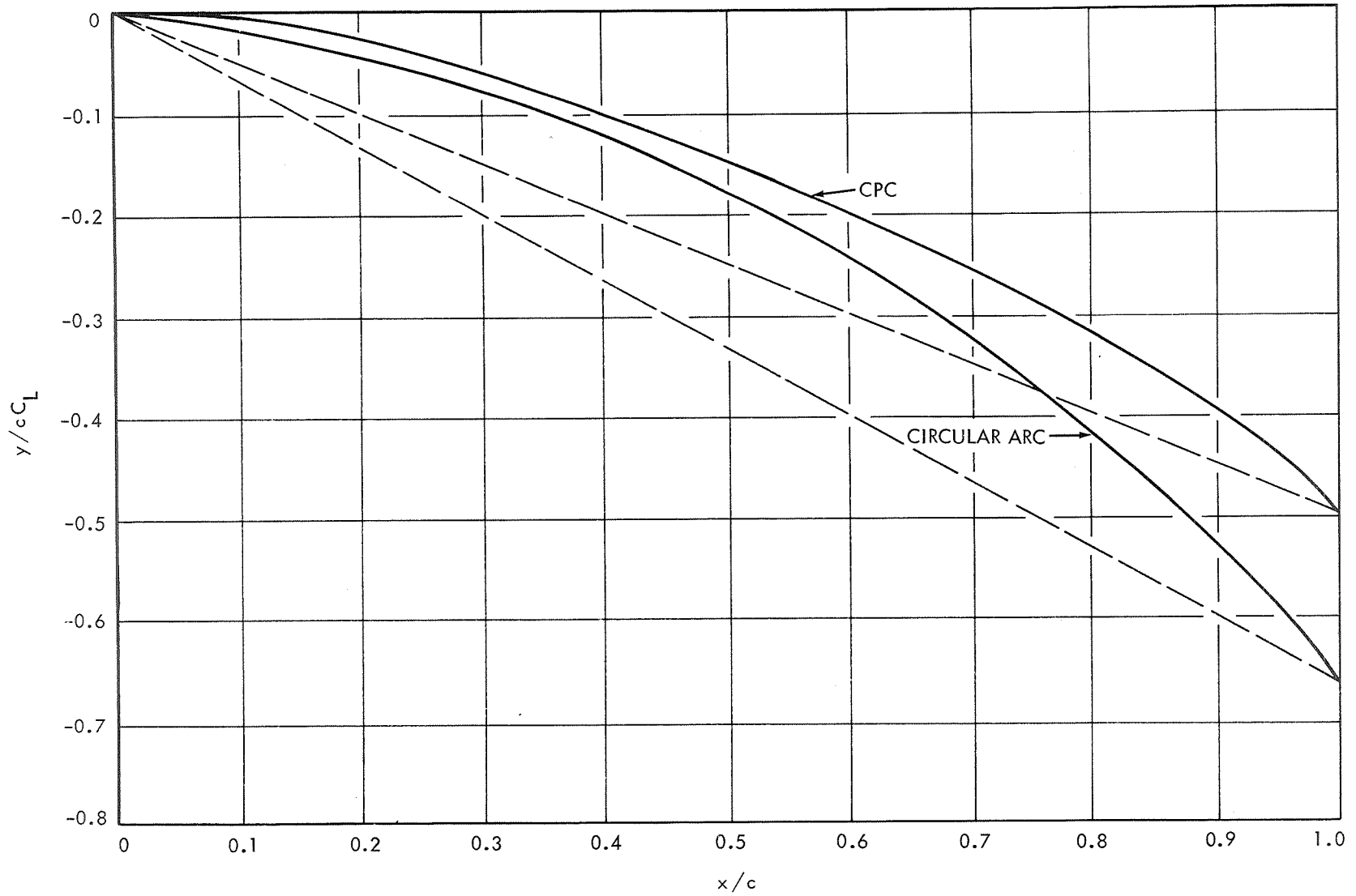


FIGURE 14 - COMPARISON OF FOIL SHAPES FOR CIRCULAR ARC AND CONSTANT PRESSURE CAMBER (AFTER YIM (18)) FOILS IN CASCADE WITH $\beta = 75^\circ$, $c/d = 0.410$, $\sigma / C_L = 0.082$

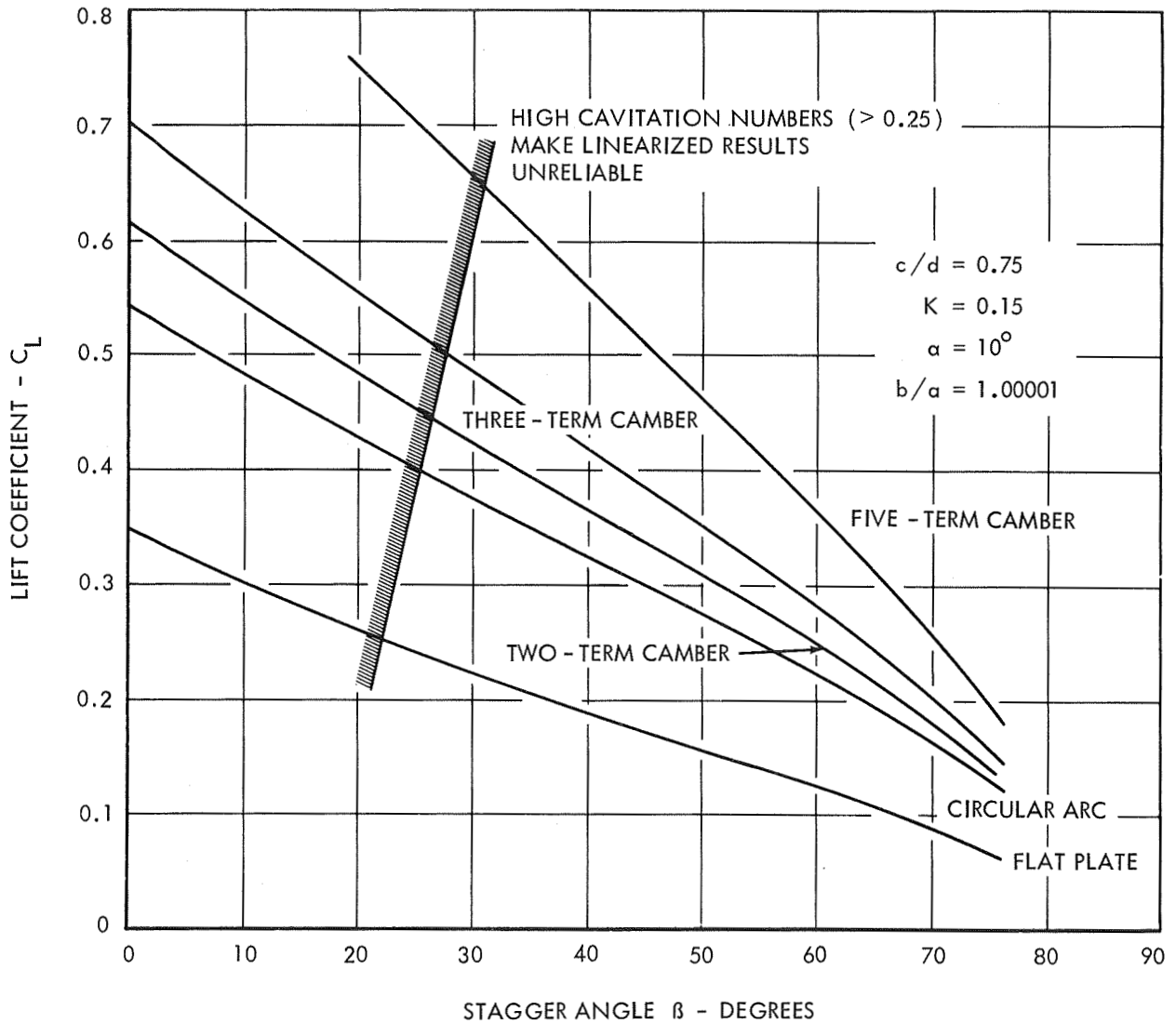


FIGURE 15 - INFLUENCE OF STAGGER ANGLE ON LIFT COEFFICIENT FOR 0.75 SOLIDITY FOR VARIOUS CAMBER TYPES

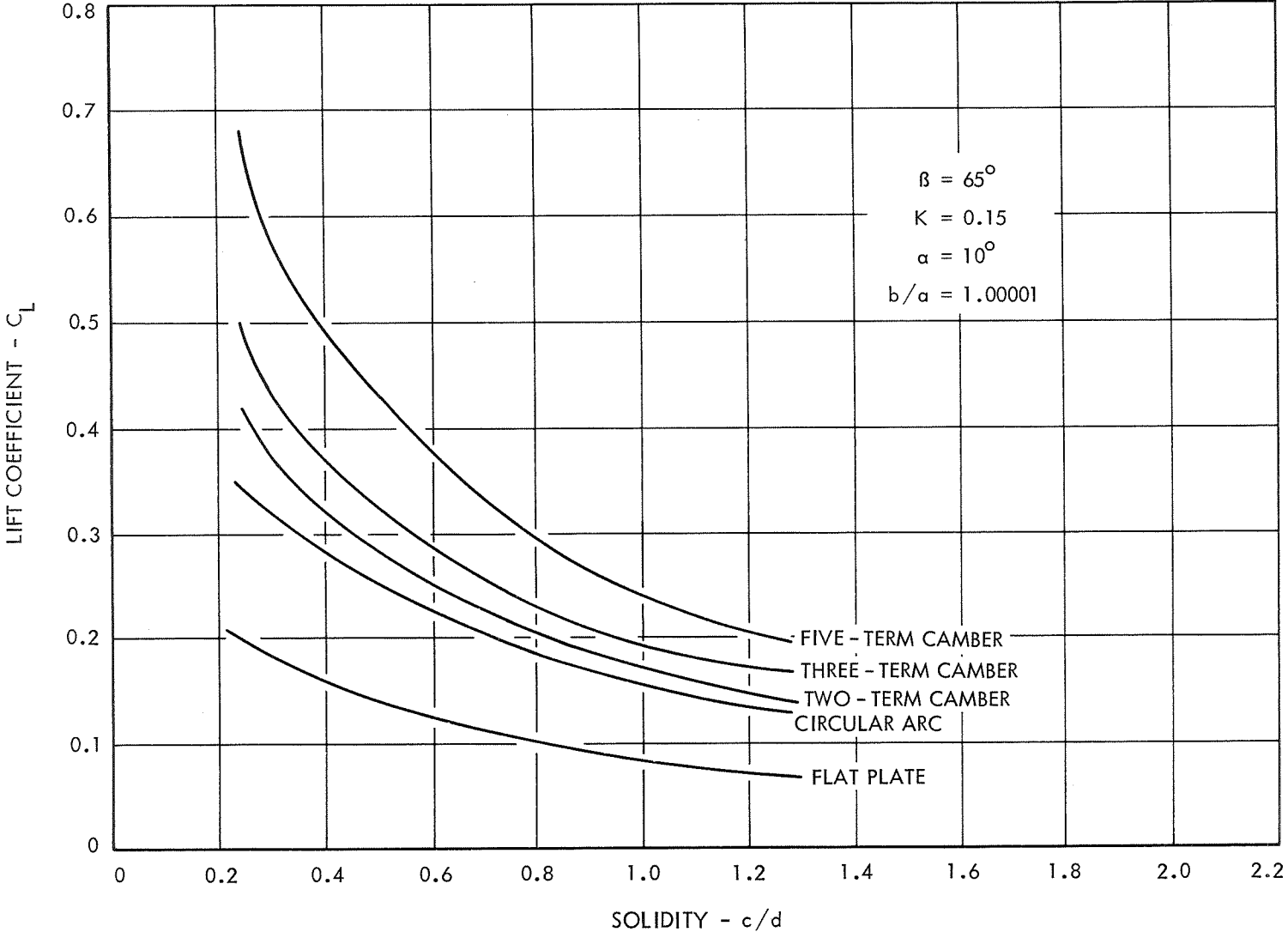


FIGURE 16 - INFLUENCE OF SOLIDITY ON LIFT COEFFICIENT FOR 65° STAGGER ANGLE AND VARIOUS CAMBER TYPES

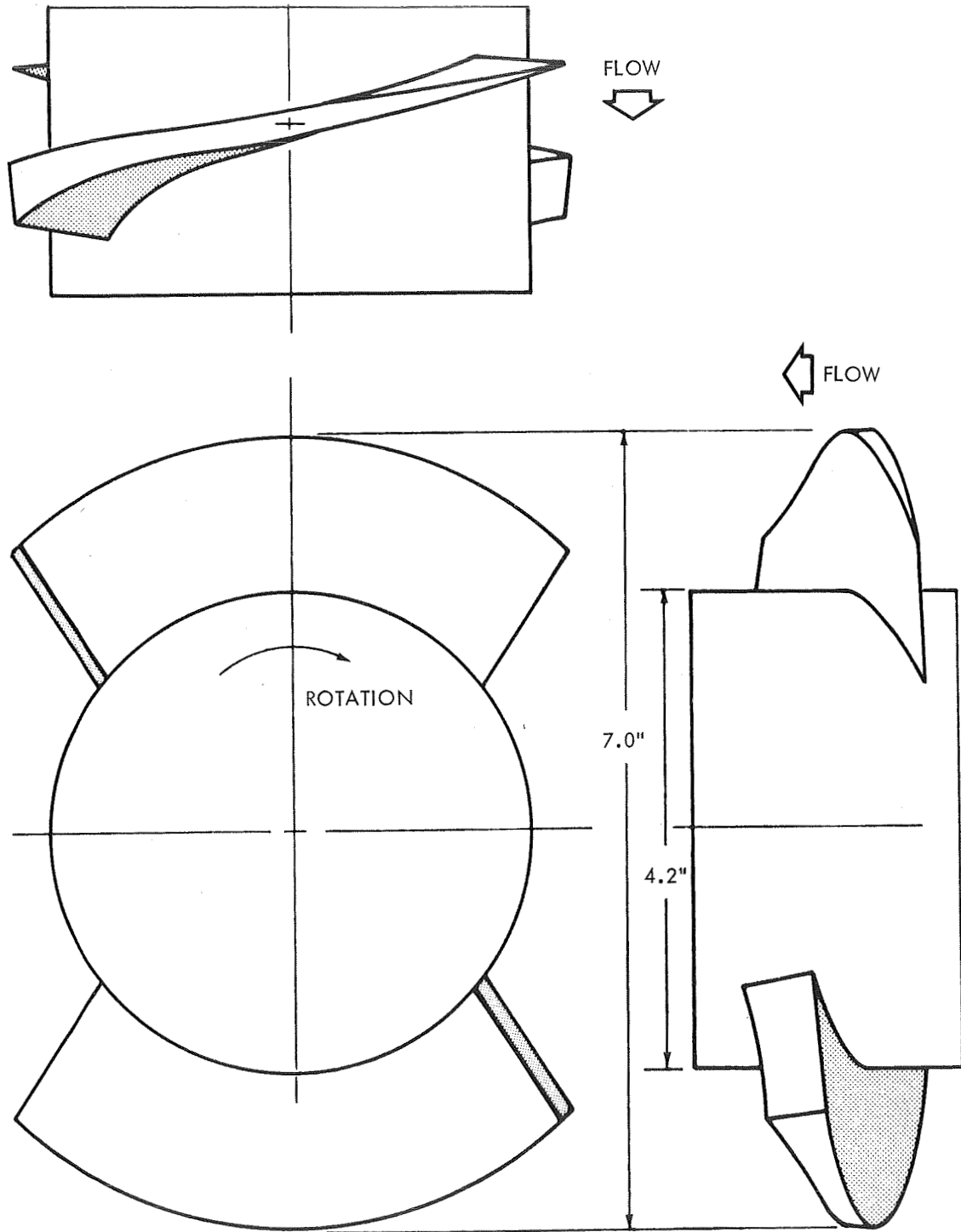


FIGURE 17 - FIVE-TERM CAMBERED, TWO BLADED, FIRST STAGE IMPELLER USING LINEAR CHORD LENGTH VARIATION

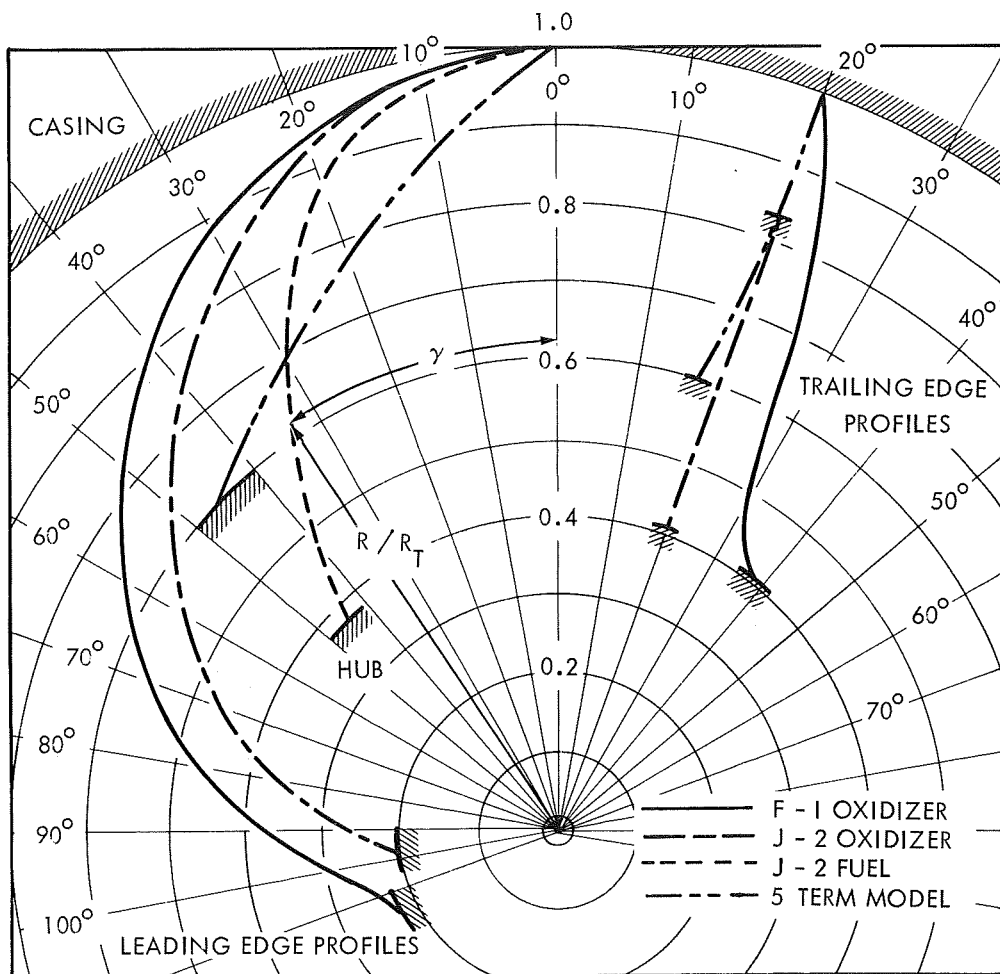


FIGURE 18 - COMPARISON OF LEADING AND TRAILING EDGE PROFILES USED IN SATURN V ENGINE INDUCERS TO 5-TERM CAMBERED MODEL WITH CONSTANT CHORD LENGTH

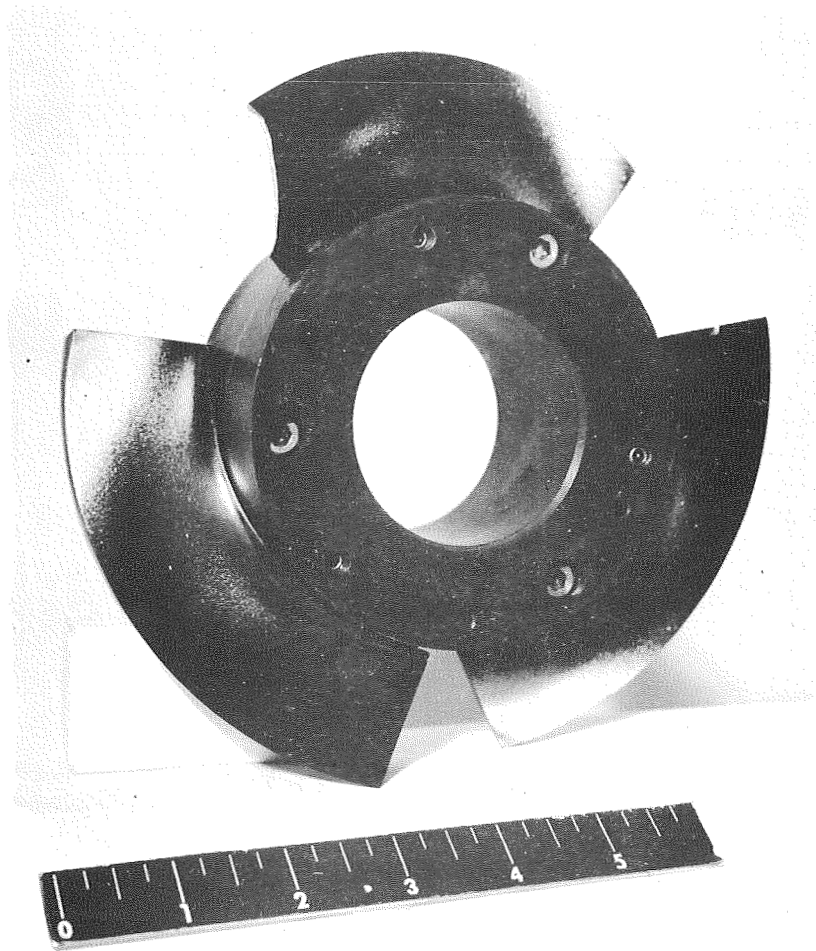


FIGURE 19 - PHASE I MODEL SHOWING FATIGUE FAILURE AT
OUTER PORTION OF LEADING EDGE

HYDRONAUTICS, INCORPORATED

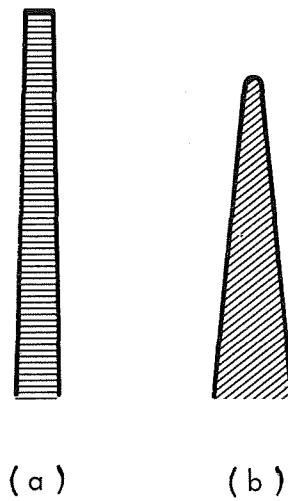


FIGURE 20 - SCHEMATIC RADIAL SECTIONS NEAR THE LEADING EDGE
(a) FOR AN INDUCER WITH RADIAL LEADING EDGE AND
(b) FOR AN INDUCER WITH A SWEEP LEADING EDGE.

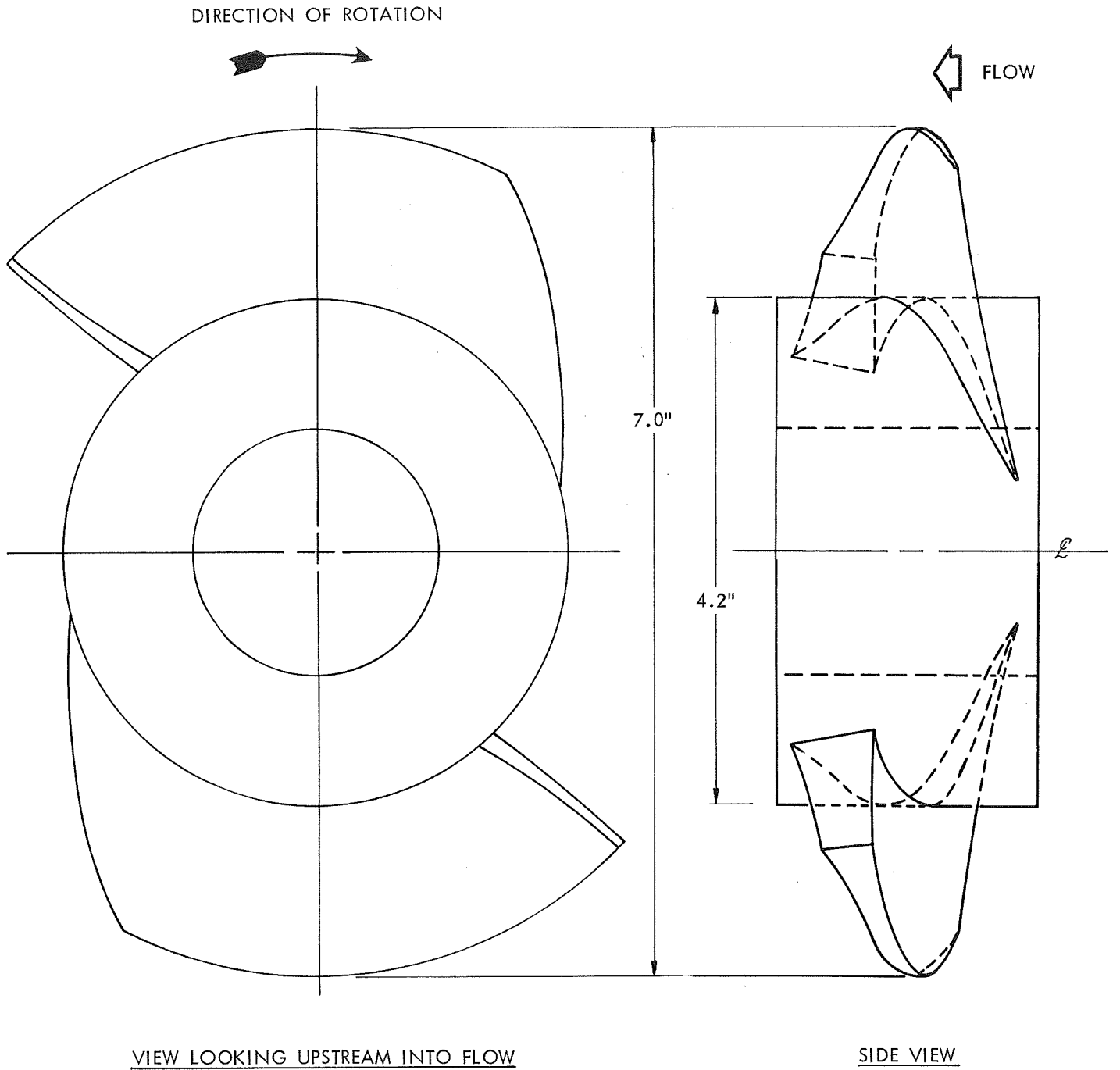
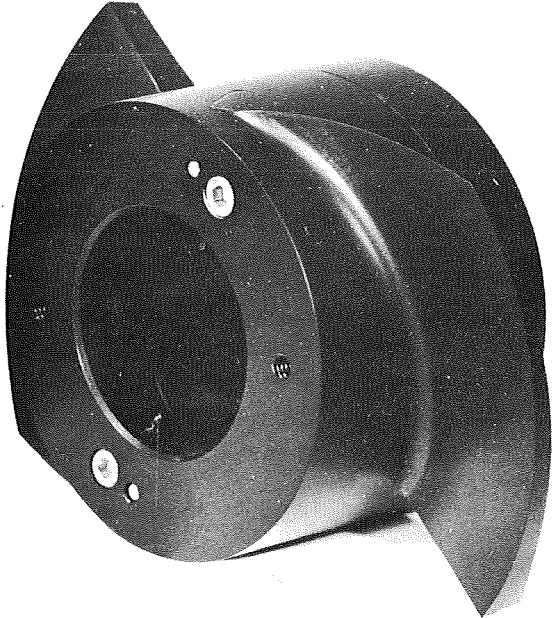


FIGURE 21 - STAGE 1, TWO-BLADED, SECOND ORDER DESIGN USING FIVE-TERM CAMBERED SECTIONS AND CONSTANT CHORD LENGTH



0 1 2 3 4 5 6

FIGURE 22 - STAGE ONE OF A TANDEM ROW INDUCER USING FIVE-TERM CAMBERED SUPERCAVITATING SECTIONS

HYDRONAUTICS, INCORPORATED

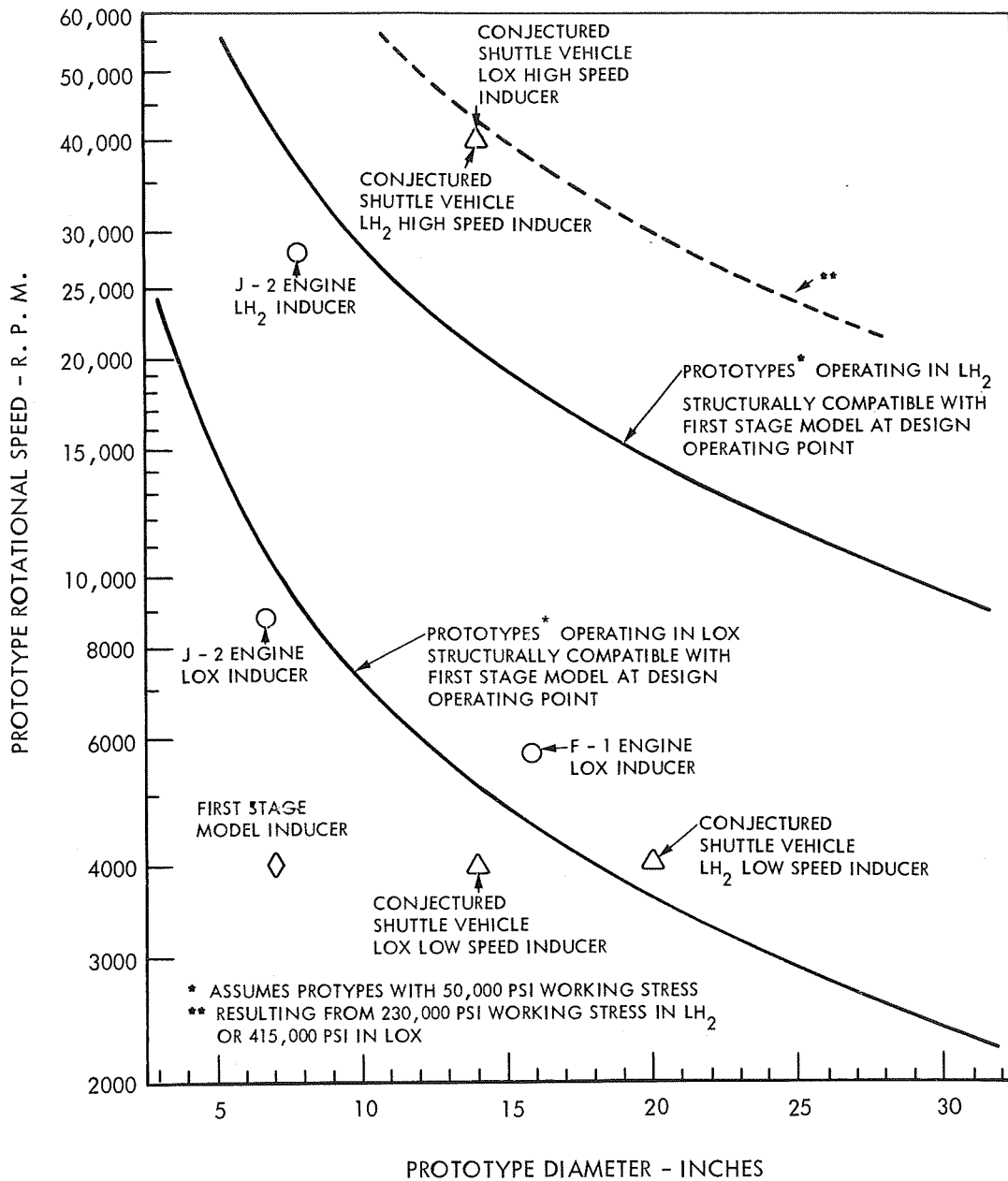


FIGURE 23 - STRUCTURAL COMPATIBILITY OF PHASE III FIRST STAGE MODEL HAVING FIVE-TERM CAMBER WITH PROTOTYPE INDUCERS OPERATING IN LH₂ AND LOX. ASSUMING 50,000 PSI PROTOTYPE WORKING STRESS.

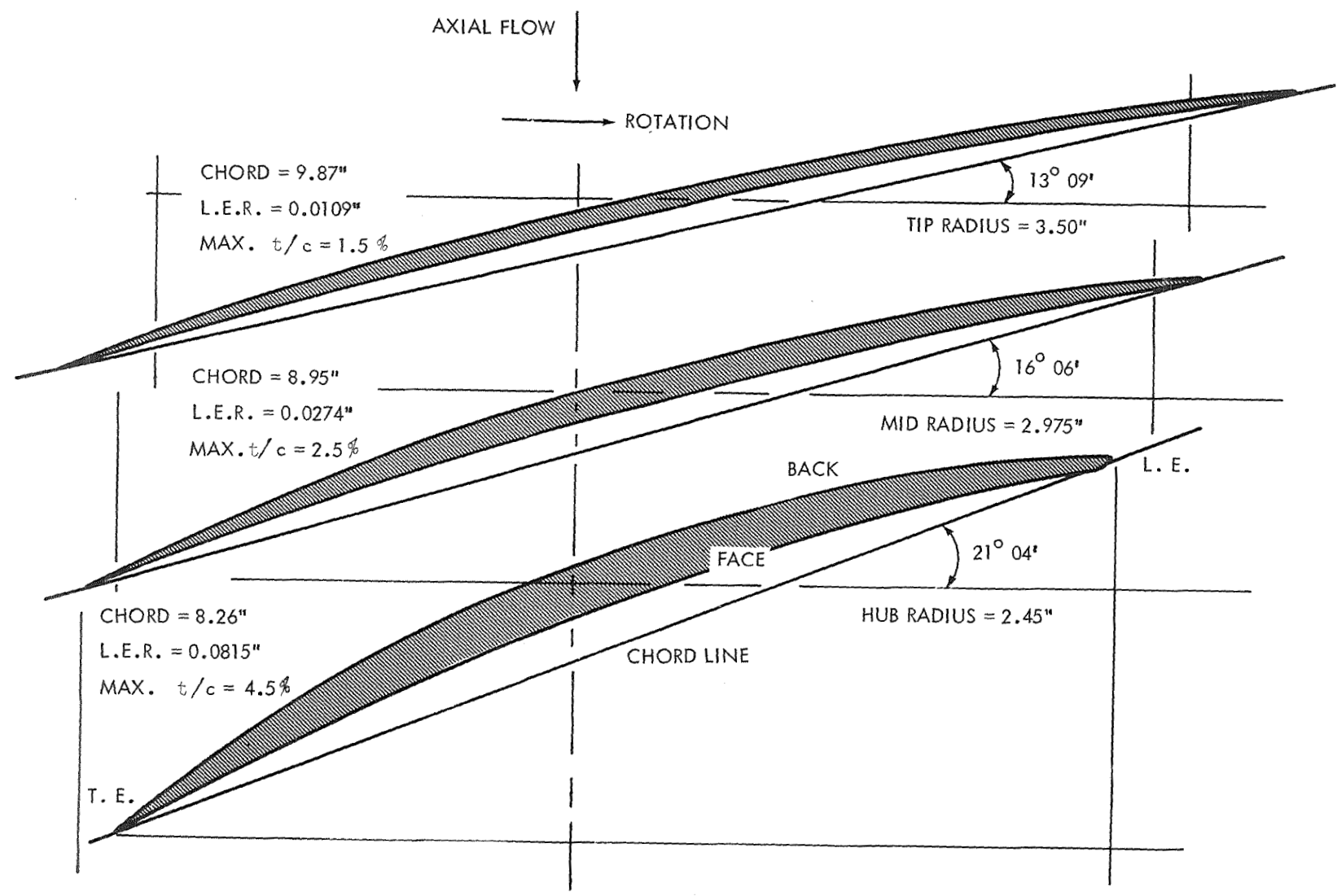


FIGURE 24 - SECOND STAGE TWO DIMENSIONAL BLADE PROFILES AT THREE RADII.
(FOUR BLADES, 0.70 HUB)

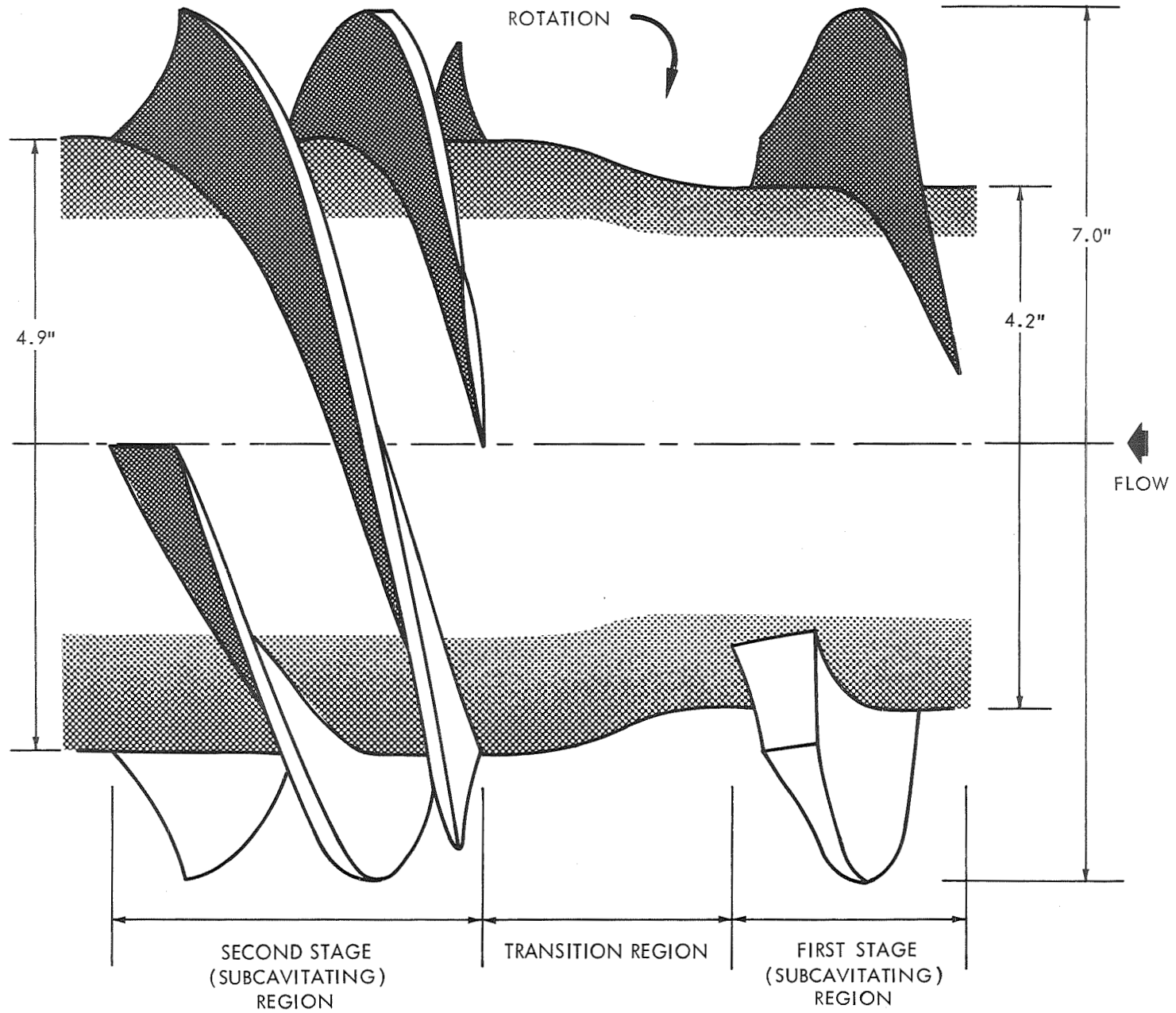


FIGURE 25 - THE TWO-BLADED FIVE - TERM CAMBERED FIRST STAGE IN TANDEM WITH A FOUR BLADED SUBCAVITATING SECOND STAGE HAVING A 0.7 HUB RATIO

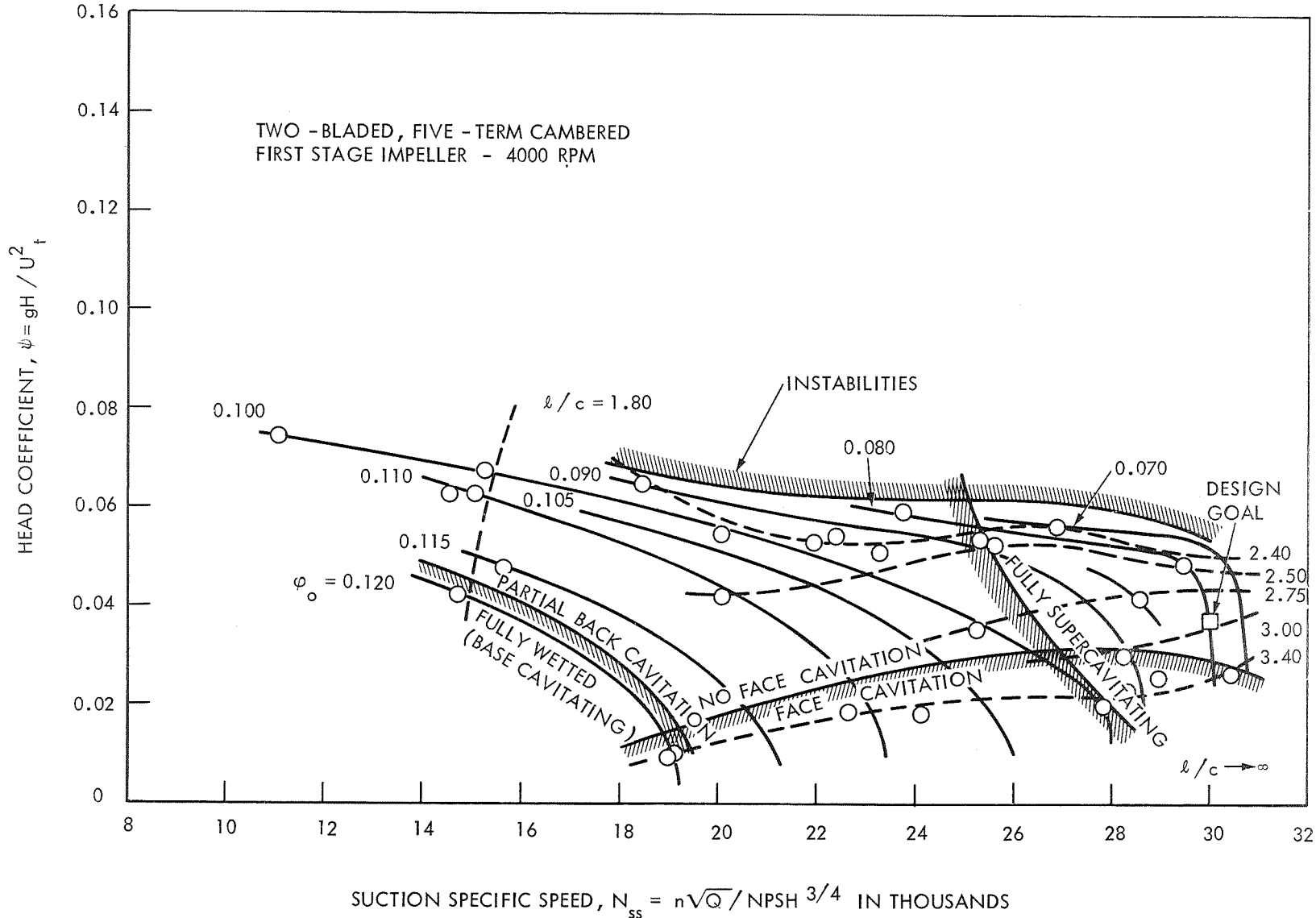


FIGURE 26 - HEAD COEFFICIENT AS A FUNCTION OF SUCTION SPECIFIC SPEED FOR A TWO - BLADED, FIVE - TERM CAMBERED FIRST STAGE IMPELLER

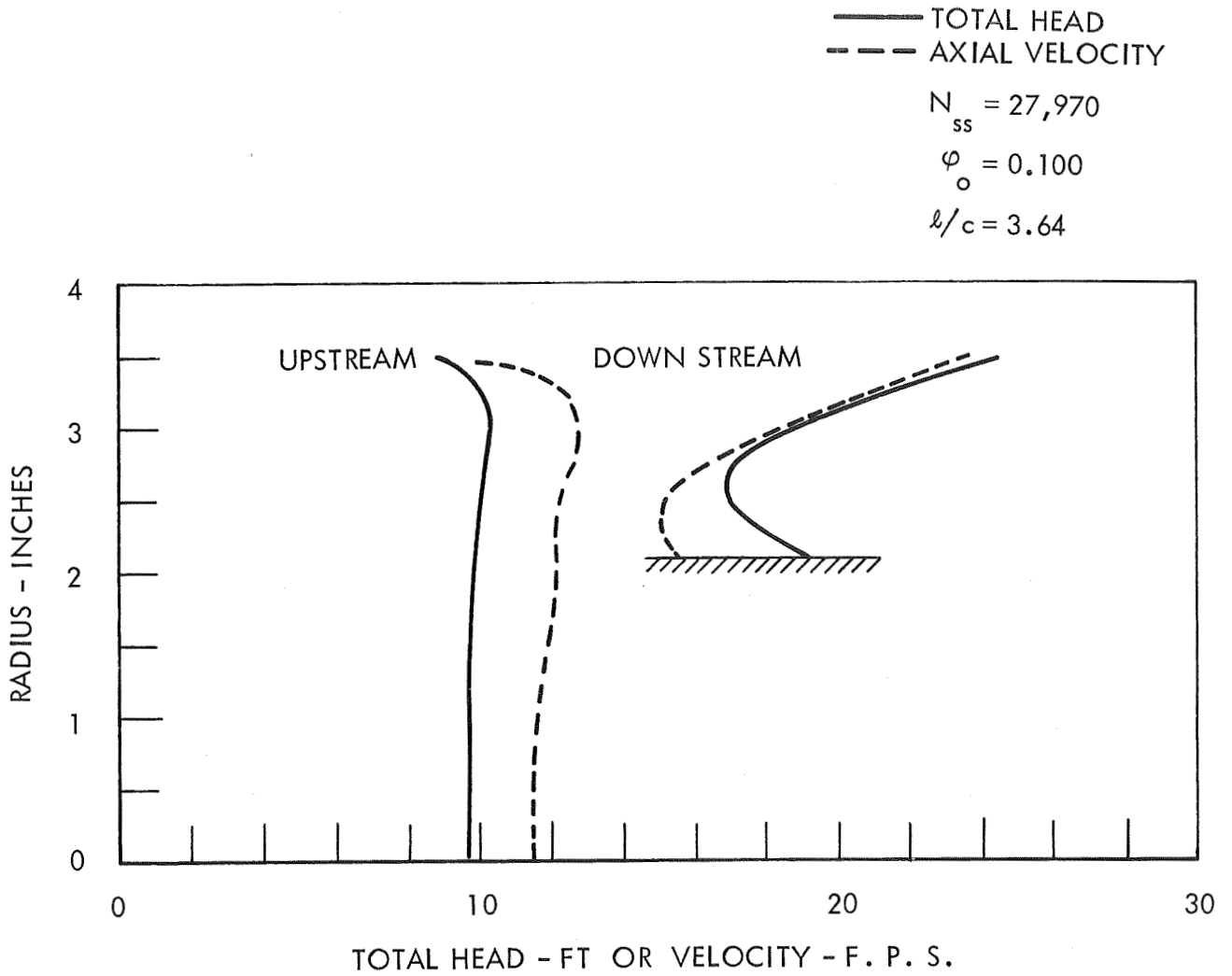


FIGURE 27 - TYPICAL RADIAL VARIATION OF AXIAL FLOW VELOCITY AND TOTAL HEAD

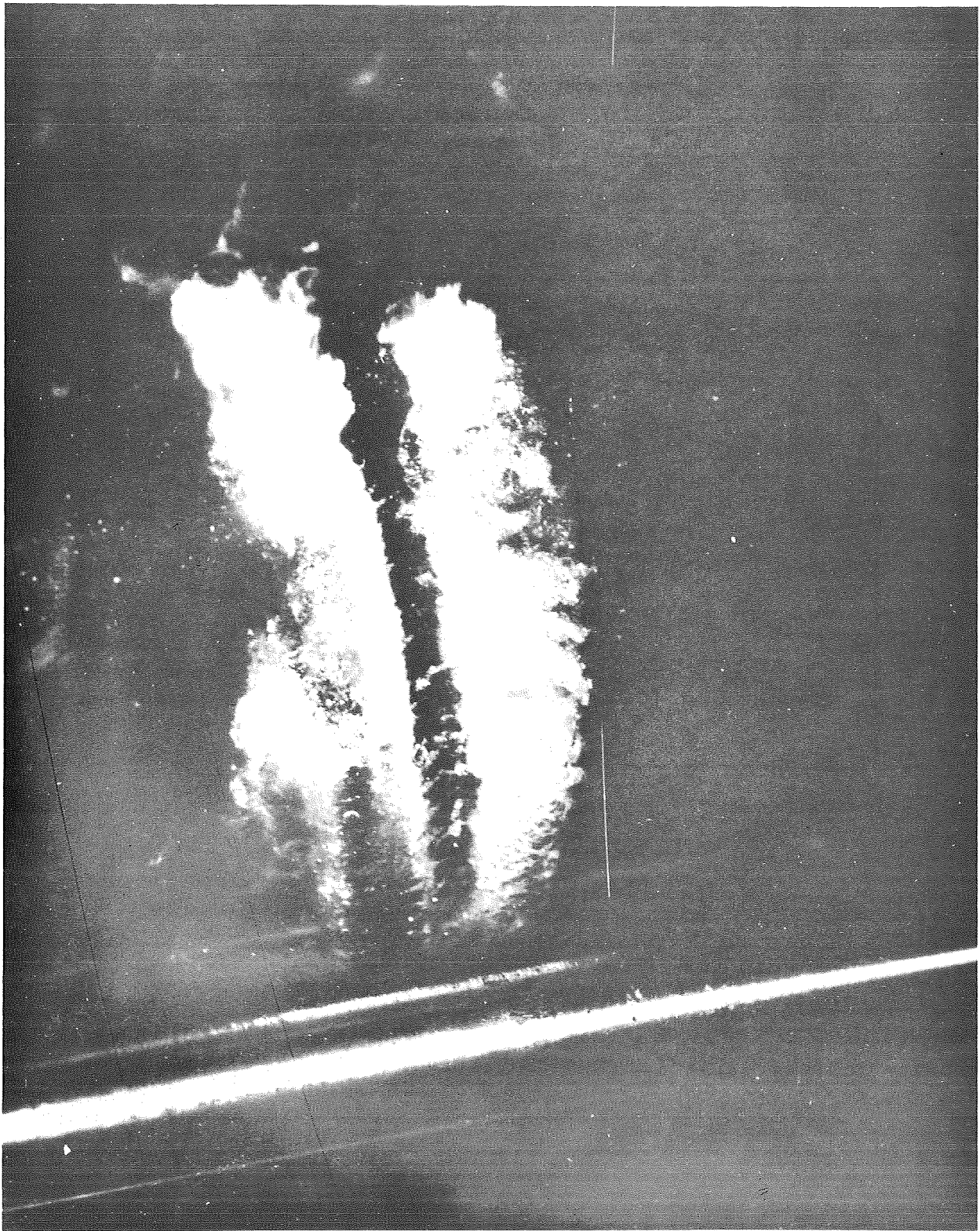


FIGURE 28 - PHOTOGRAPH OF CAVITATING OPERATION WITH $\phi_o = 0.10$, $l/c = 2.40$,
 $\psi = 0.055$, AND $N_{ss} = 20,500$.

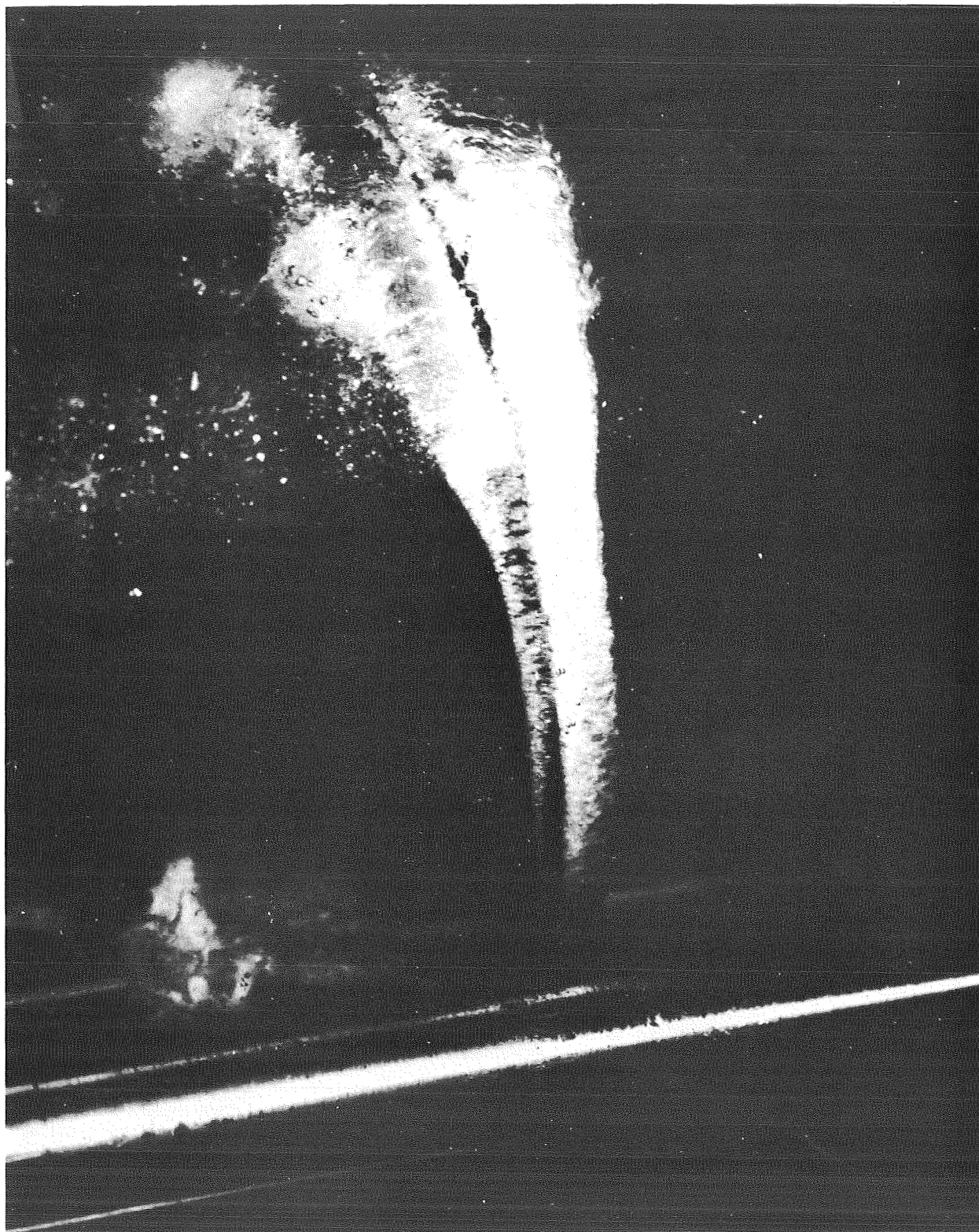


FIGURE 29 - PHOTOGRAPH OF CAVITATING OPERATION AT SAME
CONDITIONS AS IN FIGURE 28



FIGURE 30 - PHOTOGRAPH OF CAVITATING OPERATION WITH $\phi_0 = 0.10$, $l/c = 2.75$
 $\psi = 0.036$, AND $N_{ss} = 25,700$.

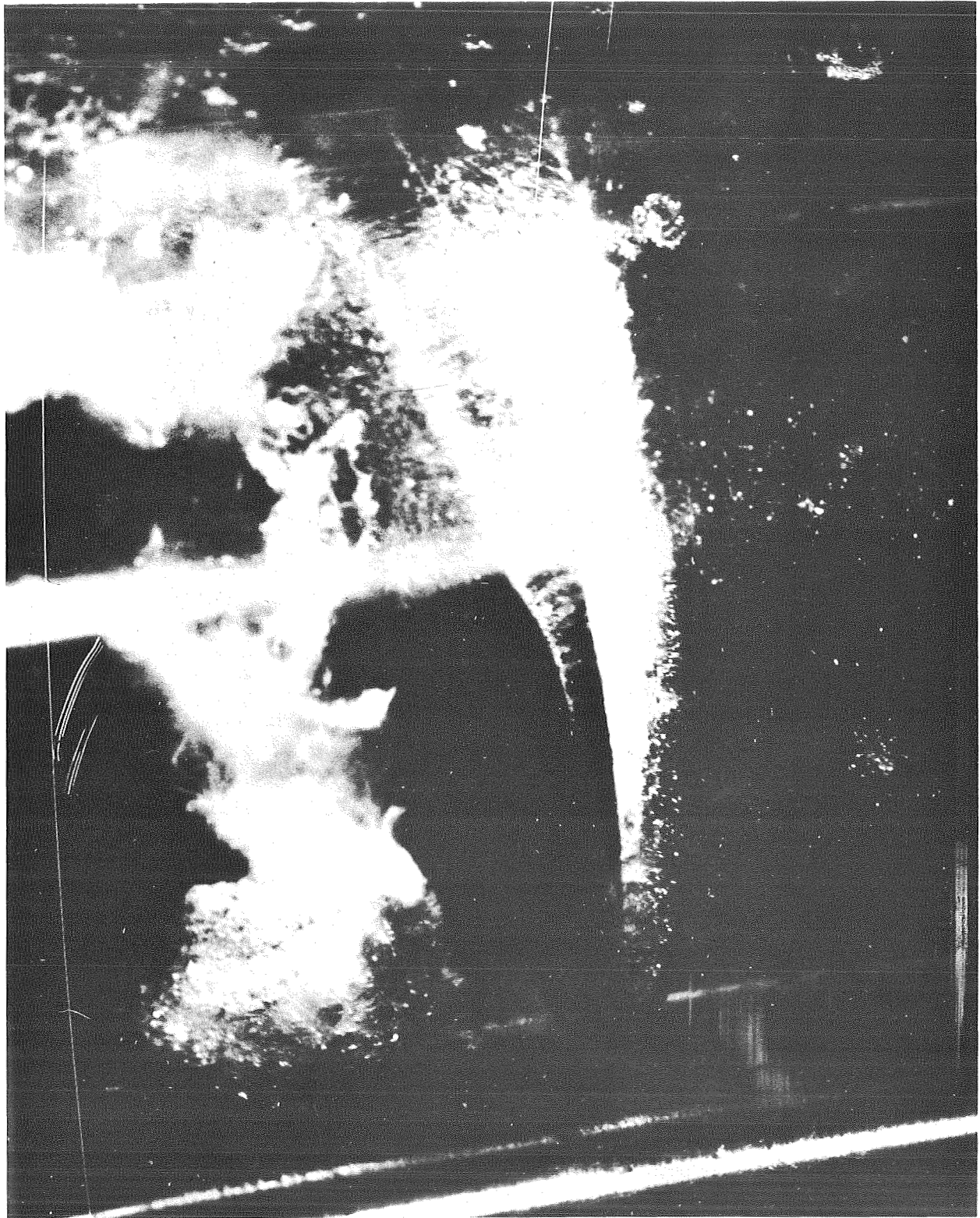


FIGURE 31 -- PHOTOGRAPH OF CAVITATING OPERATION WITH $\phi_o = 0.09$, $l/c = 3.10$,
 $\psi = 0.030$, AND $N_{ss} = 28,500$.

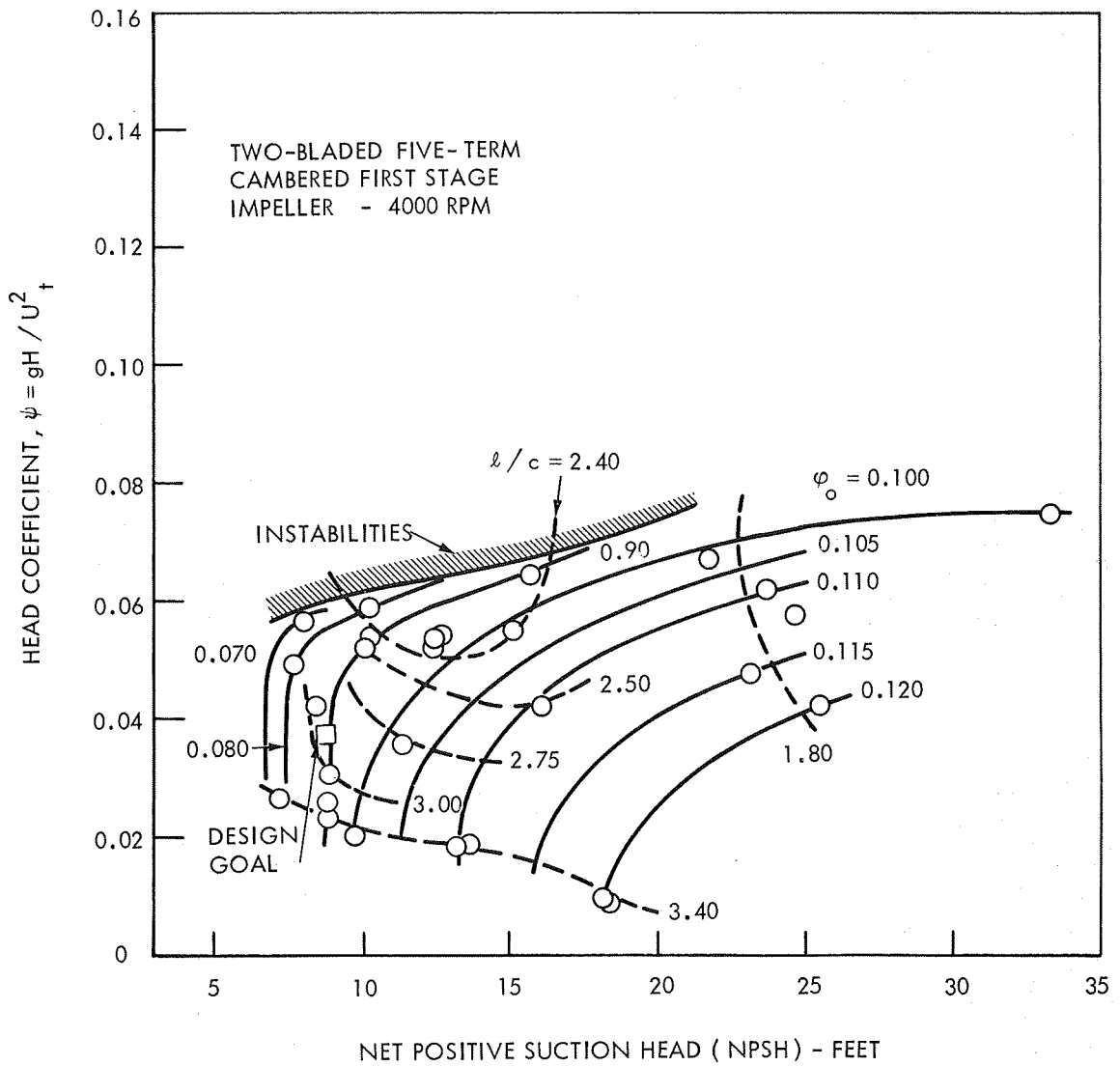


FIGURE 32 - EFFECT OF NPSH ON HEAD COEFFICIENT FOR A TWO-BLADED FIVE-TERM CAMBERED FIRST STAGE IMPELLER

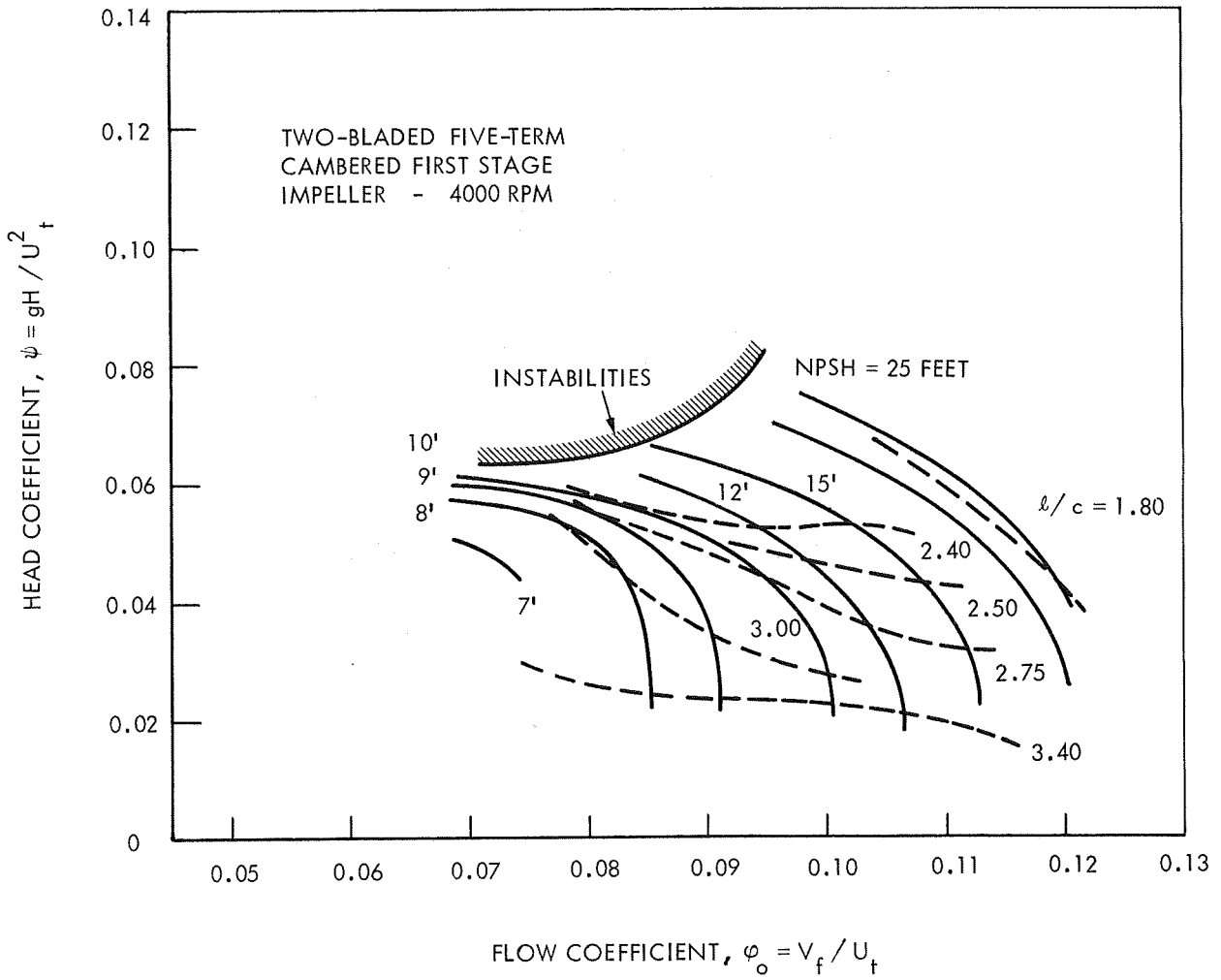


FIGURE 33 - HEAD COEFFICIENT AS A FUNCTION OF FLOW COEFFICIENT FOR A TWO-BLADED FIVE-TERM CAMBERED FIRST STAGE IMPELLER

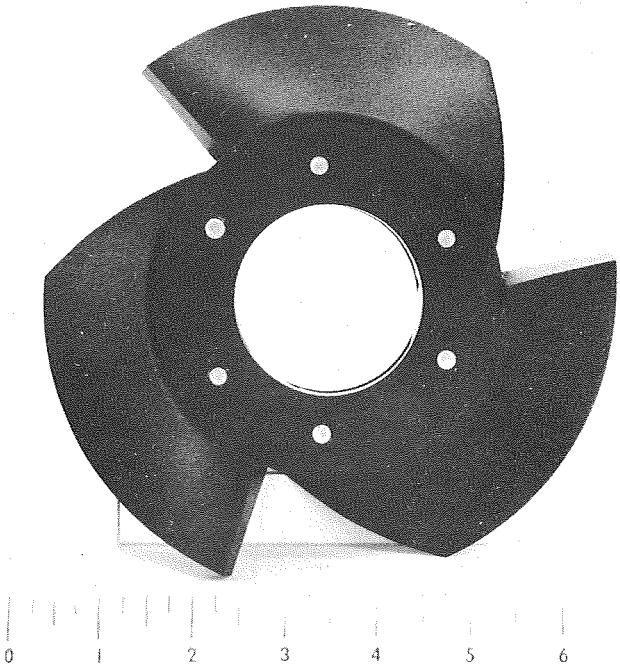


FIGURE 34 - THREE- BLADED FIVE-TERM CAMBERED FIRST STAGE INDUCER

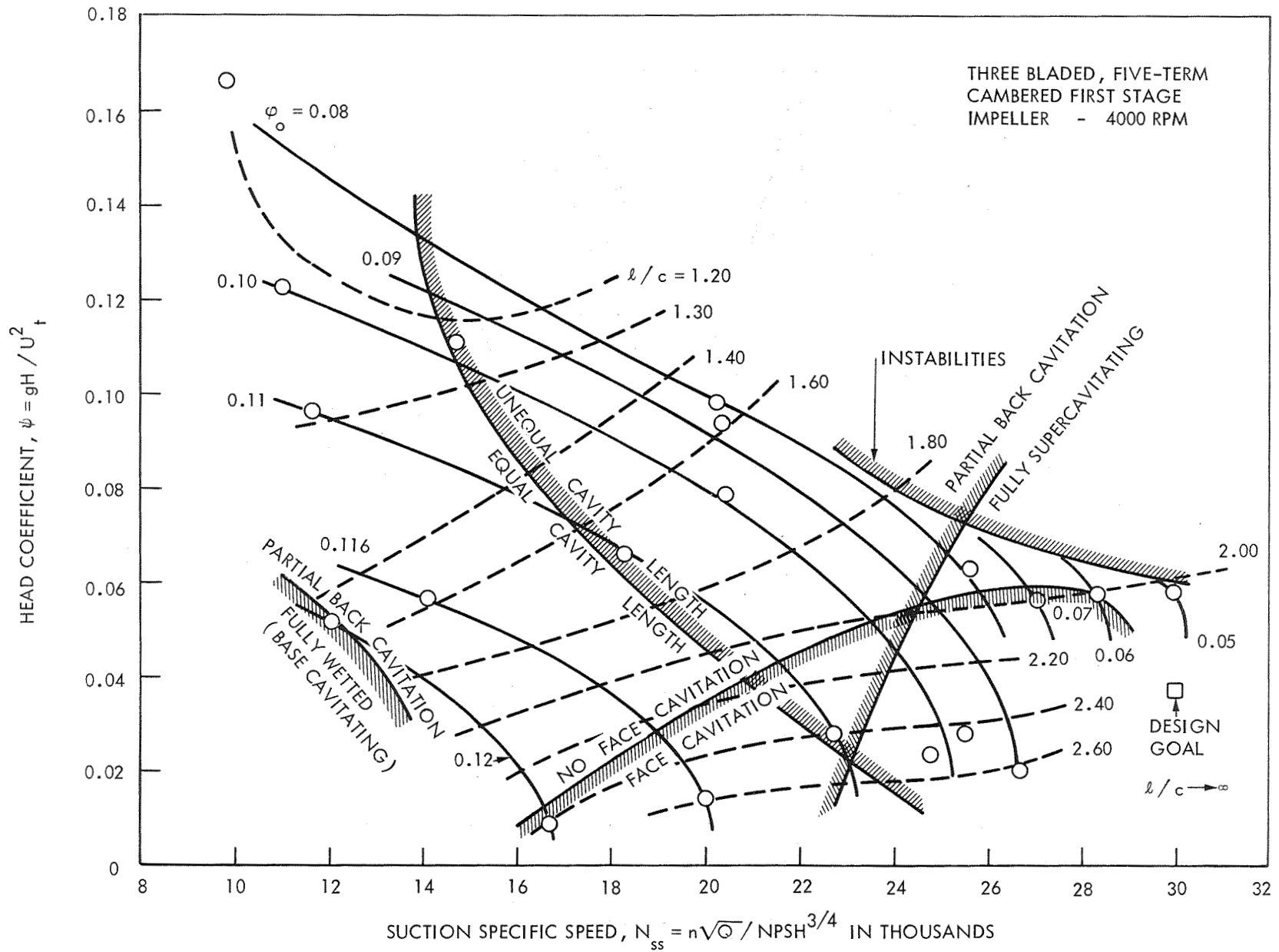


FIGURE 35 - HEAD COEFFICIENT AS A FUNCTION OF SUCTION SPECIFIC SPEED FOR A THREE-BLADED, FIVE-TERM CAMBERED FIRST STAGE IMPELLER

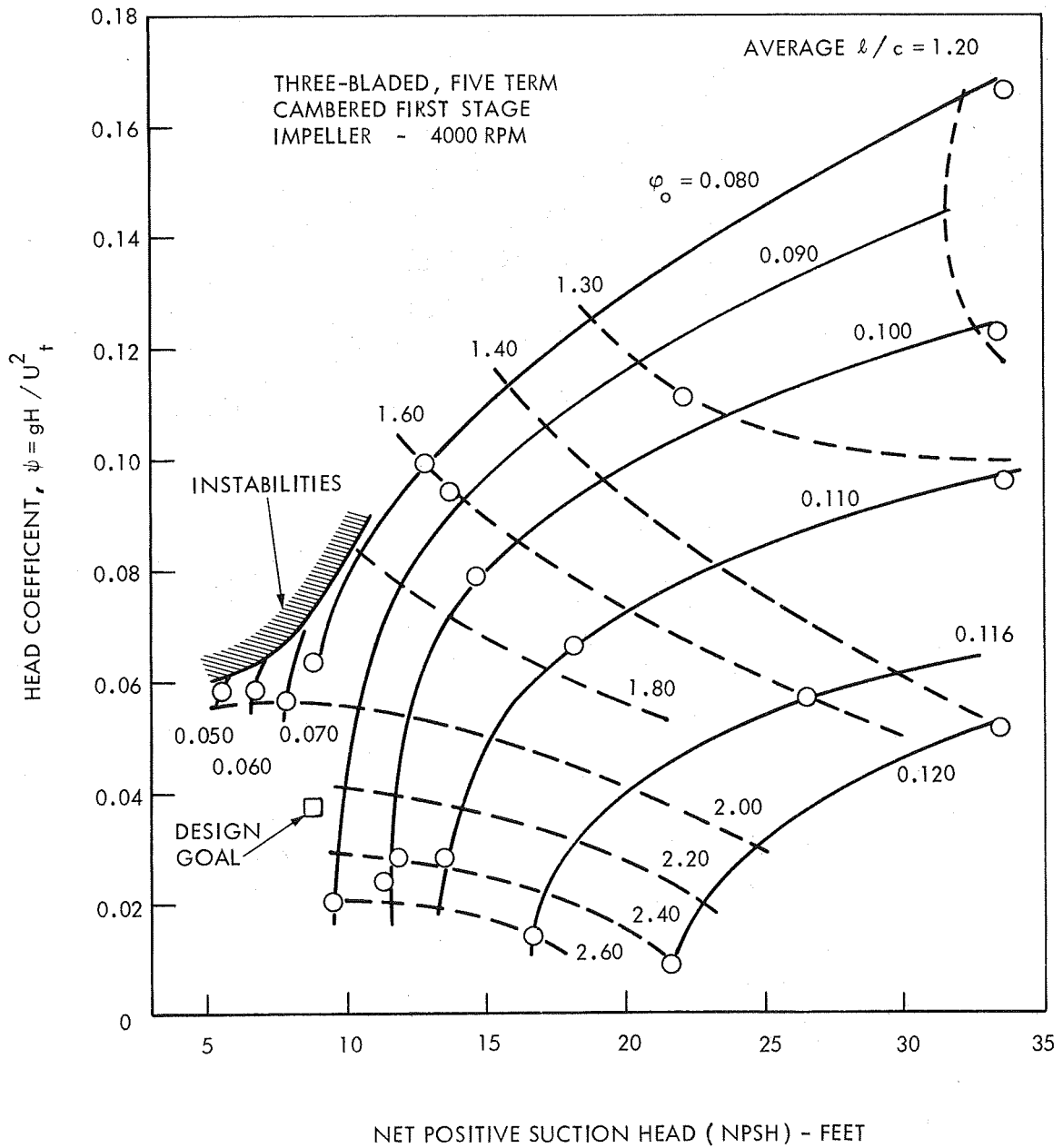


FIGURE 36 - EFFECT OF NPSH ON HEAD COEFFICIENT FOR THE THREE-BLADED, FIVE-TERM CAMBERED FIRST STAGE IMPELLER .

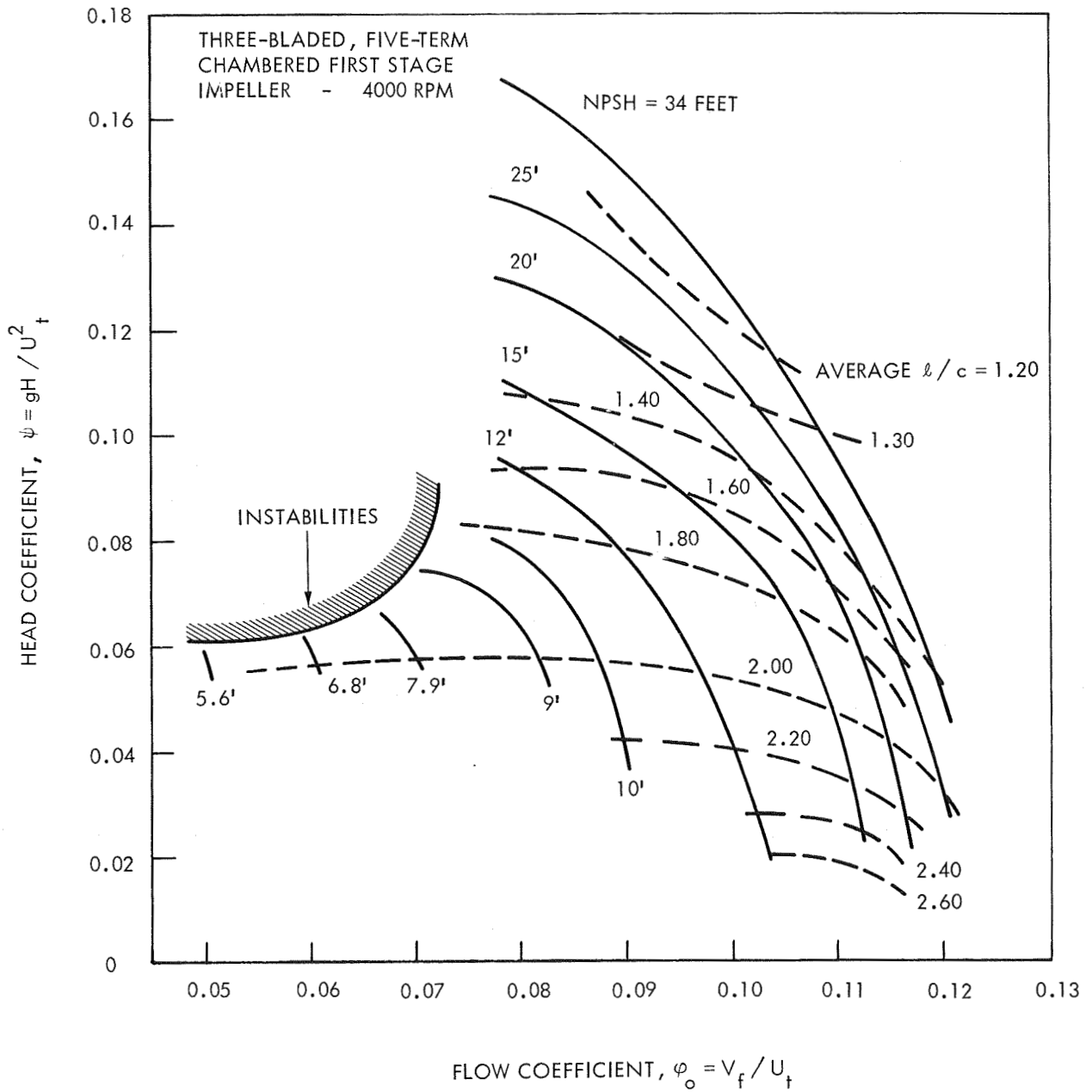


FIGURE 37 - HEAD COEFFICIENT AS A FUNCTION OF FLOW COEFFICIENT FOR A THREE-BLADED, FIVE-TERM CAMBERED FIRST STAGE IMPELLER.

HYDRONAUTICS, INCORPORATED

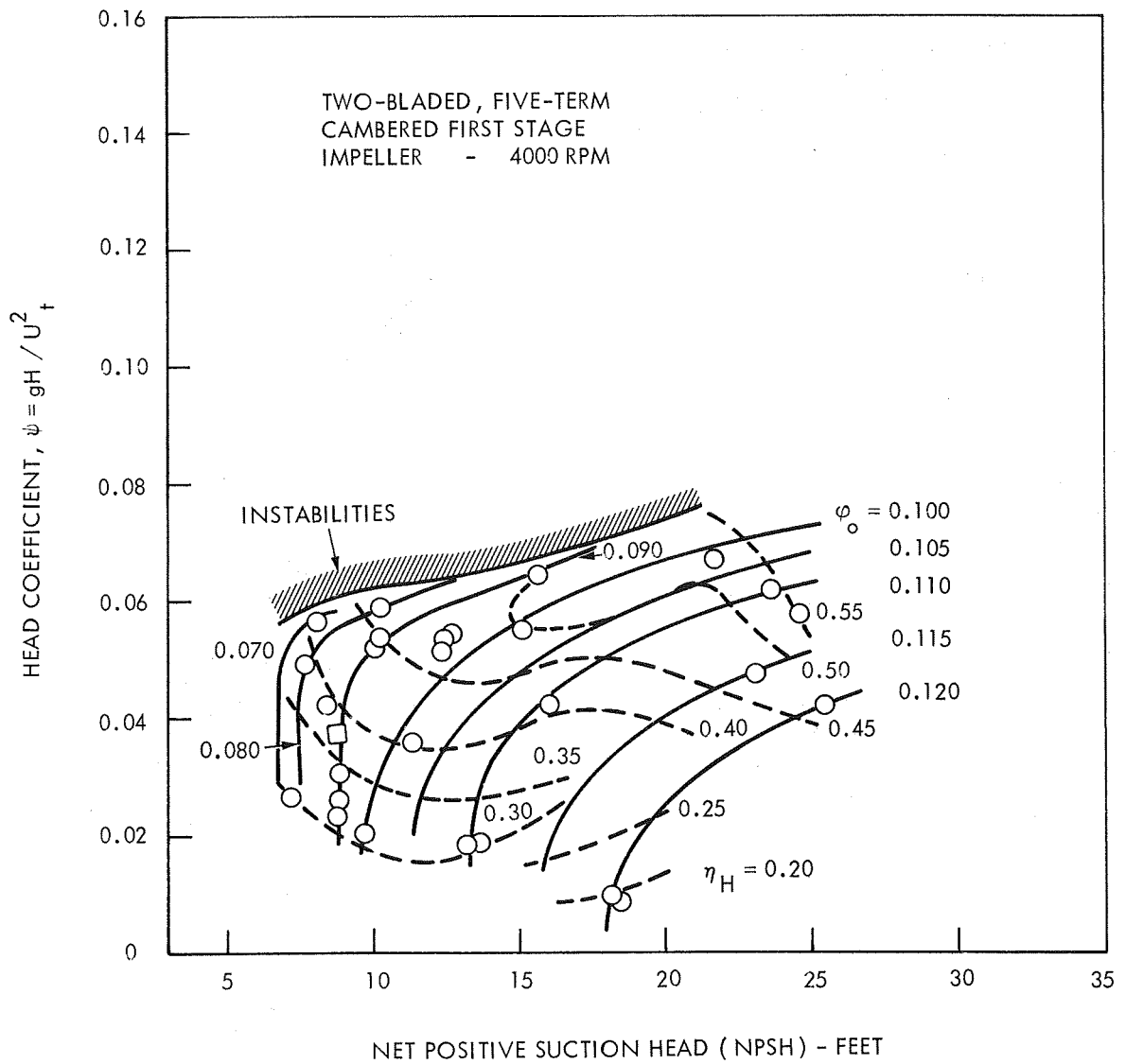


FIGURE 38 - EFFECT OF NPSH AND HEAD COEFFICIENT ON HYDRAULIC EFFICIENCY FOR A TWO-BLADED, FIVE-TERM CAMBERED FIRST STAGE IMPELLER

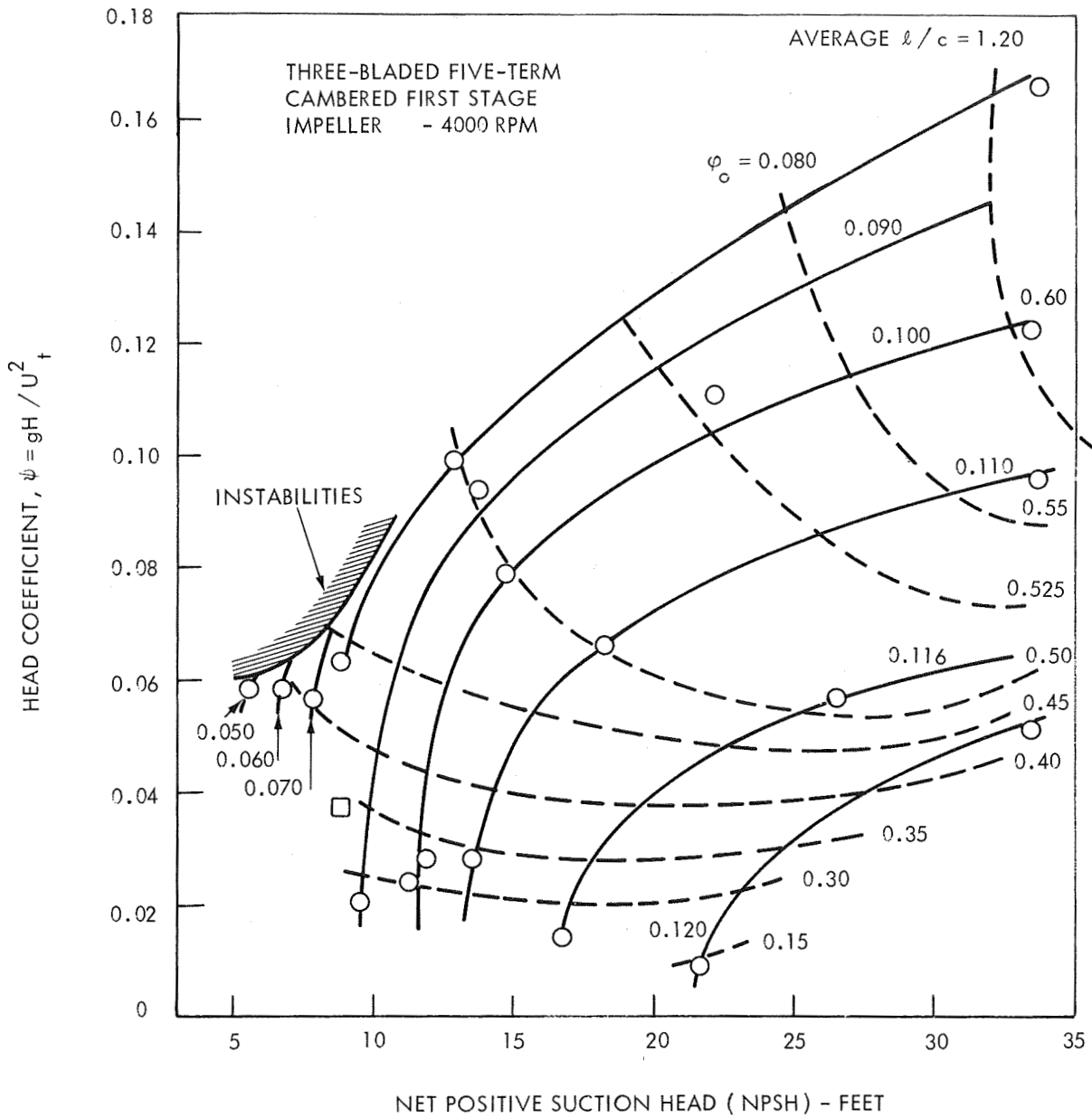
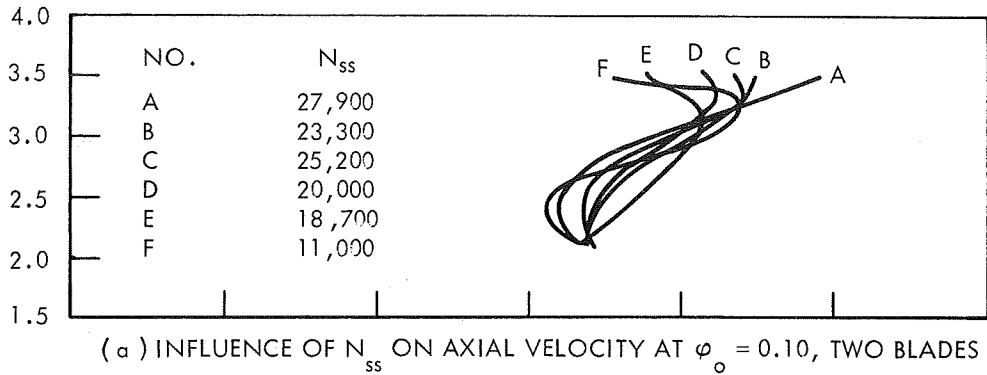


FIGURE 39 - EFFECT OF NPSH AND HEAD COEFFICIENT ON HYDRAULIC EFFICIENCY FOR A THREE-BLADED, FIVE-TERM CAMBERED FIRST STAGE IMPELLER



RADIAL LOCATION IN INCHES

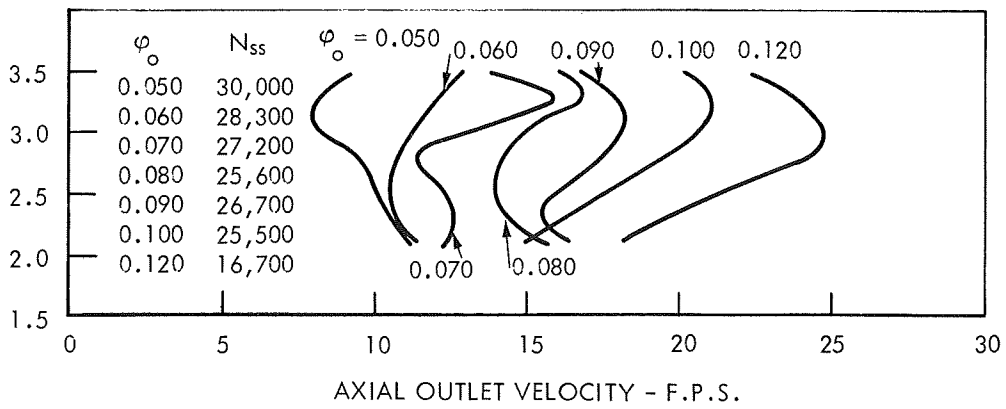
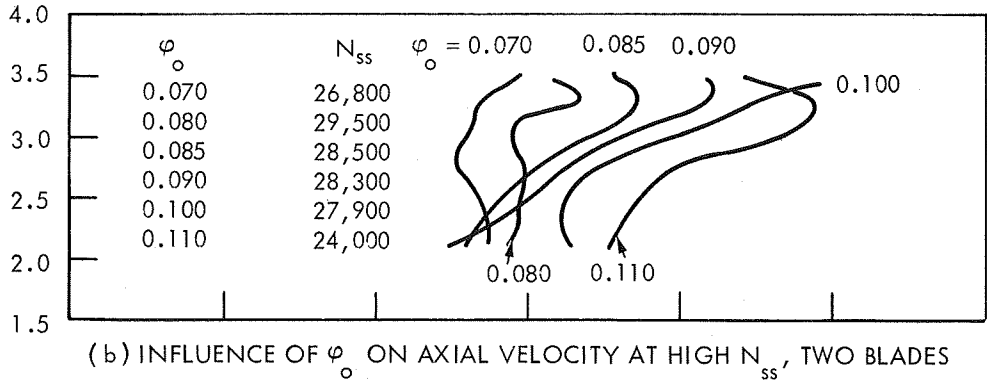


FIGURE 40 - INFLUENCE OF ϕ_o AND N_{ss} ON TYPICAL AXIAL OUTLET VELOCITY PROFILES FOR THE TWO AND THREE BLADED, FIVE-TERM CAMBERED FIRST STAGE INDUCERS

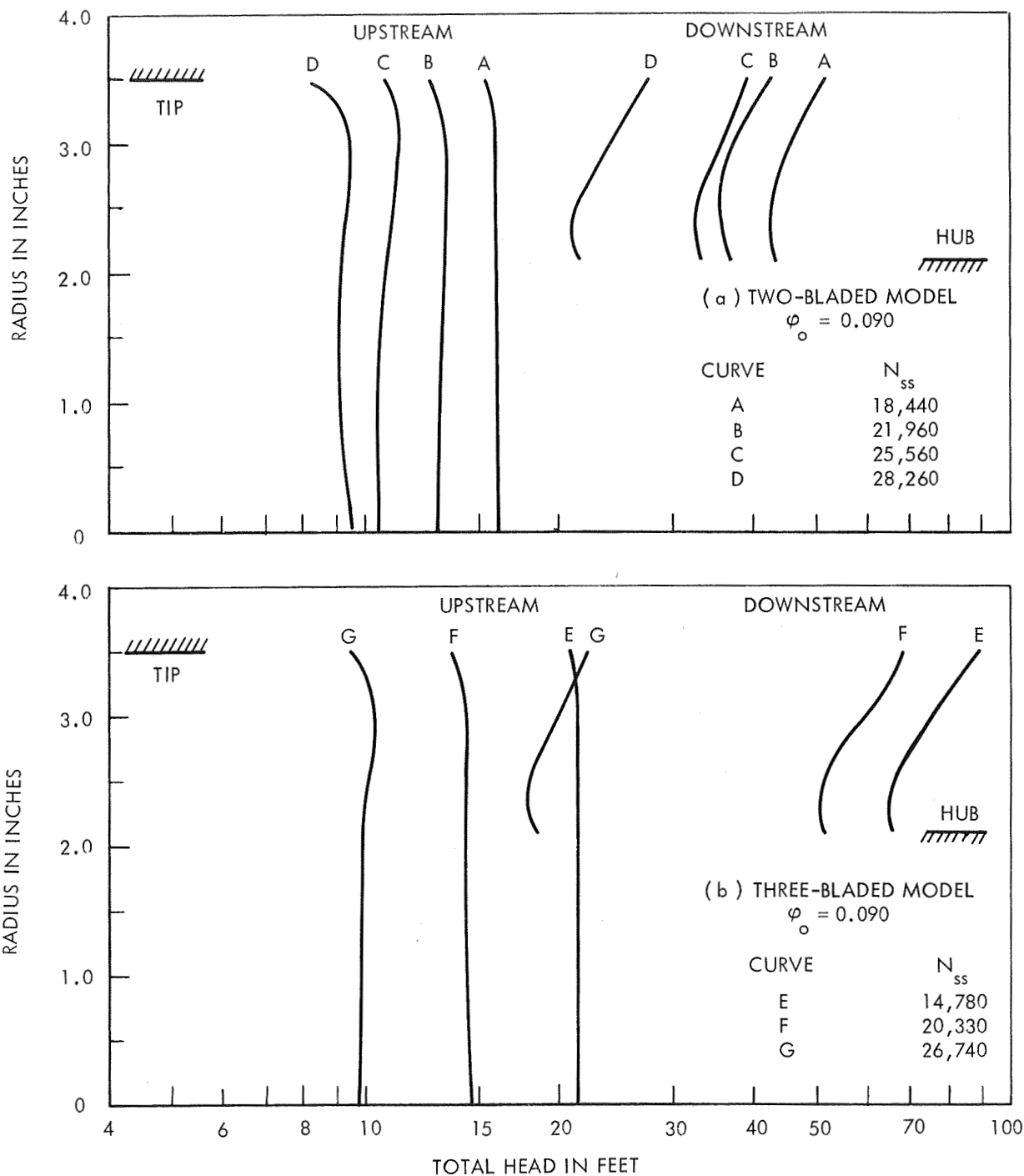


FIGURE 41 - TYPICAL RADIAL VARIATION OF INLET AND OUTLET TOTAL HEAD FOR THE TWO-BLADED AND THREE-BLADED FIVE-TERM CAMBERED FIRST STAGE INDUCERS AT $\phi_o = 0.090$

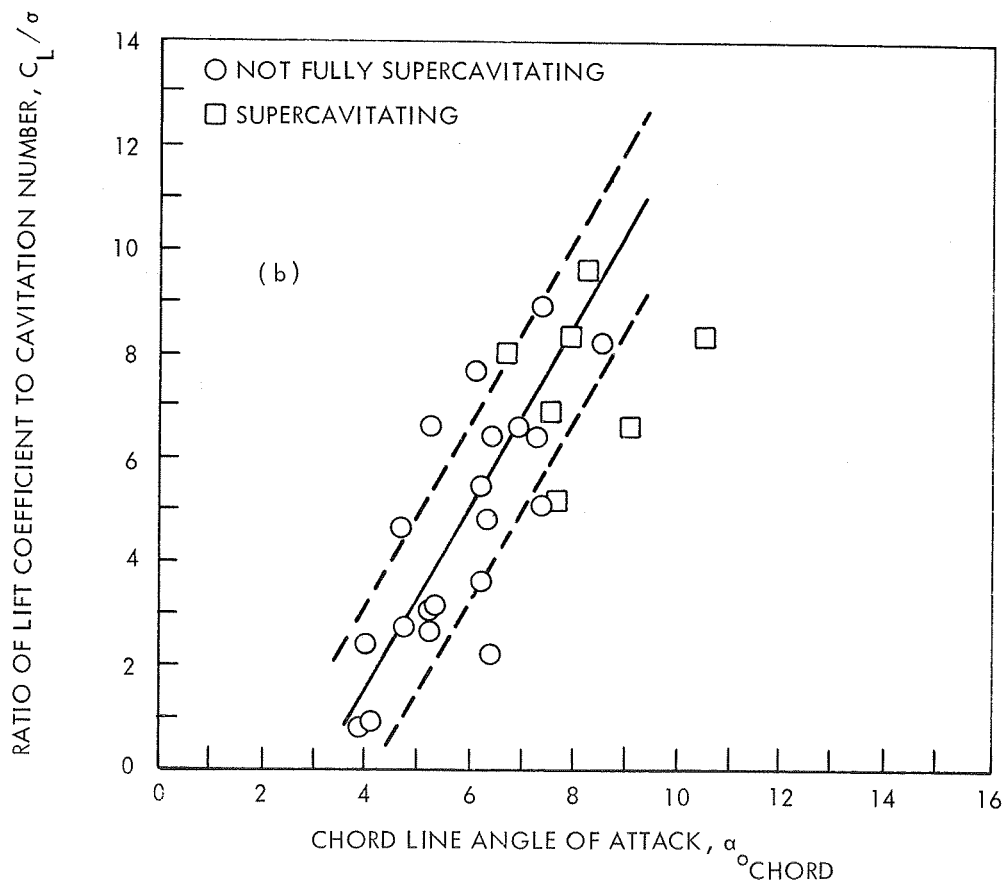
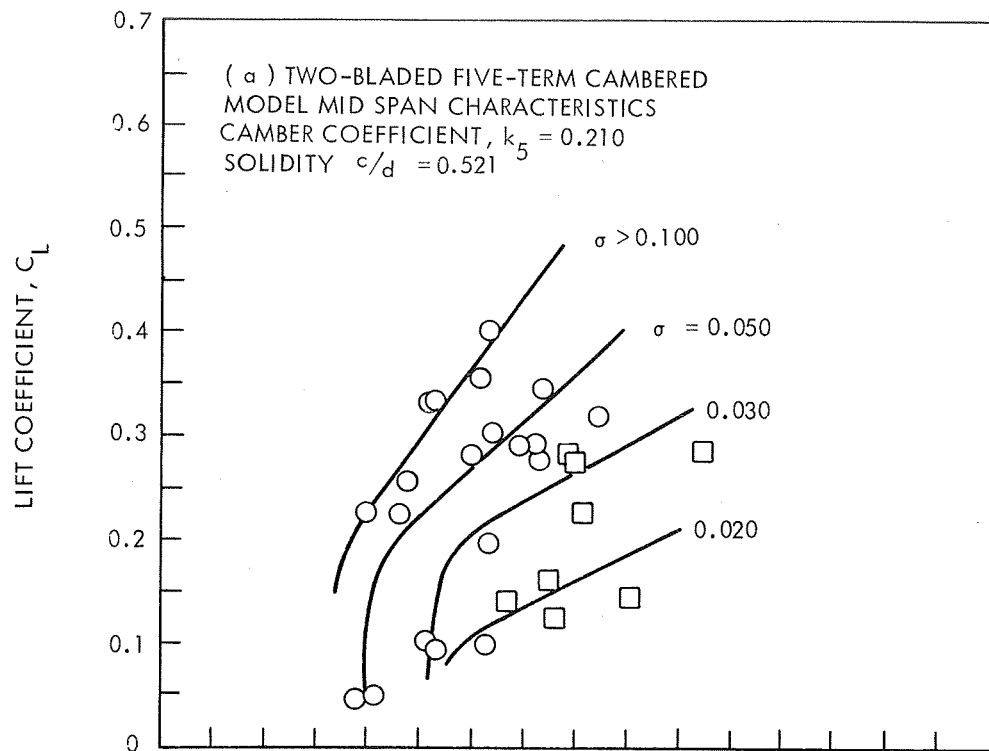


FIGURE 42 - MID-SPAN LIFT COEFFICIENT AND RATIO OF LIFT COEFFICIENT TO CAVITATION NUMBER AS A FUNCTION OF CHORD LINE ANGLE OF ATTACK FOR THE TWO-BLADED, FIVE-TERM CAMBERED MODEL

HYDRONAUTICS, INCORPORATED

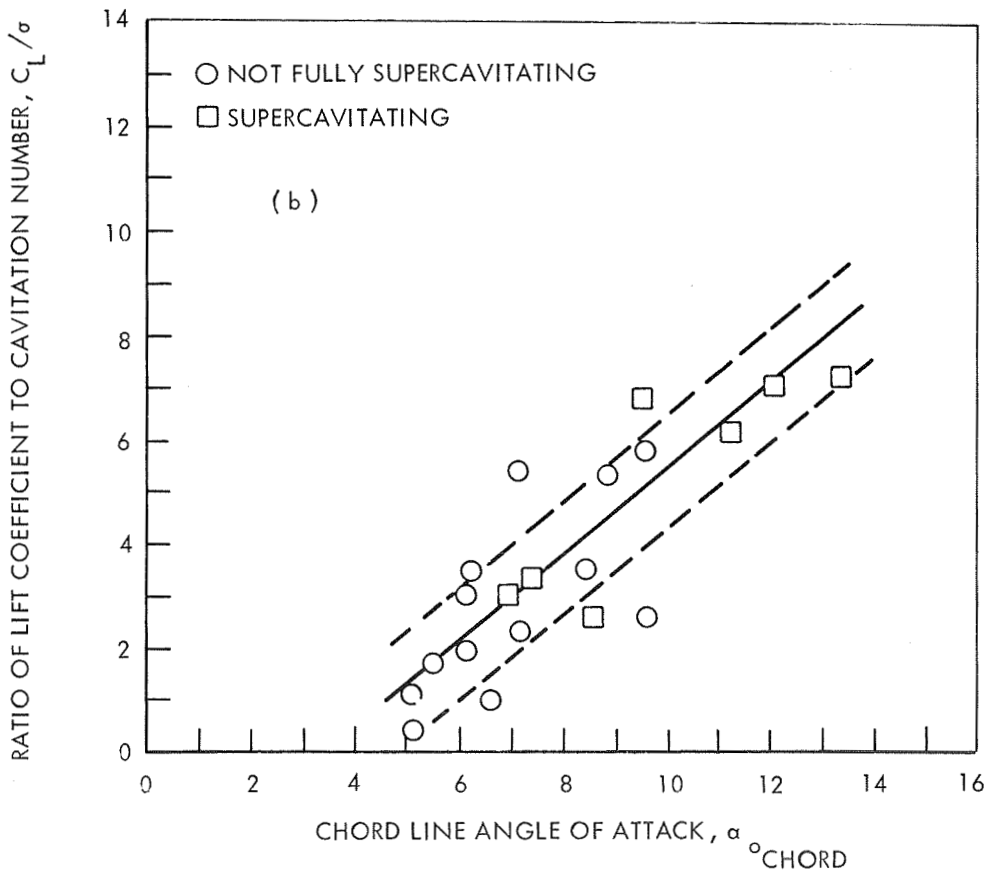
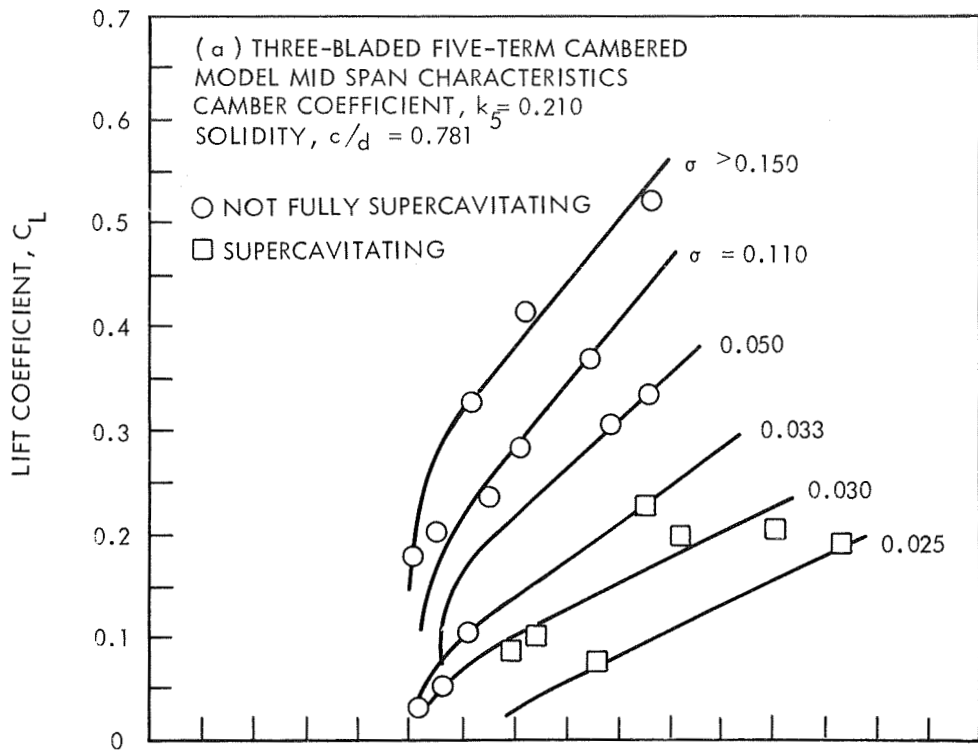


FIGURE 43- MID-SPAN LIFT COEFFICIENT AND RATIO OF LIFT COEFFICIENT TO CAVITATION NUMBER AS A FUNCTION OF CHORD LINE ANGLE OF ATTACK FOR THE THREE BLADED, FIVE TERM CAMBERED MODEL

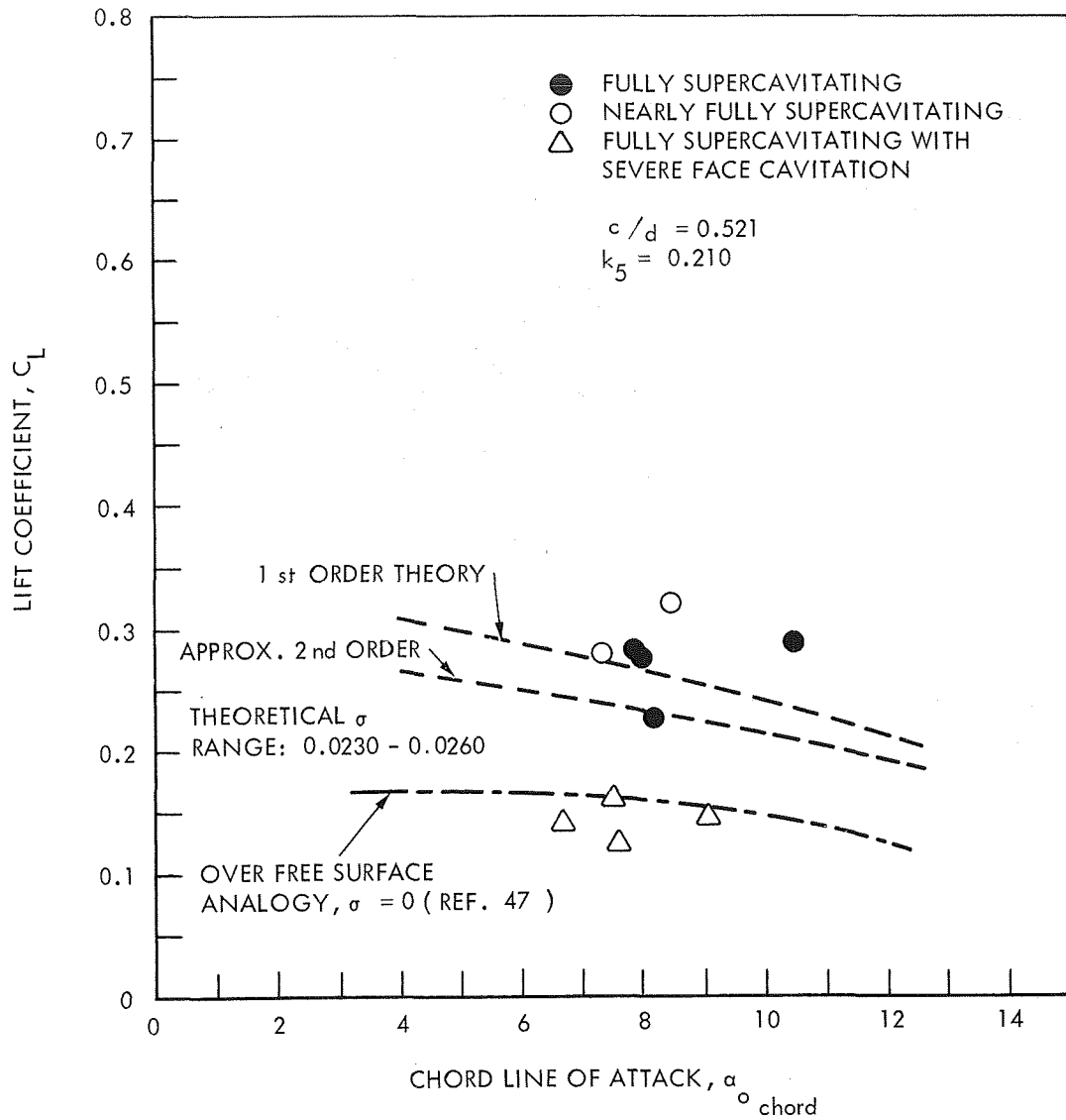


FIGURE 44 - COMPARISON OF TWO-DIMENSIONAL LINEARIZED THEORY (REF. 28) TO EXPERIMENTALLY MEASURED LIFT AND ANGLE OF ATTACK AT MID-SPAN FOR THE TWO-BLADED, FIVE-TERM CAMBERED FIRST STAGE MODEL CONSIDERING ONLY DATA AT OR VERY NEAR FULLY SUPERCAVITATING OPERATION.

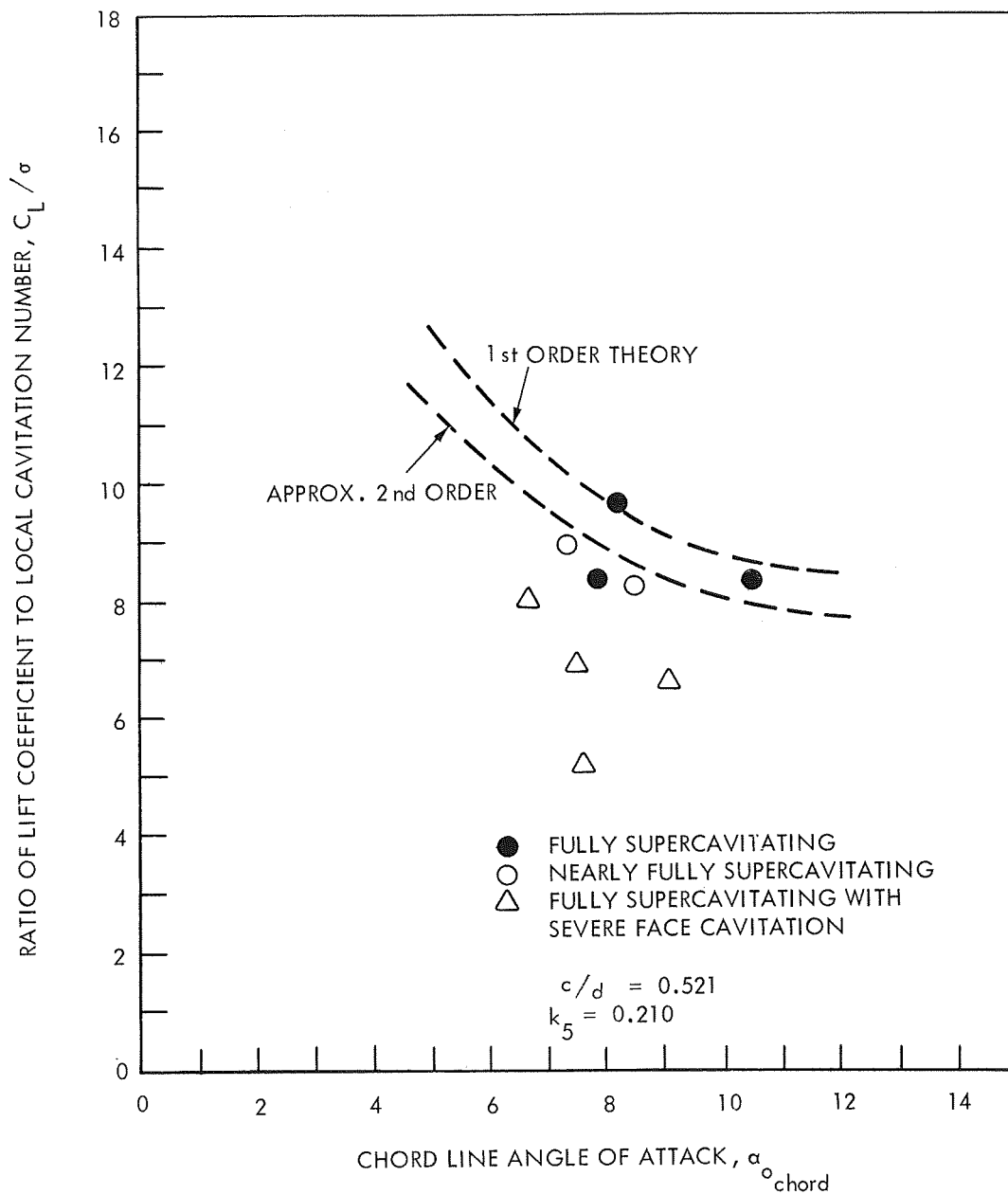


FIGURE 45 - COMPARISON OF TWO-DIMENSIONAL LINEARIZED THEORY (REF. 28) TO EXPERIMENTALLY MEASURED C_L/σ AT MID-SPAN FOR THE TWO-BLADED, FIVE TERM CAMBERED FIRST STAGE CONSIDERING ONLY DATA AT OR VERY NEAR FULLY SUPERCAVITATING OPERATION

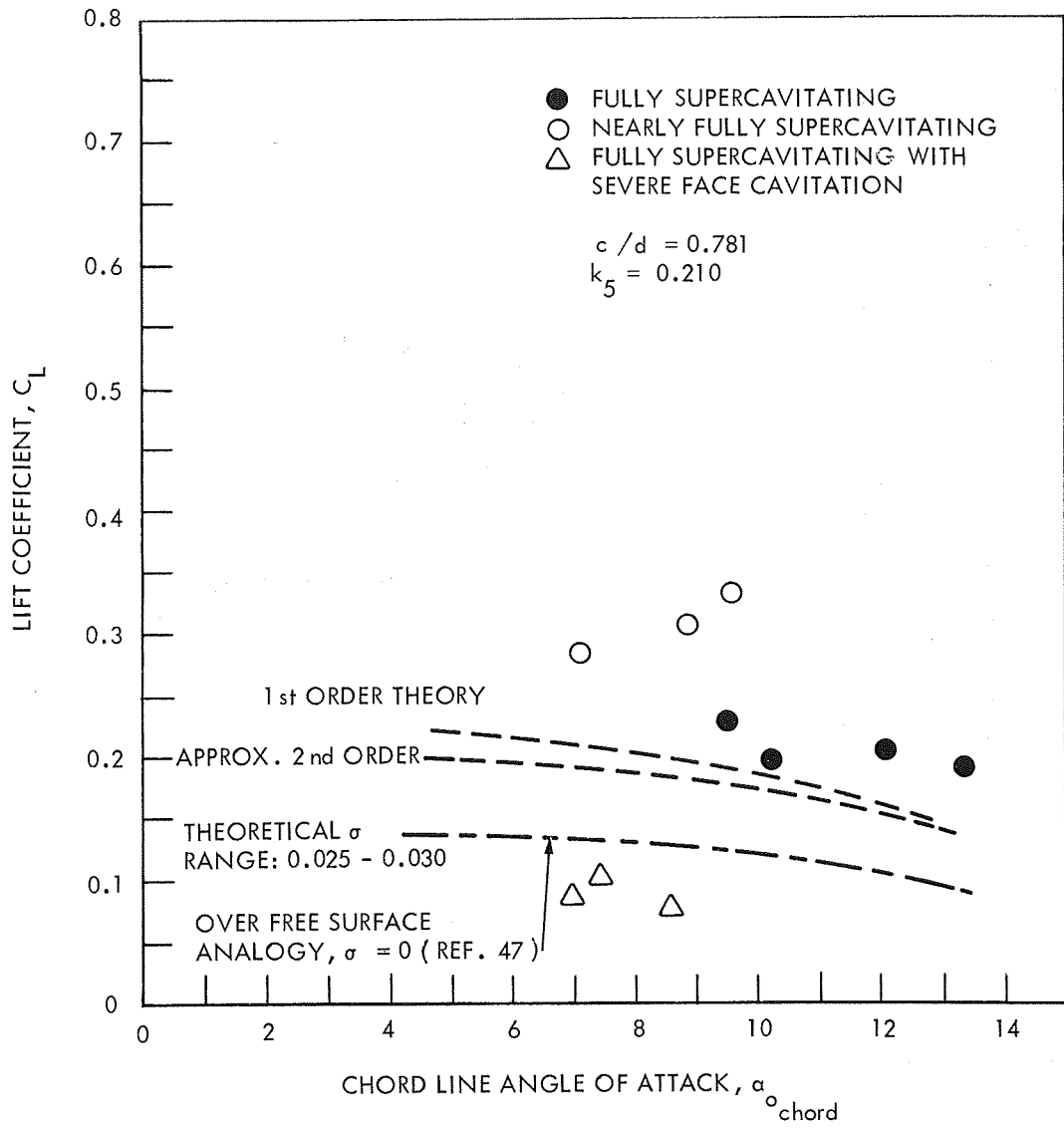


FIGURE 46 - COMPARISON OF TWO-DIMENSIONAL LINEARIZED THEORY (REF. 28) TO EXPERIMENTALLY MEASURED LIFT AND ANGLE OF ATTACK AT MID-SPAN FOR THE THREE-BLADED, FIVE-TERM CAMBERED FIRST STAGE CONSIDERING ONLY DATA AT OR NEAR FULLY SUPERCAVITATING OPERATION.

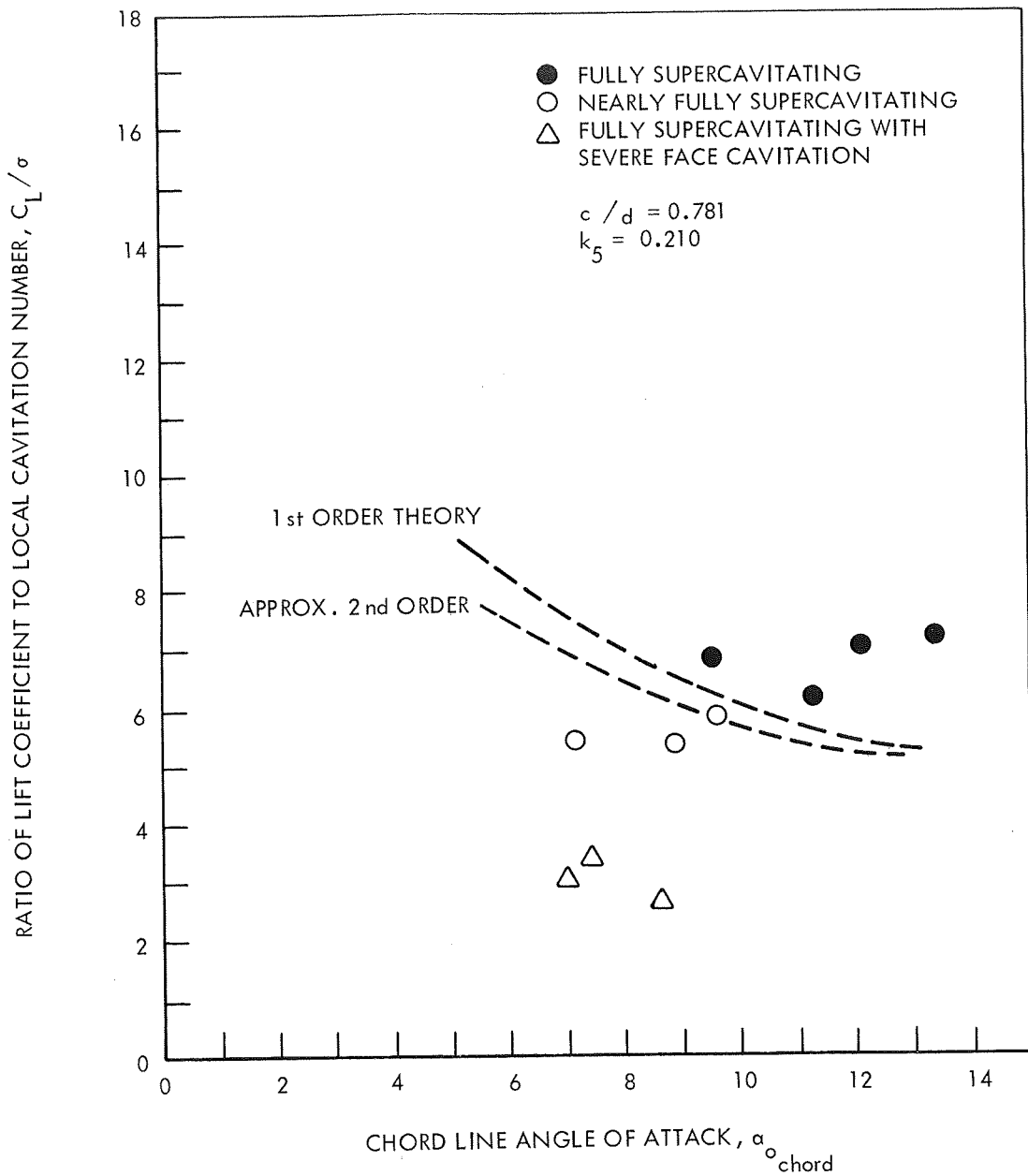
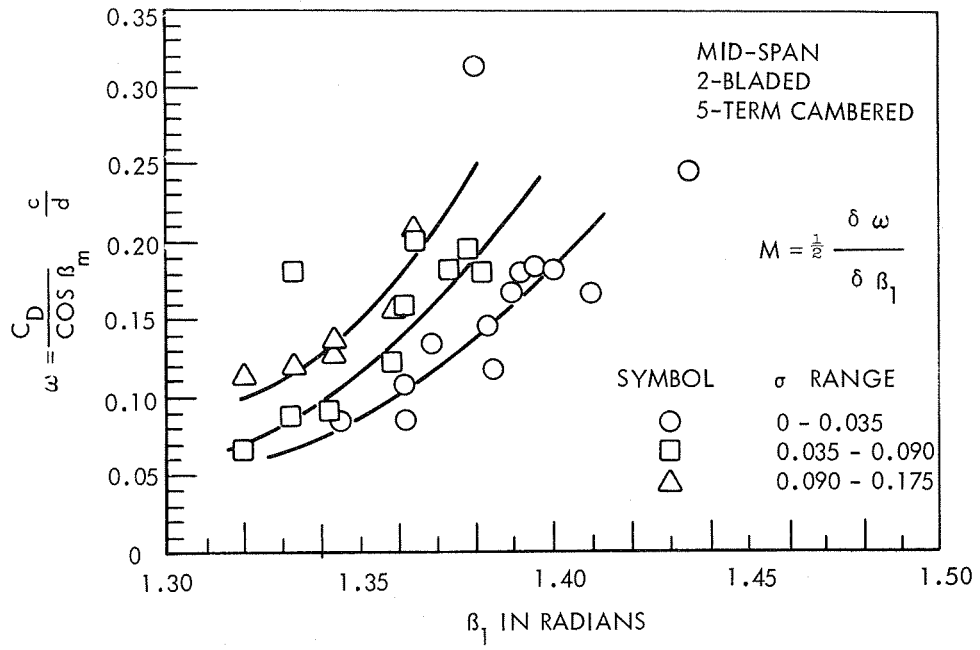
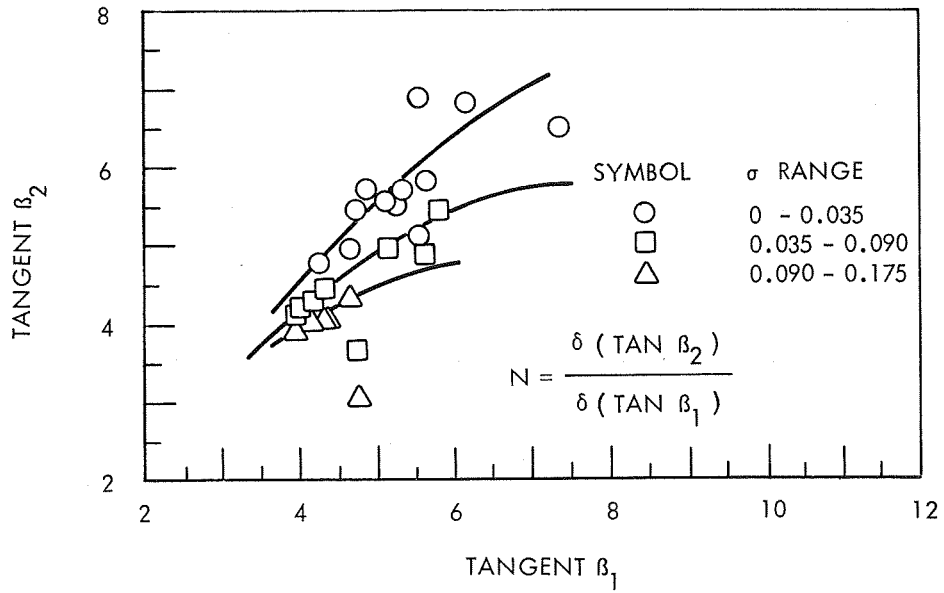


FIGURE 47- COMPARISON OF TWO-DIMENSIONAL LINEARIZED THEORY (REF. 28) TO EXPERIMENTALLY MEASURED C_L/σ AT MID-SPAN FOR THE THREE-BLADED, FIVE-TERM CAMBERED FIRST STAGE CONSIDERING ONLY DATA AT OR NEAR FULLY SUPERCAVITATING OPERATION.



(a)



(b)

FIGURE 48 - TYPICAL PLOTS FOR THE DETERMINATION OF THE PARTIAL DERIVATIVES M AND N REQUIRED IN THE YEH (16) STABILITY ANALYSIS FROM THE DATA FOR A FIRST STAGE INDUCER .

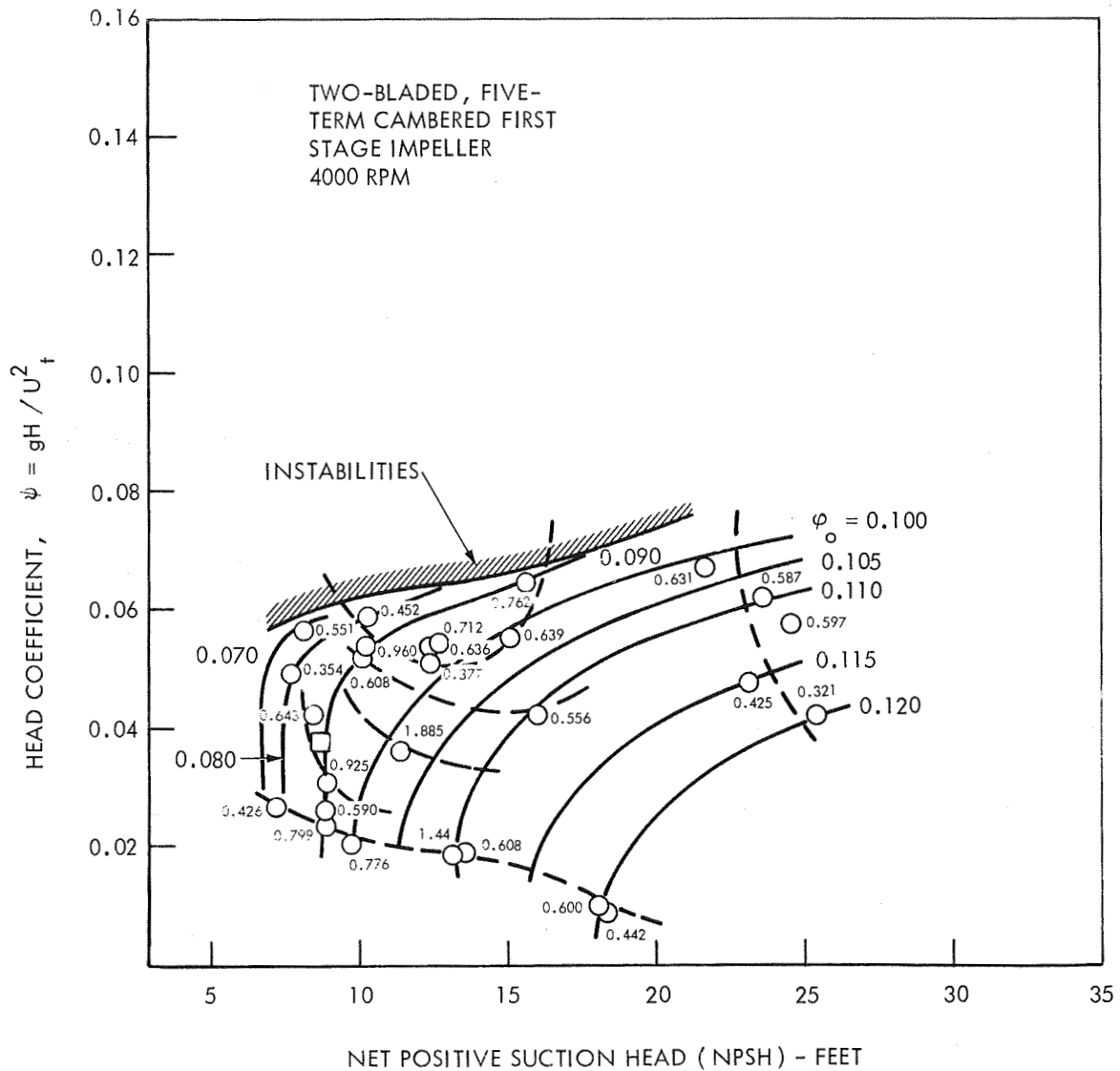


FIGURE 49 - VALUES OF YEH (16) STABILITY PARAMETER CALCULATED FROM EXPERIMENTAL DATA AT VARIOUS POINTS IN THE OPERATING REGIME OF THE TWO-BLADED FIVE-TERM CAMBERED FIRST STAGE.

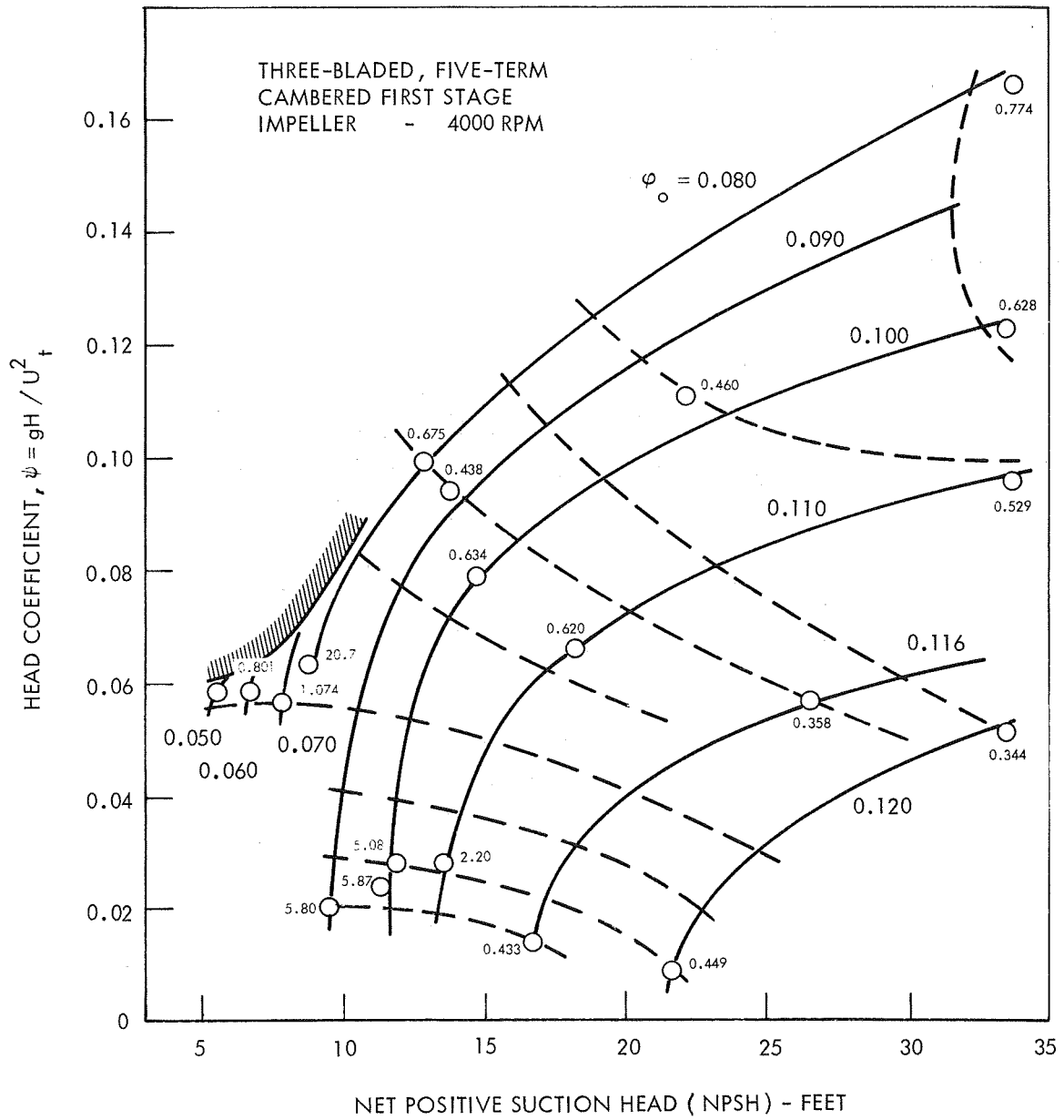


FIGURE 50 - VALUES OF YEH (16) STABILITY PARAMETER CALCULATED FROM EXPERIMENTAL DATA AT VARIOUS POINTS IN THE OPERATING REGIME OF THE THREE-BLADED FIVE-TERM CAMBERED FIRST STAGE

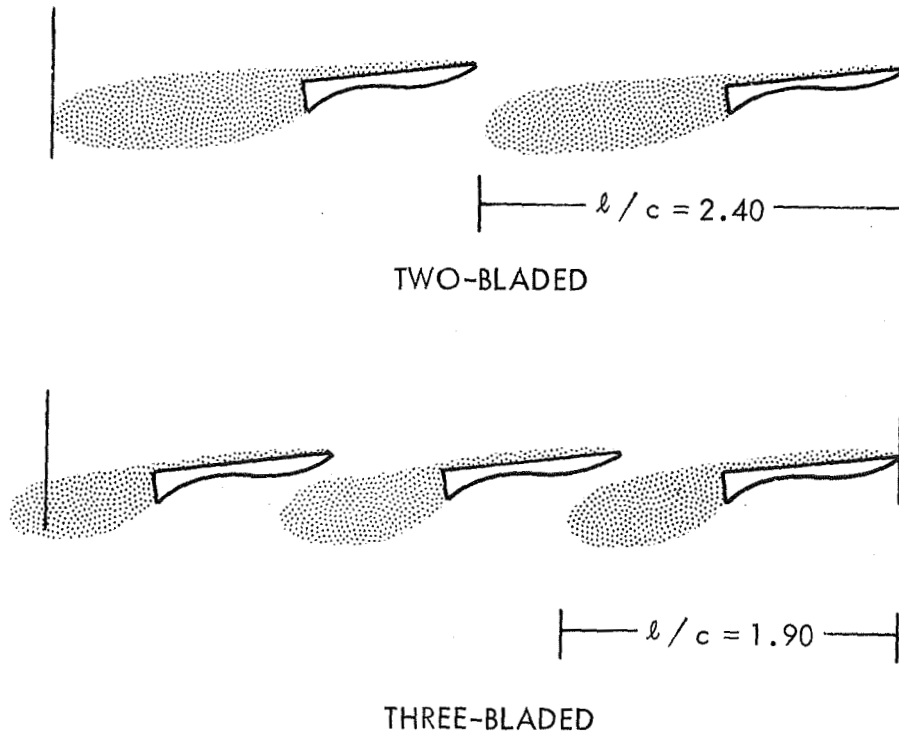


FIGURE 51 - CAVITY LENGTHS AT WHICH SEVERE INSTABILITIES OCCURRED FOR THE TWO-BLADED AND THREE-BLADED FIVE-TERM CAMBERED SUPERCAVITATING FIRST STAGE MODELS.

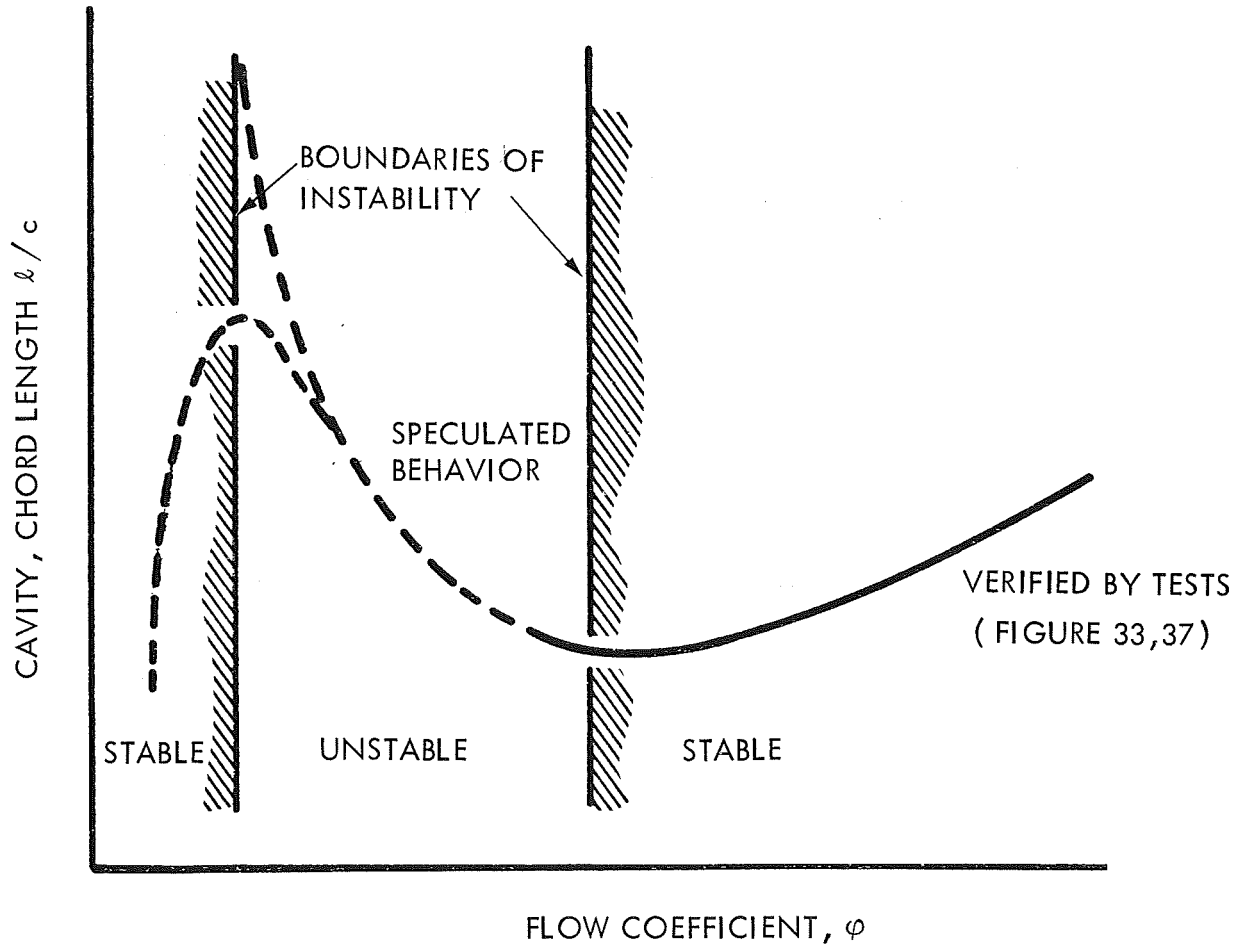


FIGURE 52 - MEASURED AND SPECULATED VARIATION OF BLADE CAVITY LENGTH AS A FUNCTION OF FLOW COEFFICIENT AT CONSTANT NPSH.

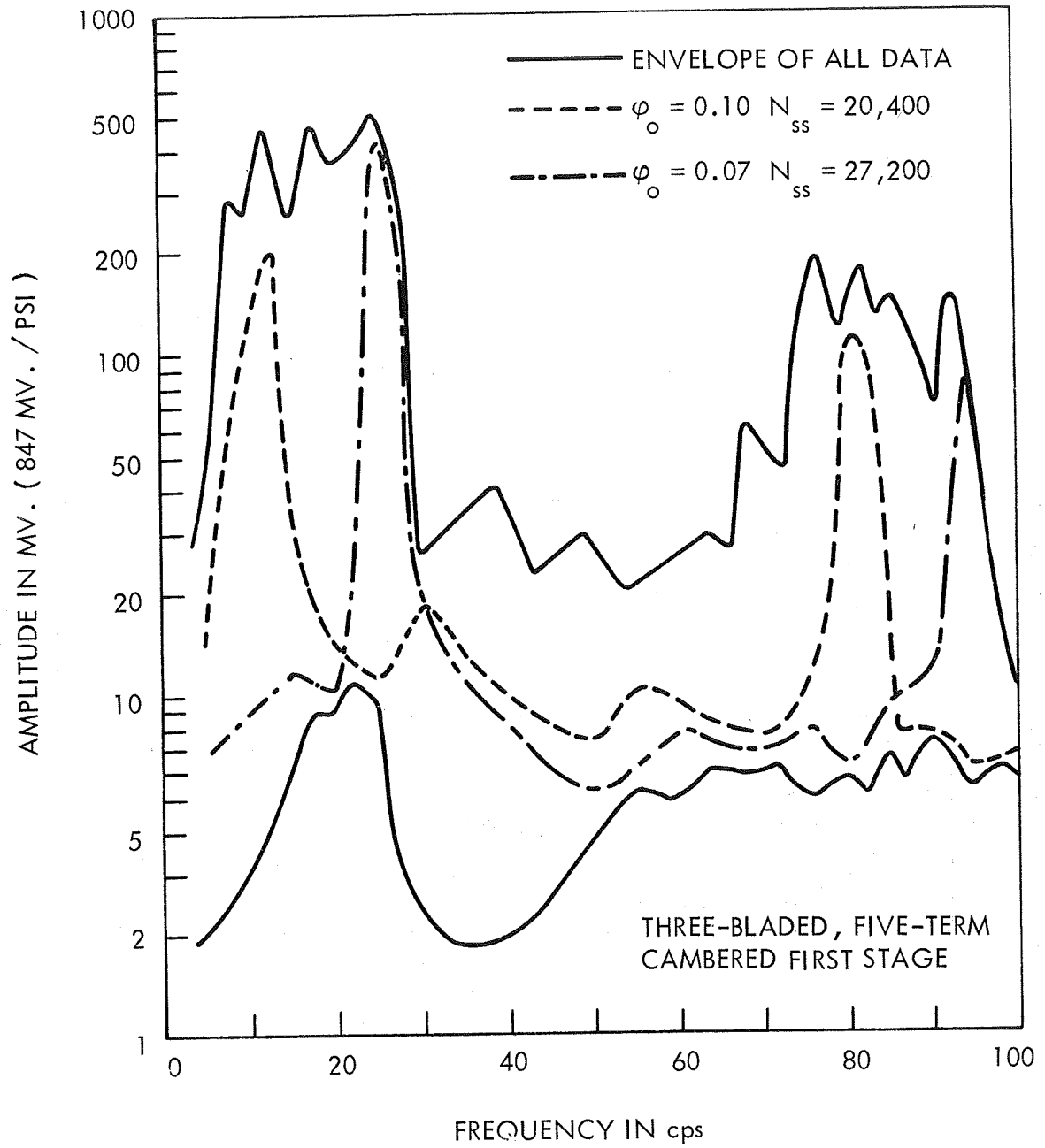


FIGURE 53 - TYPICAL PRESSURE FLUCTUATIONS AND AMPLITUDES IN THE 0-100 cps RANGE

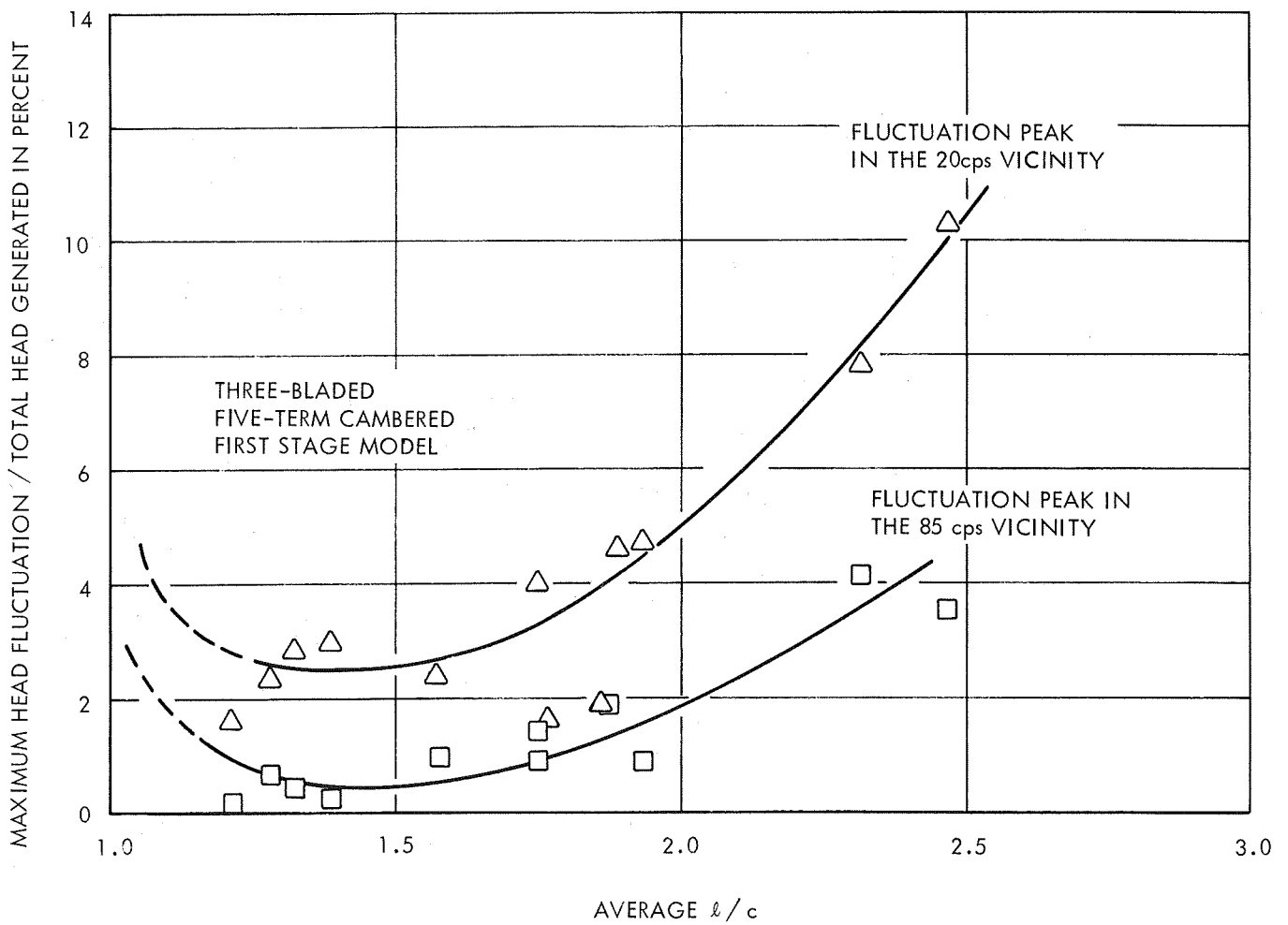


FIGURE 54 - HEAD FLUCTUATIONS AS A PERCENTAGE OF TOTAL HEAD GENERATED FOR VARIOUS CAVITY LENGTHS IN THE "STABLE" OPERATING REGIME

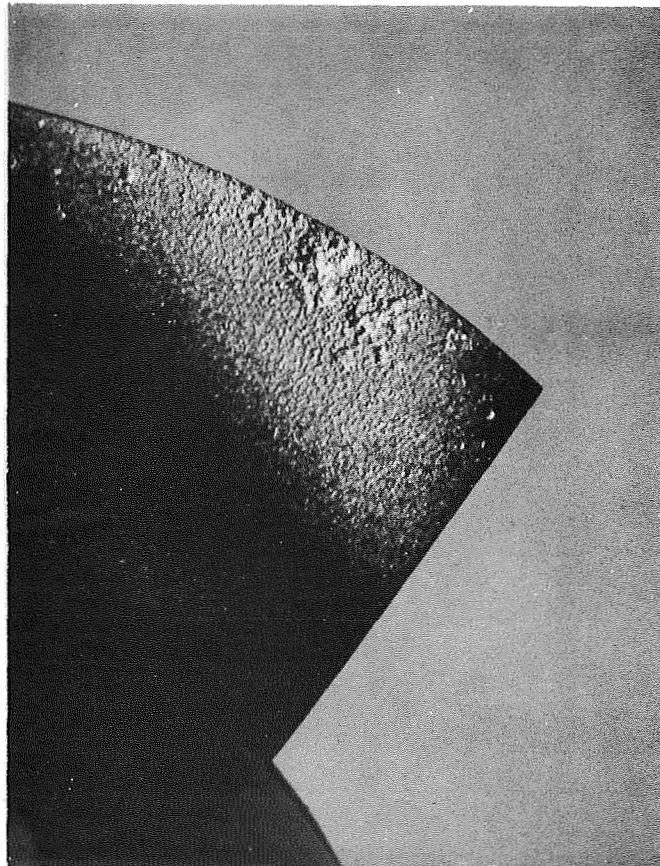


FIGURE 55 - CAVITATION DAMAGE TO THE BACK TRAILING EDGE OF
A PHASE I CONSTANT PRESSURE CAMBERED MODEL

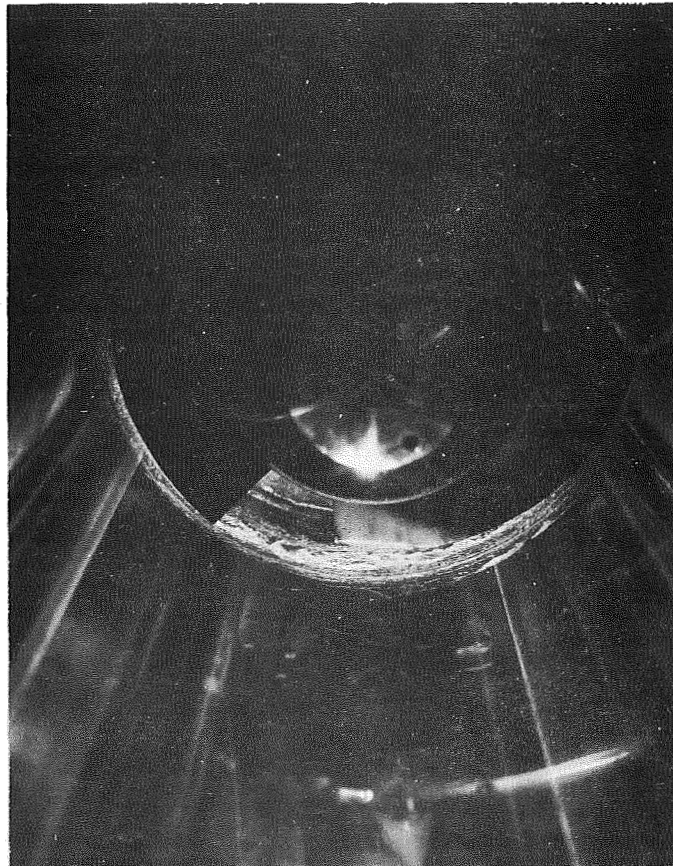


FIGURE 56 - CAVITATION DAMAGE TO THE PLEXIGLAS TEST SECTION OF THE PUMP LOOP DURING TESTS OF THE PHASE I CONSTANT PRESSURE CAMBERED MODELS.

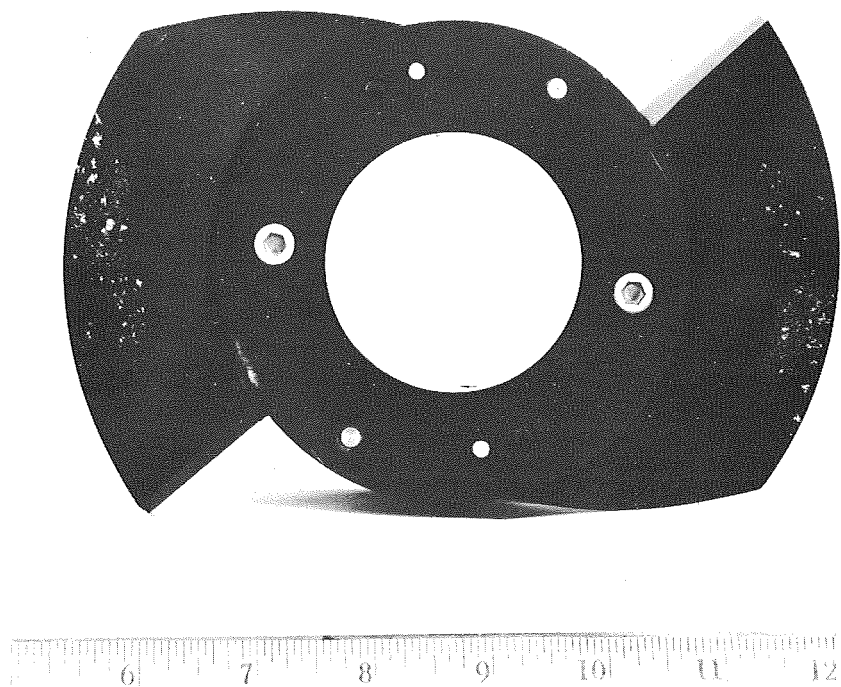


FIGURE 57 - CAVITATION DAMAGE TO THE FACE OF THE PHASE III
TWO-BLADED FIVE-TERM CAMBERED FIRST STAGE

HYDRONAUTICS, Incorporated

DISTRIBUTION LIST
Contract No. NAS 8-20625

NASA Marshall Space Flight Center		NASA Scientific and Tech.	
Huntsville, Alabama 35812		Inf. Facility	
Attn: Code PR-RC	1	P. O. Box 33	
Code MS-DL	1	College Park, Md. 20740	73
Technology Utilization			
Office, MS-T	1	Director	
Code MS-I	1	Launch Vehicles and Prop, SV	
Loren A. Gross,		Office of Space Science	
S and E-ASTN-PPA	1	and Applications	
Technical Manager,		NASA Headquarters	
S and E-ASTN-PPA	2	Washington, D. C. 20546	1
Dale Burrows,			
S and E-ASTN-PJ	1	Director	
Office of Tech. Inf.		Advanced Manned Missions, MT	
MS-IP	2	Office of Manned Space Flight	
Technical Library	1	NASA Headquarters	
Purchasing Office, PR-EC	1	Washington, D. C. 20546	1
Patent Office, M-PAT	1		
		Mission Analysis Division	
Fort Holabird		NASA Ames Research Center	
Baltimore, Maryland 21219		Moffett Field, Calif. 24035	1
Attn: Code DCASA			
(DCRP-DB)	1	NASA Ames Research Center	
		Moffett Field, Calif. 94035	
Chief, Liquid Propulsion		Attn: Hans M. Mark	1
Technology, RPL			
Office of Advanced Res and Tech.		Goddard Space Flight Center	
NASA Headquarters		Greenbelt, Md. 20771	
Washington, D. C. 20546	3	Attn: Merland L. Moseson	
		Code 620	1
Director			
Technology Utilization Division		Jet Propulsion Laboratory	
Office of Tech. Utilization		Calif. Inst. of Technology	
NASA Headquarters		4800 Oak Grove Drive	
Washington, D. C. 20546	1	Pasadena, Calif. 91103	
		Attn: Henry Burlage, Jr.	
		Prop. Div. 38	2

HYDRONAUTICS, Incorporated

-2-

Langley Research Center Langley Station Hampton, Virginia 23365 Attn: Ed. Cortwright, Dir.	2	Dr. George Wislicenus 4641 Coronado Drive Tucson, Arizona 85718	1
Lewis Research Center 21000 Brookpark Road Cleveland, Ohio 44135 Attn: Dr. A. Silverstein, Dir.	2	Case Western Reserve Univ. University Circle Cleveland, Ohio 44106 Attn: Dr. E. Reshotko	1
Manned Spacecraft Center Houston, Texas 77001 Attn: Joseph G. Thibodaux, Jr. Chief, Prop. and Power Division	2	Stanford University Palo Alto, Calif. 94305 Attn: Dr. S. Kline	1
John F. Kennedy Space Center NASA Cocoa Beach, Fla. 32931 Attn: Dr. Kurt H. Debus	1	University of Michigan Ann Arbor, Michigan 48108 Attn: Dr. F.G. Hammitt	1
Georgia Inst. of Technology Atlanta, Georgia 30332	1	Mass. Inst. of Technology Cambridge, Mass. 02139 Attn: Dr. Mann	1
Pennsylvania State University State College, Penn. Attn: Dr. W. Holl 19111	1	Purdue University Lafayette, Indiana 47907 Attn: Dr. Bruce Reese	1
Iowa State University Ames, Iowa Attn: Dr. George Serovy 52241	1	Cornell University Ithaca, New York 14850 Attn: Dr. D.L. Turcott	1
Calif. Inst. of Technology Pasadena, Calif. Attn: Dr. Acosta 91101	1	Rensselaer Polytechnic Inst. Troy, New York 12181 Attn: Dr. Foa	1
Naval Postgraduate Training Center, Monterey, California 93940 Attn: Dr. Vavra	1	Princeton University Princeton, N. J. 08540 Attn: Dr. G. L. Mellor	1
		Mr. Werner Britsch Lewis Research Center Mail Stop 500-209 Cleveland, Ohio 44135	1